A first order hyperbolic framework for large strain computational solid dynamics: An upwind cell centred Total Lagrangian scheme

Jibran Haider[a], Chun Hean Lee[a,*], Antonio J. Gil[a,*], Javier Bonet[b]

(a) Zienkiewicz Centre for Computational Engineering, College of Engineering, Swansea University, Bay Campus, SA1 8EN, United Kingdom

(b) University of Greenwich, London, SE10 9LS

SUMMARY

This paper builds on recent work developed by the authors for the numerical analysis of large strain solid dynamics, by introducing an upwind cell centred hexahedral Finite Volume framework implemented within the open source code OpenFOAM [http://www.openfoam.com/http://www.openfoam.com/]. In Lee, Gil and Bonet [1], a first order hyperbolic system of conservation laws was introduced in terms of the linear momentum and the deformation gradient tensor of the system, leading to excellent behaviour in two dimensional bending dominated nearly incompressible scenarios. The main aim of this paper is the extension of this algorithm into three dimensions, its tailor-made implementation into OpenFOAM and the enhancement of the formulation with three key novelties. First, the introduction of two different strategies in order to ensure the satisfaction of the underlying involutions of the system, that is, that the deformation gradient tensor must be curl-free throughout the deformation process. Second, the use of a discrete angular momentum projection algorithm and a monolithic Total Variation Diminishing Runge-Kutta time integrator combined in order to guarantee the conservation of angular momentum. Third, and for comparison purposes, an adapted Total Lagrangian version of the Hyperelastic-GLACE nodal scheme of Kluth and Després [2] is presented. A series of challenging numerical examples are examined in order to assess the robustness and accuracy of the proposed algorithm, benchmarking it against an ample spectrum of alternative numerical strategies developed by the authors in recent publications.

Received . . .

KEY WORDS: Conservation laws; Finite Volume Method; OpenFOAM; Locking; Riemann solver; Upwind; Large strain, Solid dynamics

*Correspondence to: Chun Hean Lee (c.h.lee@swansea.ac.uk) and Antonio J. Gil (a.j.gil@swansea.ac.uk)

1. INTRODUCTION

Current commercial codes (e.g. PAM-CRASH, ANSYS AUTODYN, LS-DYNA, ABAQUS, Altair HyperCrash) used in industry for the simulation of large-scale solid mechanics problems (e.g. crash, contact, impact, fracture) are typically based on the use of classical low order Finite Element displacement based formulations. However, it is well-known that these formulations present a number of shortcomings [3, 4], namely (1) reduced order of convergence for strains and stresses in comparison with displacements [5, 6]; (2) high frequency noise in the vicinity of shocks or sharp spatial gradients [7, 8, 9, 10] and (3) numerical instabilities associated with shear locking [11], volumetric locking [12, 13] and pressure checker-boarding [14].

To alleviate some of the shortcomings mentioned above, a variety of methodologies have been developed and implemented over time into commercial codes. These enhancements are appealing to Industry as, without much extra cost (in terms of number of degrees of freedom), the necessary modifications into a standard displacement formulation tend to be very minor. This is in clear contrast to the case of high order interpolation schemes [15, 16, 17], an equally valid alternative, but where intensive modifications are necessary.

In particular, in the case of nearly incompressible materials, the B-bar (also known as mean dilatation) hexahedral element [18, 19] is very popular in Industry, despite not circumventing the inf-sup Ladyzhenskaya-Babuška-Brezzi (LBB) condition [20]. In this element, the volumetric component of the stresses is approximated via piecewise constant shape functions (equivalent to selective reduced integration).

In the case of tetrahedral elements, a very popular choice is that of nodally integrated elements, introduced for the first time by Bonet $et\ al.$ [21], where the pressure field is (under) integrated at nodes. Extensive efforts have since been made in order to prevent the appearance of hourglassing-like modes [22, 23, 24], a shortcoming of this finite element. Several variants of the original nodal-pressure approach have since followed, including the averaged nodal deformation gradient [25], the F-bar method [26] and the Smoothed Finite Element Method [12]. Despite exhibiting locking-free deformation behaviour, all methods described above still suffer from spurious hydrostatic pressure fluctuations when simulating large strain nearly incompressible materials [13]. Recently, Scovazzi and co-authors [27] have proposed an effective alternative tetrahedral velocity/pressure Updated Lagrangian mixed methodology.

On the other hand, Finite Volume based Methods (FVM), despite their maturity in the field of Computational Fluid Dynamics, have not attracted that much attention in the Solid Mechanics community. Some attempts have been reported at trying to solve solid mechanics problems using these methods [28, 29, 30, 31, 32], with most of them restricted to the use of displacement based formulations for linear elastic small strain problems, with very limited effort directed towards dealing with nearly incompressible materials [33]. Recently, some work has been published using the Finite Volume Method in contact mechanics applications [34] and moderate strains [35] by using the open source platform OpenFOAM.

An interesting FVM approach introduced by Després and Mazeran [36] in gas dynamics applications is based on the use of conservation laws discretised in space through the use of a cell centred Lagrangian (GLACE) scheme, later explored in [37, 38, 39, 40]. This scheme employs a nodal based solver with numerical interface tractions and velocities evaluated at the nodes of the

underlying mesh. This nodal scheme does not require ad-hoc procedures [4] to obtain the nodal velocities and thus it is consistent with the so-called Geometric Conservation Law. This scheme was then extended to (two dimensional) hyperelastic solids by Kluth and Després [2], opting for an Updated Lagrangian first order cell centred FVM in terms of the linear momentum $\boldsymbol{p}$ and the deformation gradient $\boldsymbol{F}$.

One of the earliest attempts at employing a mixed $\{\boldsymbol{p}, \boldsymbol{F}\}$ system of first order conservation laws in large strain solid dynamics can be traced back to the work of Trangenstein and Colella [41, 42]. In particular, a second order Total Lagrangian finite volume framework together with the use of an upwinding stabilisation was presented in two-dimensional linear elasticity [42]. Although the consideration of involutions is outlined as part of the paper, it numerical implementation is not fully described. Moreover, the example presented is restricted to the case of small strain linear elasticity.

Over the last few years, the authors of this paper have pursued the same $\{\boldsymbol{p}, \boldsymbol{F}\}$ mixed conservation-based methodology, in the form of a system of first order conservation laws. In this case, velocities, deviatoric stresses and volumetric stresses display the same rate of convergence, which proves ideal in the case of low order discretisations. This approach has been studied by the authors using a wide variety of spatial second order discretisation techniques, well known by the CFD community. Specifically, (two dimensional) cell centred upwind Finite Volume Method (Upwind-CCFVM) [1], vertex centred Jameson-Schmidt-Turkel (JST-VCFVM) [43], two step Taylor-Galerkin Finite Element Method [44] and stabilised Petrov-Galerkin Finite Element Method (PG-FEM) [45].

Subsequently, the two-field $\{\boldsymbol{p}, \boldsymbol{F}\}$ formulation was then augmented by considering a new conservation law for the Jacobian J of the deformation to effectively solve nearly incompressible and truly incompressible materials [46, 47]. Further enhancement of this $\{\boldsymbol{p}, \boldsymbol{F}, J\}$ framework has recently been reported by the authors in [48, 49], when considering compressible, nearly incompressible and truly incompressible materials governed by a polyconvex constitutive law, where the co-factor $\boldsymbol{H}$ of the deformation plays a dominant role, leading to a $\{\boldsymbol{p}, \boldsymbol{F}, J, \boldsymbol{H}\}$ system of conservation laws. The extended set of unknowns $\{\boldsymbol{p}, \boldsymbol{F}, J, \boldsymbol{H}\}$ yields an elegant system of conservation laws, where the existence of a generalised convex entropy function enables the derivation of an alternative system of conservation laws in terms of entropy conjugates [48, 49]. These CFD-based methodologies have proven to be very efficient circumventing the drawbacks of the traditional displacement based techniques.

The general purpose of this paper is to extend the mixed $\{\boldsymbol{p}, \boldsymbol{F}\}$ Upwind-CCFVM of [1] to the case of three dimensional hexahedral meshes, enhance the robustness of the algorithm and to carry out its implementation into the open source platform OpenFOAM, widely accepted these days by Industry. The new algorithm, entitled TOUCH (**TO**tal Lagrangian **U**pwind **C**ell Centred Finite Volume Method for **H**yperbolic conservation laws), includes a linear reconstruction procedure to guarantee second order spatial accuracy, a slope limiter to ensure monotonicity, an acoustic Riemann solver for the evaluation of the numerical interface fluxes and a Total Variation Diminishing Runge-Kutta (TVD-RK) time integrator.

In this paper, we have preferred to focus in the use of hexahedral meshes (i.e. the OpenFOAM preprocessing default mesh) as they are considered to be computationally more efficient than tetrahedral meshes when pursuing a cell centred finite volume approach. Specifically, in three-dimensional simulations, for a given number of nodes, the number of tetrahedral elements is

usually five to six times the number of hexahedral elements [21]. Nonetheless, the authors have also explored the possibility of using unstructured tetrahedral elements through a series of papers, either in the context of stabilised Finite Element method (see References [45, 47, 48, 49, 44]) or by using a more efficient vertex centred finite volume approach (see References [43, 46]) via the use of a dual mesh.

In addition, and following the work in [43], a new variant of the discrete angular momentum projection algorithm is carried out. Another novelty introduced in this paper, contrary to all the previous work by the authors, is that the geometry is advanced in time using the same TVD-RK time integrator in a monolithic manner.

Noticing that $\boldsymbol{F}$ must be curl-free (a differential constraint known as involution), one of the greatest challenges in designing a robust $\{\boldsymbol{p}, \boldsymbol{F}\}$ computational framework is the ability to control the appearance of spurious curl-error mechanisms. These spurious modes can accumulate and lead to the breakdown of the numerical scheme. In the context Magnetohydrodynamics, a wide variety of numerical methodologies are available for the construction of transport schemes fulfilling the satisfaction of specific involutions [50, 51, 52, 53]. In this paper, two alternative strategies are proposed; the first approach corresponds to a constrained Finite Volume Method [53, 50], whereas the second strategy corresponds to a penalised Finite Volume Method. Finally, the Hyperelastic-GLACE nodal scheme [2] is adapted to a second order Total Lagrangian setting and also implemented within OpenFOAM for comparison purposes.

The outline of the paper is as follows. Section 2 revisits the system of first order conservation laws to be solved supplemented with an appropriate constitutive law. The consideration of irreversible processes due to plasticity is discussed in Section 3, followed by a study of the eigenstructure of the system (see Appendix A). Section 4 describes the methodology of the cell centred FVM. Linear reconstruction, slope limiter and acoustic Riemann solver ingredients are also presented. Sections 5 describes the TVD Runge-Kutta time integrator used for temporal discretisation. Section 6 introduces two different versions for the update of the variables in order to control spurious curl modes over a long term response. Section 7 describes the projection algorithm used to preserve the angular momentum. Section 8 summarises the algorithmic description of the proposed methodology. In Section 9, an extensive set of numerical examples is presented to assess the performance of the proposed methods and to draw some comparisons against previous results published by the authors [43, 46, 54, 1, 45, 47]. Finally, Section 10 presents some concluding remarks and current directions of research.

2. FIRST ORDER CONSERVATION LAWS FOR REVERSIBLE ELASTODYNAMICS

It has been extensively reported in existing literature, that the use of low order displacement-based formulations [32] in large strain solid mechanics can lead to exhibit shear and volumetric deformation locking [21, 24] as well as hydrostatic pressure instabilities [25, 13, 12]. To address these shortcomings, References [2, 1, 45, 43, 44, 55] have introduced an alternative mixed linear momentum/strain formulation, which will be further explored in this paper. The resulting hyperbolic system of first order conservation laws is of a similar structure to that of the well-known Euler equations in the context of Computational Fluid Dynamics (CFD). The primary variables of interest

are linear momentum $\boldsymbol{p}$ and deformation gradient $\boldsymbol{F}$ (also known as fibre map), for which relevant conservation laws will be presented in this section.

2.1. Conservation of linear momentum

The conservation of linear momentum $\boldsymbol{p}$ per unit of undeformed volume within an arbitrary material domain Ω_0, with boundary $\partial\Omega_0$, can be expressed in integral form as

$$\frac{d}{dt}\int_{\Omega_0} \boldsymbol{p}\, d\Omega_0 = \int_{\Omega_0} \rho_0 \boldsymbol{b}\, d\Omega_0 + \int_{\partial\Omega_0} \boldsymbol{t}\, dA, \tag{1}$$

where ρ_0 is the material density of the continuum, $\boldsymbol{b}$ are the body forces per unit of mass, $\boldsymbol{t}$ represents the traction vector defined by $\boldsymbol{t} = \boldsymbol{P}\boldsymbol{N}$, $\boldsymbol{P}$ is the first Piola-Kirchhoff stress tensor and $\boldsymbol{N}$ is the material outward unit normal on $\partial\Omega_0$. Application of the Gauss divergence theorem on the boundary integral of (1) yields (for a smooth function)

$$\frac{\partial \boldsymbol{p}}{\partial t} - \mathrm{DIV}\boldsymbol{P} = \rho_0 \boldsymbol{b}, \tag{2}$$

together with the jump conditions (for non-smooth solutions) [1] defined as

$$U[\![\boldsymbol{p}]\!] = -[\![\boldsymbol{P}]\!]\boldsymbol{N}, \tag{3}$$

where DIV in (2) denotes the material divergence operator and $[\![\cdot]\!]$ in (3) the jump operator across a discontinuity surface with normal $\boldsymbol{N}$ moving with speed U in the reference space. In addition, the current geometry $\boldsymbol{x}$ can be obtained through the time integration of the linear momentum $\boldsymbol{p}$, that is

$$\frac{\partial \boldsymbol{x}}{\partial t} = \frac{\boldsymbol{p}}{\rho_0}; \qquad \boldsymbol{x} = \boldsymbol{X} + \boldsymbol{u}, \tag{4}$$

where $\boldsymbol{X}$ represents the undeformed geometry and $\boldsymbol{u}$ the displacement field.

2.2. Conservation of deformation gradient

In classical continuum mechanics, the deformation gradient is generally computed from the current geometry, namely $\boldsymbol{\nabla}_0 \boldsymbol{x} =: \boldsymbol{F}_{\boldsymbol{x}}$ (see Fig. 1). However, when accompanied by low order discretisations, this approach can lead to the appearance of locking, specially in the case of nearly incompressible simulations [56, 57]. In the best case scenario, the strains will converge at a rate one order less than the geometry. To increase the flexibility of the formulation and resolve these shortcomings, the deformation gradient $\boldsymbol{F}$ can be treated as an additional independent variable. With that in mind, an integral conservation law for the deformation gradient can be established as

$$\frac{d}{dt}\int_{\Omega_0} \boldsymbol{F}\, d\Omega_0 = \int_{\partial\Omega_0} \frac{\boldsymbol{p}}{\rho_0} \otimes \boldsymbol{N}\, dA. \tag{5}$$

Using the Gauss divergence theorem on the boundary integral of (5), it is also possible to obtain the counterpart differential (strong) form along with jump conditions as

$$\frac{\partial \boldsymbol{F}}{\partial t} - \text{DIV}\left(\frac{\boldsymbol{p}}{\rho_0} \otimes \boldsymbol{I}\right) = \boldsymbol{0}; \qquad U[\![\boldsymbol{F}]\!] = -\frac{1}{\rho_0}[\![\boldsymbol{p}]\!] \otimes \boldsymbol{N}, \tag{6}$$

where $\boldsymbol{I}$ represents the second order identity tensor. Within the CFD community, expression (6a) can be regarded as a generalisation of the classical Geometric Conservation Law (GCL) usually used for Arbitrary Lagrangian Eulerian (ALE) conservation equations in moving domains [58, 59, 60, 61]. It is clear from expression (6a) that the material CURL of $\boldsymbol{F}$ vanishes, that is [54]

$$\text{CURL}\boldsymbol{F} = \boldsymbol{0}, \tag{7}$$

where the material CURL of a second order two-point tensor $\boldsymbol{A}$ is defined via the third order alternating tensor $\boldsymbol{\mathcal{E}}$ as

$$(\text{CURL}\boldsymbol{A})_{iI} = \mathcal{E}_{IJK}\frac{\partial A_{iK}}{\partial X_J}. \tag{8}$$

2.3. Conservation of total energy

Analogously to the CFD case of the Euler equations [62, 20], it is also possible to include the total energy conservation law into our mixed system as

$$\frac{d}{dt}\int_{\Omega_0} E\, d\Omega_0 = \int_{\partial\Omega_0} \frac{1}{\rho_0}\boldsymbol{p}\cdot\boldsymbol{t}\, dA - \int_{\partial\Omega_0} \boldsymbol{Q}\cdot\boldsymbol{N}\, dA + \int_{\Omega_0} s\, d\Omega_0, \tag{9}$$

where E is the total energy per unit of undeformed volume and $\boldsymbol{Q}$ and s represent the heat flux and the heat source terms, respectively. The local form of the total energy conservation law and its jump conditions are

$$\frac{\partial E}{\partial t} - \text{DIV}\left(\frac{1}{\rho_0}\boldsymbol{P}^T\boldsymbol{p} - \boldsymbol{Q}\right) = s; \quad U[\![E]\!] = -\frac{1}{\rho_0}[\![\boldsymbol{P}^T\boldsymbol{p}]\!]\cdot\boldsymbol{N} + [\![\boldsymbol{Q}]\!]\cdot\boldsymbol{N}. \tag{10}$$

In the case of an adiabatic deformation, the heat flux $\boldsymbol{Q}$ and the heat source s are neglected. In addition, when dealing with non-thermomechanical materials, equation (10) is fully decoupled from the rest of the system of conservation laws. Even in this case, from the computational point of view, this equation is still very useful when evaluating the numerical diffusion (entropy) introduced by the algorithm and hence, will be retained in this work.

2.4. Conservation law formulation

We are now in a position to combine these balance principles (see equations (2), (6a), (10a) and (4a)) into a system of conservation laws written under a Total Lagrangian formalism as

$$\frac{\partial \boldsymbol{\mathcal{U}}}{\partial t} + \frac{\partial \boldsymbol{\mathcal{F}}_I}{\partial X_I} = \boldsymbol{\mathcal{S}}, \qquad \forall\, I = 1, 2, 3; \tag{11}$$

where $\boldsymbol{\mathcal{U}}^{\dagger}$ is the vector of conservation variables, $\boldsymbol{\mathcal{F}}_I$ is the flux vector in I-th material direction and $\boldsymbol{\mathcal{S}}$ is the source term. Their respective components are

$$\boldsymbol{\mathcal{U}} = \begin{bmatrix} \boldsymbol{p} \\ \boldsymbol{F} \\ E \\ \boldsymbol{x} \end{bmatrix}, \qquad \boldsymbol{\mathcal{F}}_I = \begin{bmatrix} -\boldsymbol{P}\boldsymbol{E}_I \\ -\frac{\boldsymbol{p}}{\rho_0} \otimes \boldsymbol{E}_I \\ -\left(\frac{1}{\rho_0}\boldsymbol{P}^T\boldsymbol{p}\right) \cdot \boldsymbol{E}_I + \boldsymbol{Q} \cdot \boldsymbol{E}_I \\ \boldsymbol{0} \end{bmatrix}, \qquad \boldsymbol{\mathcal{S}} = \begin{bmatrix} \rho_0 \boldsymbol{b} \\ \boldsymbol{0} \\ s \\ \frac{\boldsymbol{p}}{\rho_0} \end{bmatrix}, \tag{12}$$

and the Cartesian coordinate basis

$$\boldsymbol{E}_1 = \begin{bmatrix} 1 \\ 0 \\ 0 \end{bmatrix}; \quad \boldsymbol{E}_2 = \begin{bmatrix} 0 \\ 1 \\ 0 \end{bmatrix}; \quad \boldsymbol{E}_3 = \begin{bmatrix} 0 \\ 0 \\ 1 \end{bmatrix}. \tag{13}$$

The corresponding flux vector (12b) associated with the material unit outward normal $\boldsymbol{N}$ can be expressed as

$$\boldsymbol{\mathcal{F}}_{\boldsymbol{N}} = \boldsymbol{\mathcal{F}}_I N_I = \begin{bmatrix} -\boldsymbol{t} \\ -\frac{\boldsymbol{p}}{\rho_0} \otimes \boldsymbol{N} \\ -\frac{1}{\rho_0}\boldsymbol{t} \cdot \boldsymbol{p} + \boldsymbol{Q} \cdot \boldsymbol{N} \\ \boldsymbol{0} \end{bmatrix}. \tag{14}$$

For closure of system (11), it is necessary to introduce an appropriate constitutive model to relate $\boldsymbol{P}$ with $\boldsymbol{F}$ and E, obeying the principle of objectivity [1, 47] and thermodynamic consistency (via the Colemann-Noll procedure) [63]. Finally, for the complete definition of the Initial Boundary Value Problem (IBVP), initial and boundary (essential and natural) conditions must also be specified.

2.5. Constitutive model: Hyperelasticity

Numerous well-known engineering and biological materials (e.g. tyres, biological tissue or elastomeric gaskets) are modelled as hyperelastic [64]. One of the simplest hyperelastic models is the nearly incompressible neo-Hookean model, where its strain energy ψ is decomposed into the summation of deviatoric and volumetric contributions as

$$\psi = \psi_{dev} + \psi_{vol}; \quad \psi_{dev} = \frac{\mu}{2}[J_{\boldsymbol{F}}^{-2/3}(\boldsymbol{F} : \boldsymbol{F}) - 3]; \quad \psi_{vol} = \frac{\kappa}{2}(J_{\boldsymbol{F}} - 1)^2, \tag{15}$$

where $J_{\boldsymbol{F}} = \det\boldsymbol{F} = \frac{1}{6}\,(\boldsymbol{F} \times \boldsymbol{F}) : \boldsymbol{F}$ [65] denotes the Jacobian (also known as volume map) of the deformation, μ is the shear modulus and κ the bulk modulus. The evaluation of the first Piola-Kirchhoff stress tensor follows as

$$\boldsymbol{P} = \boldsymbol{P}_{dev} + \boldsymbol{P}_{vol}; \qquad \boldsymbol{P}_{dev} = \frac{\partial \psi_{dev}}{\partial \boldsymbol{F}}; \qquad \boldsymbol{P}_{vol} = \frac{\partial \psi_{vol}}{\partial \boldsymbol{F}}, \tag{16}$$

[†]The reason behind the inclusion of the geometry update (4) as part of the system of conservation laws will become apparent in Section 7 of the paper, where a geometry-based projection operator is computed to ensure the conservation of angular momentum.

with components

$$\boldsymbol{P}_{dev} = \mu J_{\boldsymbol{F}}^{-2/3}\left[\boldsymbol{F} - \frac{1}{3}(\boldsymbol{F} : \boldsymbol{F})\boldsymbol{F}^{-T}\right]; \qquad \boldsymbol{P}_{vol} = p\boldsymbol{H}_{\boldsymbol{F}}; \qquad p = \kappa(J_{\boldsymbol{F}} - 1). \tag{17}$$

where $\boldsymbol{H}_{\boldsymbol{F}} = \text{Cof}\boldsymbol{F} = \frac{1}{2}\boldsymbol{F} \times \boldsymbol{F}$ denotes the co-factor (also known as area map) of the deformation [65] and p is the pressure field. Hyperbolicity of the system of conservation laws (11) in combination with a constitutive model such as (15), is of paramount importance especially when considering elastic materials undergoing extremely large deformations [54]. From the physical viewpoint, the satisfaction of hyperbolicity (or rank one convexity) ensures the existence of physical (real) waves travelling throughout the domain and, hence, the well-posedness of the problem. For completeness, and following recent works in [2, 47, 46, 48], the study of the eigenstructure of the mixed system (11) is included in Appendix A.

3. IRREVERSIBLE PROCESSES

In this paper, consideration of irreversible processes is restricted to the case of an isothermal elasto-plastic model typically used in metal forming applications [66]. In this particular work, thermal effects will be neglected (refer to [46] for the consideration of thermal effects). In order to model irrecoverable plastic behaviour, the standard rate-independent von Mises plasticity with isotropic hardening is used and the basic structure is summarised in **??** 1 (refer to [64] for further details).

4. SPATIAL DISCRETISATION

4.1. General remarks

Commercial and open source fluid solvers are extensively used these days in industry for CFD simulations. One of the most popular approaches pursued (used in the open source code OpenFOAM) is based on the use of an Upwind Cell Centred Finite Volume Method (CCFVM) [67, 68].

In this section, a three-dimensional Total Lagrangian CCFVM will be introduced for the analysis of large strain solid mechanics problems. The development of an acoustic Riemann solver [62] for the evaluation of the numerical fluxes and a slope reconstruction/limiter procedure [69] for second order spatial accuracy will be shown. The overall scheme will be implemented (from scratch) into the existing OpenFOAM platform. Additionally, an extension of the Updated Lagrangian Hyperelastic-GLACE nodal framework proposed by Després and Kluth [2] to a Total Lagrangian setting will also be presented and implemented in OpenFOAM for comparison purposes.

Algorithm 1: Time update of first Piola Kirchoff stress tensor

Input : $\boldsymbol{F}^{n+1}, \left[\boldsymbol{C}_p^{-1}\right]^n, \varepsilon_p^n$
Output: $\boldsymbol{P}^{n+1}$

(1) Obtain Jacobian of deformation: $J_{\boldsymbol{F}}^{n+1} = \det\left(\boldsymbol{F}^{n+1}\right)$

(2) Evaluate pressure: $p^{n+1} = \kappa \frac{\ln\left(J_{\boldsymbol{F}}^{n+1}\right)}{J_{\boldsymbol{F}}^{n+1}}$

(3) Compute trial elastic left strain tensor: $\bar{\boldsymbol{b}}_e^{n+1} = \boldsymbol{F}^{n+1}\left[\boldsymbol{C}_p^{-1}\right]^n\left[\boldsymbol{F}^T\right]^{n+1}$

(4) Spectral decomposition of $\bar{\boldsymbol{b}}_e^{n+1}$: $\bar{\lambda}_{e,i}$, $\bar{\boldsymbol{n}}_i \longleftarrow \bar{\boldsymbol{b}}_e^{n+1} = \sum_{i=1}^{3}\left(\bar{\lambda}_{e,i}\right)^2(\bar{\boldsymbol{n}}_i \otimes \bar{\boldsymbol{n}}_i)$

(5) Obtain trial deviatoric Kirchoff stress tensor:
$\bar{\boldsymbol{\tau}}' = \sum_{i=1}^{3}\bar{\tau}'_{ii}\left(\bar{\boldsymbol{n}}_i \otimes \bar{\boldsymbol{n}}_i\right), \qquad \bar{\tau}'_{ii} = 2\mu\ln\left(\bar{\lambda}_{e,i}\right) - \frac{2}{3}\mu\ln\left(J_{\boldsymbol{F}}^{n+1}\right)$

(6) Obtain yield criterion: $f\left(\bar{\boldsymbol{\tau}}', \varepsilon_p^n\right) = \sqrt{\frac{3}{2}(\bar{\boldsymbol{\tau}}' : \bar{\boldsymbol{\tau}}')} - \left(\tau_y^0 + H\varepsilon_p^n\right)$

(7) Compute direction vector and plastic multiplier:

if $f\left(\bar{\boldsymbol{\tau}}', \varepsilon_p^n\right) > 0$ **then**

Direction vector: $\boldsymbol{\upsilon}_i^{n+1} = \frac{\bar{\tau}'_{ii}}{\sqrt{\frac{2}{3}(\bar{\boldsymbol{\tau}}':\bar{\boldsymbol{\tau}}')}}$

Plastic multiplier: $\Delta\gamma = \frac{f\left(\bar{\boldsymbol{\tau}}', \varepsilon_p^n\right)}{3\mu + H}$

else

$\boldsymbol{\upsilon}_i^{n+1} = \Delta\gamma = 0$

end

(7) Evaluate elastic stretch: $\lambda_{e,i}^{n+1} = \exp\left(\ln(\bar{\lambda}_{e,i}) - \Delta\gamma\,\boldsymbol{\upsilon}_i^{n+1}\right)$

(8) Set spatial normals: $\boldsymbol{n}_i^{n+1} = \bar{\boldsymbol{n}}_i$

(9) Compute Kirchoff stresss tensor:
$\boldsymbol{\tau}^{n+1} = \sum_{i=1}^{3}\tau_{ii}\left(\boldsymbol{n}_i^{n+1} \otimes \boldsymbol{n}_i^{n+1}\right)$
$\tau_{ii} = \tau'_{ii} + J_{\boldsymbol{F}}^{n+1}p^{n+1}, \qquad \tau'_{ii} = \left(1 - \frac{2\mu\Delta\gamma}{\sqrt{\frac{2}{3}(\bar{\boldsymbol{\tau}}':\bar{\boldsymbol{\tau}}')}}\right)\bar{\tau}'_{ii}$

(10) Evaluate first Piola Kirchoff stress tensor: $\boldsymbol{P}^{n+1} = \boldsymbol{\tau}^{n+1}\left[\boldsymbol{F}^{-T}\right]^{n+1}$

(11) Update elastic left strain tensor: $\boldsymbol{b}_e^{n+1} = \sum_{i=1}^{3}\left(\lambda_{e,i}^{n+1}\right)^2\left(\boldsymbol{n}_i^{n+1} \otimes \boldsymbol{n}_i^{n+1}\right)$

(12) Compute plastic right Cauchy Green tensor: $\left[\boldsymbol{C}_p^{-1}\right]^{n+1} = \left[\boldsymbol{F}^{-1}\right]^{n+1}\boldsymbol{b}_e^{n+1}\left[\boldsymbol{F}^{-T}\right]^{n+1}$

(13) Update plastic strain: $\varepsilon_p^{n+1} = \varepsilon_p^n + \Delta\gamma$

4.2. Cell centred Finite Volume Method

The system of conservation laws (11) is discretised using the standard cell centred finite volume algorithm for hexahedral meshes (see Fig. 2). Unlike staggered approaches [56, 57], all the primary variables are computed at the centroid of each cell (also known as control volume). The spatial

discretisation of system (11) for an arbitrary cell e can be generally approximated as

$$\begin{aligned}\frac{d\boldsymbol{\mathcal{U}}_e}{dt} &= -\frac{1}{\Omega_0^e}\int_{\Omega_0^e}\frac{\partial \boldsymbol{\mathcal{F}}_I}{\partial X_I}\,d\Omega_0 \\ &= -\frac{1}{\Omega_0^e}\int_{\partial\Omega_0^e}\boldsymbol{\mathcal{F}}_{\boldsymbol{N}}\,dA \\ &\approx -\frac{1}{\Omega_0^e}\sum_{f\in\Lambda_e^f}\sum_{g\in\Lambda_f^g}\boldsymbol{\mathcal{F}}^C_{\boldsymbol{N}_{eg}}(\boldsymbol{\mathcal{U}}_g^-,\boldsymbol{\mathcal{U}}_g^+)\,\|\boldsymbol{C}_{eg}\|,\end{aligned} \tag{18}$$

where use has been made of the Gauss divergence theorem and of equation (14).[‡] In above equations, Ω_0^e denotes the control volume associated to cell e, Λ_e^f represents the set of surfaces f associated to cell e, Λ_f^g represents the set of Gauss quadrature points g associated to surface f, $\boldsymbol{N}_{eg} := \boldsymbol{C}_{eg}/\|\boldsymbol{C}_{eg}\|$ and $\|\boldsymbol{C}_{eg}\|$ denote the material outward normal and the surface area associated to Gauss quadrature point g of cell e, respectively, and $\boldsymbol{\mathcal{F}}^C_{\boldsymbol{N}_{eg}}(\boldsymbol{\mathcal{U}}_g^-,\boldsymbol{\mathcal{U}}_g^+)$ represents the numerical (contact) flux computed using the left and right states of variable $\boldsymbol{\mathcal{U}}$ at Gauss quadrature point g, namely $\boldsymbol{\mathcal{U}}_g^-$ and $\boldsymbol{\mathcal{U}}_g^+$. Upper index C will be used in the remainder of this paper to emphasise the notion of 'contact' or interface flux.

In this paper, when evaluating the surface flux integral (18), we will restrict to integrands which require a single Gauss quadrature point for exact integration, seeking computational efficiency of the overall scheme. In this case, the reduced form of the variable update (18) takes the form

$$\frac{d\boldsymbol{\mathcal{U}}_e}{dt} = -\frac{1}{\Omega_0^e}\sum_{f\in\Lambda_e^f}\boldsymbol{\mathcal{F}}^C_{\boldsymbol{N}_{ef}}(\boldsymbol{\mathcal{U}}_f^-,\boldsymbol{\mathcal{U}}_f^+)\,\|\boldsymbol{C}_{ef}\| \tag{19}$$

where $\boldsymbol{N}_{ef} := \boldsymbol{C}_{ef}/\|\boldsymbol{C}_{ef}\|$ and $\|\boldsymbol{C}_{ef}\|$ represent the material outward normal and the surface area associated to face f of cell e and $\boldsymbol{\mathcal{F}}^C_{\boldsymbol{N}_{ef}}(\boldsymbol{\mathcal{U}}_f^-,\boldsymbol{\mathcal{U}}_f^+)$ represents the numerical (contact) flux computed using the left and right states of variable $\boldsymbol{\mathcal{U}}$ at face f, namely $\boldsymbol{\mathcal{U}}_f^-$ and $\boldsymbol{\mathcal{U}}_f^+$. Above expression can now be particularised for the individual components of $\boldsymbol{\mathcal{U}}$, yielding

$$\frac{d\boldsymbol{p}_e}{dt} = \frac{1}{\Omega_0^e}\sum_{f\in\Lambda_e^f}\boldsymbol{t}_f^C\|\boldsymbol{C}_{ef}\|, \tag{20a}$$

$$\frac{d\boldsymbol{F}_e}{dt} = \frac{1}{\Omega_0^e}\sum_{f\in\Lambda_e^f}\frac{\boldsymbol{p}_f^C}{\rho_0}\otimes\boldsymbol{C}_{ef}, \tag{20b}$$

$$\frac{dE_e}{dt} = \frac{1}{\Omega_0^e}\sum_{f\in\Lambda_e^f}\frac{\zeta_f^C}{\rho_0}\|\boldsymbol{C}_{ef}\|, \tag{20c}$$

$$\frac{d\boldsymbol{x}_e}{dt} = \frac{\boldsymbol{p}_e}{\rho_0}, \tag{20d}$$

where $\boldsymbol{t}_f^C = \boldsymbol{P}_f^C\boldsymbol{N}_{ef}$ is the contact traction and $\zeta_f^C = \left(\boldsymbol{t}_f\cdot\boldsymbol{p}_f\right)^C$ the total energy contact adiabatic flux. Above equations (19) or (20) summarise the update of conservation variables via the integration of the numerical contact fluxes.

[‡]In what follows, e stands for cell, f denotes face and g represents a Gauss quadrature point.

Remark 1: Alternatively, the variable update above (19) can be re-expressed in terms of so-called nodal fluxes [2, 38, 70, 71, 37, 39] (see Fig. 3)

$$\frac{d\boldsymbol{\mathcal{U}}_e}{dt} = -\frac{1}{\Omega_0^e}\sum_{a\in\Lambda_e^a} \boldsymbol{\mathcal{F}}^C_{\boldsymbol{N}_{ea}}(\boldsymbol{\mathcal{U}}_a^-,\boldsymbol{\mathcal{U}}_a^+)\,\|\boldsymbol{C}_{ea}\|, \tag{21}$$

where Λ_e^a represents the set of nodes a associated with cell e, $\boldsymbol{N}_{ea} := \boldsymbol{C}_{ea}/\|\boldsymbol{C}_{ea}\|$ and $\|\boldsymbol{C}_{ea}\|$ represent the outward 'nodal' normal and area (see Reference [38] for the computation of $\|\boldsymbol{C}_{ea}\|$ for hexahedral meshes), respectively, and $\boldsymbol{\mathcal{F}}^C_{\boldsymbol{N}_{ea}}(\boldsymbol{\mathcal{U}}_a^-,\boldsymbol{\mathcal{U}}_a^+)$ represents the numerical (contact) flux evaluated using the left and right states of variable $\boldsymbol{\mathcal{U}}$, namely $\boldsymbol{\mathcal{U}}_a^-$ and $\boldsymbol{\mathcal{U}}_a^+$, at node a of cell e. Detailed discussion on this nodal based solver can be found in Section 6.2.2.

It is worth noting that expression (19) or its nodal equivalent (21) lead to a first order solution in space as long as $\boldsymbol{\mathcal{U}}_f^-$ and $\boldsymbol{\mathcal{U}}_f^+$ are modelled following a piecewise constant representation within every cell. As a result, the accuracy of this approach is severely undermined by an excess of numerical dissipation, whereby the physics of the problem can no longer be accurately captured unless excessively fine meshes are used. Thus, a suitable reconstruction procedure over each cell will be carried out in the next section.

4.2.1. Linear reconstruction procedure. With a second order spatial solution in mind, a linear reconstruction procedure is employed for the evaluation of the states at the interface (contact) between neighbouring cells (see expressions (19) and (21)). For this reason, it is necessary to obtain an appropriate local gradient operator $\boldsymbol{G}_e$ through, for instance, a least squares minimisation process [1, 70]. Introducing first the objective functional Π defined by

$$\Pi(\boldsymbol{G}_e) = \frac{1}{2}\sum_{\alpha\in\Lambda_e^\alpha}\frac{1}{\|\boldsymbol{d}_{e\alpha}\|^2}\left[\mathcal{U}_\alpha - (\mathcal{U}_e + \boldsymbol{G}_e\cdot\boldsymbol{d}_{e\alpha})\right]^2; \quad \boldsymbol{d}_{e\alpha} = \boldsymbol{X}_\alpha - \boldsymbol{X}_e, \tag{22}$$

$\mathcal{U}$ is a generic individual component of the unknown vector $\boldsymbol{\mathcal{U}}$, Λ_e^α represents the set of neighbouring values α associated to cell e and $\boldsymbol{d}_{e\alpha}$ represents a material position vector pointing from the centroid of cell e, $\boldsymbol{X}_e$, to the centroid of cell α, $\boldsymbol{X}_\alpha$. The directional derivative of (22) with respect to $\boldsymbol{G}_e$ gives

$$\boldsymbol{0} = D\Pi[\boldsymbol{G}_e] = \sum_{\alpha\in\Lambda_e^\alpha}\frac{1}{\|\boldsymbol{d}_{e\alpha}\|^2}\left[\mathcal{U}_\alpha - (\mathcal{U}_e + \boldsymbol{G}_e\cdot\boldsymbol{d}_{e\alpha})\right]\boldsymbol{d}_{e\alpha}. \tag{23}$$

Rearranging equation (23) gives the following expression for $\boldsymbol{G}_e$

$$\boldsymbol{G}_e = \left[\sum_{\alpha\in\Lambda_e^\alpha}\hat{\boldsymbol{d}}_{e\alpha}\otimes\hat{\boldsymbol{d}}_{e\alpha}\right]^{-1}\sum_{\alpha\in\Lambda_e^\alpha}\left(\frac{\mathcal{U}_\alpha - \mathcal{U}_e}{\|\boldsymbol{d}_{e\alpha}\|}\right)\hat{\boldsymbol{d}}_{e\alpha}; \quad \hat{\boldsymbol{d}}_{e\alpha} = \frac{\boldsymbol{d}_{e\alpha}}{\|\boldsymbol{d}_{e\alpha}\|}, \tag{24}$$

where $\hat{\boldsymbol{d}}_{e\alpha}$ is the unit vector in the direction of $\boldsymbol{d}_{e\alpha}$. Finally, with the aid of (24), the linear reconstructed value at any position $\boldsymbol{X}$ within the cell e can be written as

$$\mathcal{U}(\boldsymbol{X}) = \mathcal{U}_e + \boldsymbol{G}_e \cdot (\boldsymbol{X} - \boldsymbol{X}_e). \tag{25}$$

The reconstructed values $\mathcal{U}(\boldsymbol{X})$ (25) can lead to undershoots and overshoots in the vicinity of sharp spatial gradients. For this reason, the inclusion of a slope limiter is necessary to avoid the creation of a new local extrema at flux integration points [72].

4.2.2. Monotonicity: Slope correction. For the satisfaction of monotonicity, it is crucial to correct the linear gradient reconstruction (25) by including a scalar correction term ϕ_e to yield

$$\mathcal{U}(\boldsymbol{X}) = \mathcal{U}_e + \phi_e \boldsymbol{G}_e \cdot (\boldsymbol{X} - \boldsymbol{X}_e). \tag{26}$$

The algorithm below describes the conventional Barth and Jespersen limiter [69] used in this paper:

1. Find the smallest and largest averaged values among the neighbouring values α and the owner value e

$$\mathcal{U}_e^{\min} = \min_{\alpha \in \Lambda_e^\alpha} (\mathcal{U}_e, \mathcal{U}_\alpha), \qquad \mathcal{U}_e^{\max} = \max_{\alpha \in \Lambda_e^\alpha} (\mathcal{U}_e, \mathcal{U}_\alpha).$$

2. Compute an unlimited reconstructed value (set ϕ_e = 1 in equation (26) or use equation (25)) at each flux integration point, namely

$$\mathcal{U}_{e\alpha} = \mathcal{U}_e + \boldsymbol{G}_e \cdot (\boldsymbol{X}_\alpha - \boldsymbol{X}_e); \quad \forall \alpha \in \Lambda_e^\alpha.$$

3. Obtain a maximum allowable value of $\phi_{e\alpha}$ at each flux integration point

$$\phi_{e\alpha} = \begin{cases} \min\left(1, \frac{\mathcal{U}_e^{\max} - \mathcal{U}_e}{\mathcal{U}_{e\alpha} - \mathcal{U}_e}\right), & \text{if} \quad \mathcal{U}_{e\alpha} - \mathcal{U}_e > 0 \\ \min\left(1, \frac{\mathcal{U}_e^{\min} - \mathcal{U}_e}{\mathcal{U}_{e\alpha} - \mathcal{U}_e}\right), & \text{if} \quad \mathcal{U}_{e\alpha} - \mathcal{U}_e < 0 \\ 1, & \text{if} \quad \mathcal{U}_{e\alpha} - \mathcal{U}_e = 0 \end{cases}$$

4. Select $\phi_e = \min_{\alpha \in \Lambda_e^\alpha} (\phi_{e\alpha})$.

4.3. Lagrangian contact algorithm

The upwind finite volume spatial discretisation requires an approximate Riemann solver [62] to numerically compute contact fluxes ($\boldsymbol{t}_f^C$, $\boldsymbol{p}_f^C$ and ζ_f^C in (20)). All the numerical examples presented in this paper have been generated through the use of an acoustic (or linearised) Riemann solver [1], which will be presented below.

4.3.1. Acoustic Riemann solver. In what follows, some of the results included in Appendix A will be employed. In Lagrangian dynamics, it is often possible for two domains (i.e. Ω_0^+ and Ω_0^-) to come into contact with each other after time t. The impact would generate two types of shock waves (i.e. p-wave c_p and s-wave c_s) travelling within the domains, as shown in Fig. 4. Similar waves propagate in the interface between neighbouring cells when considering piecewise discontinuous solutions. In

general, the interface (contact) flux across a discontinuity surface defined by the outward material unit normal vector $\boldsymbol{N}_{ef}$, namely $\boldsymbol{\mathcal{F}}^{C}_{\boldsymbol{N}_{ef}}$ (14) can be computed as [73, 67]

$$\boldsymbol{\mathcal{F}}^{C}_{\boldsymbol{N}_{ef}} = \underbrace{\frac{1}{2}\left[\boldsymbol{\mathcal{F}}_{\boldsymbol{N}_{ef}}(\boldsymbol{\mathcal{U}}_f^-) + \boldsymbol{\mathcal{F}}_{\boldsymbol{N}_{ef}}(\boldsymbol{\mathcal{U}}_f^+)\right]}_{\text{Unstable flux}} \underbrace{-\frac{1}{2}\int_{\boldsymbol{\mathcal{U}}_f^-}^{\boldsymbol{\mathcal{U}}_f^+} |\boldsymbol{\mathcal{A}}_{\boldsymbol{N}_{ef}}|\,\mathrm{d}\boldsymbol{\mathcal{U}}}_{\text{Upwinding stabilisation}}, \tag{27}$$

where the above integral is evaluated along an arbitrary path from $\boldsymbol{\mathcal{U}}_f^-$ to $\boldsymbol{\mathcal{U}}_f^+$. The first term denotes the unstable flux (simple arithmetic average from the left and the right states), implying no consideration for wave directional character. The second (upwinding stabilisation) term can be interpreted as a numerical diffusion that damps the instabilities arising from the first term.

Referring to Appendix A, the absolute value component of the flux Jacobian matrix $|\boldsymbol{\mathcal{A}}_{\boldsymbol{N}_{ef}}| = \left|\frac{\partial \boldsymbol{\mathcal{F}}_{\boldsymbol{N}_{ef}}}{\partial \boldsymbol{\mathcal{U}}}\right|$ reads as follows

$$\begin{aligned}
|\boldsymbol{\mathcal{A}}_{\boldsymbol{N}_{ef}}| &= \frac{1}{2}\sum_{\alpha=1}^{6} |c_\alpha| \boldsymbol{\mathcal{R}}_\alpha \boldsymbol{\mathcal{L}}_\alpha^T \\
&= \frac{1}{2}(\boldsymbol{\mathcal{R}}_1, \ldots, \boldsymbol{\mathcal{R}}_6)
\begin{pmatrix}
c_p & 0 & 0 & 0 & 0 & 0 \\
0 & c_p & 0 & 0 & 0 & 0 \\
0 & 0 & c_s & 0 & 0 & 0 \\
0 & 0 & 0 & c_s & 0 & 0 \\
0 & 0 & 0 & 0 & c_s & 0 \\
0 & 0 & 0 & 0 & 0 & c_s
\end{pmatrix}
\begin{pmatrix}
\boldsymbol{\mathcal{L}}_1^T \\ \vdots \\ \boldsymbol{\mathcal{L}}_6^T
\end{pmatrix} \\
&= \frac{1}{2}\left[c_p(\boldsymbol{\mathcal{R}}_1\boldsymbol{\mathcal{L}}_1^T + \boldsymbol{\mathcal{R}}_2\boldsymbol{\mathcal{L}}_2^T) + c_s(\boldsymbol{\mathcal{R}}_3\boldsymbol{\mathcal{L}}_3^T + \boldsymbol{\mathcal{R}}_4\boldsymbol{\mathcal{L}}_4^T + \boldsymbol{\mathcal{R}}_5\boldsymbol{\mathcal{L}}_5^T + \boldsymbol{\mathcal{R}}_6\boldsymbol{\mathcal{L}}_6^T)\right],
\end{aligned} \tag{28}$$

where $\boldsymbol{\mathcal{L}}_\alpha$ and $\boldsymbol{\mathcal{R}}_\alpha$ denote the α- left and right eigenvectors of $\boldsymbol{\mathcal{A}}_{\boldsymbol{N}_{ef}}$, respectively, and c_α the non-zero α- wave speed. Substitution of expressions (77), (78) and (79) into (28), and after some simple but lengthy algebra, it leads to,

$$\begin{aligned}
|\boldsymbol{\mathcal{A}}_{\boldsymbol{N}_{ef}}| = &\begin{bmatrix}
c_s\left(\boldsymbol{I} - \boldsymbol{n}_{ef}\otimes\boldsymbol{n}_{ef}\right) & \boldsymbol{0} & \boldsymbol{0} & \boldsymbol{0} \\
\boldsymbol{0} & \frac{1}{\rho_0 c_s}\boldsymbol{\mathcal{C}}^* & \boldsymbol{0} & \boldsymbol{0} \\
\frac{c_s}{\rho_0}(\boldsymbol{I} - \boldsymbol{n}_{ef}\otimes\boldsymbol{n}_{ef})\boldsymbol{p}_f & \boldsymbol{\mathcal{T}} & \boldsymbol{0} & \boldsymbol{0} \\
\boldsymbol{0} & \boldsymbol{0} & \boldsymbol{0} & \boldsymbol{0}
\end{bmatrix} \\
&+ \begin{bmatrix}
c_p\left(\boldsymbol{n}_{ef}\otimes\boldsymbol{n}_{ef}\right) & \boldsymbol{0} & \boldsymbol{0} & \boldsymbol{0} \\
\boldsymbol{0} & (\frac{1}{\rho_0 c_p} - \frac{1}{\rho_0 c_s})(\boldsymbol{n}_{ef}\otimes\boldsymbol{N}_{ef})\otimes[\boldsymbol{\mathcal{C}}\colon(\boldsymbol{n}_{ef}\otimes\boldsymbol{N}_{ef})] & \boldsymbol{0} & \boldsymbol{0} \\
\frac{c_p}{\rho_0}(\boldsymbol{n}_{ef}\otimes\boldsymbol{n}_{ef})\boldsymbol{p}_f & \frac{1}{\rho_0 c_p}\left(\boldsymbol{n}_{ef}\cdot\boldsymbol{P}_f\boldsymbol{N}_{ef}\right)\left(\boldsymbol{\mathcal{C}}:\boldsymbol{n}_{ef}\otimes\boldsymbol{N}_{ef}\right) & \boldsymbol{0} & \boldsymbol{0} \\
\boldsymbol{0} & \boldsymbol{0} & \boldsymbol{0} & \boldsymbol{0}
\end{bmatrix},
\end{aligned} \tag{29}$$

where the fourth order constitutive tensor $\boldsymbol{\mathcal{C}}^*$ is defined as (68)

$$[\boldsymbol{\mathcal{C}}^*]_{iIjJ} = \sum_l \mathcal{C}_{iLjJ}[\boldsymbol{N}_{ef}]_L[\boldsymbol{N}_{ef}]_I$$

and

$$\boldsymbol{\mathcal{T}} = \frac{1}{\rho_0 c_s}\left[(\boldsymbol{t}_1 \cdot \boldsymbol{P}_f \boldsymbol{N}_{ef})\,(\boldsymbol{\mathcal{C}} : \boldsymbol{t}_1 \otimes \boldsymbol{N}_{ef}) + (\boldsymbol{t}_2 \cdot \boldsymbol{P}_f \boldsymbol{N}_{ef})\,(\boldsymbol{\mathcal{C}} : \boldsymbol{t}_2 \otimes \boldsymbol{N}_{ef})\right]. \tag{30}$$

In above equations, $\boldsymbol{t}_1$ and $\boldsymbol{t}_2$ are two arbitrary tangential vectors orthogonal to $\boldsymbol{n}_{ef}$, which is the spatial outward unit normal (push forward of $\boldsymbol{N}_{ef}$). Since c_s grows with $\sqrt{\mu}$ and $\boldsymbol{\mathcal{C}}$ grows with μ (refer to Appendix A), $|\boldsymbol{\mathcal{A}}_{\boldsymbol{N}_{ef}}|$ will not become unbounded in the absence of shear strength (terms appeared as divided or multiplied by c_s will simply vanish). The integral of the numerical stabilisation term in (27) yields

$$\begin{aligned}
&\int_{\boldsymbol{\mathcal{U}}_f^-}^{\boldsymbol{\mathcal{U}}_f^+} |\boldsymbol{\mathcal{A}}_{\boldsymbol{N}_{ef}}|\, d\boldsymbol{\mathcal{U}} \\
&= \int_{\boldsymbol{\mathcal{U}}_f^-}^{\boldsymbol{\mathcal{U}}_f^+} \begin{bmatrix} c_s\,(\boldsymbol{I} - \boldsymbol{n}_{ef} \otimes \boldsymbol{n}_{ef}) d\boldsymbol{p} \\ \frac{1}{\rho_0 c_s}\,((d\boldsymbol{P})\boldsymbol{N}_{ef}) \otimes \boldsymbol{N}_{ef} \\ \boldsymbol{p}_f \cdot \left[\frac{c_s}{\rho_0}\,(\boldsymbol{I} - \boldsymbol{n}_{ef} \otimes \boldsymbol{n}_{ef})\, d\boldsymbol{p}\right] + (\boldsymbol{P}_f \boldsymbol{N}_{ef}) \cdot \left[\frac{1}{\rho_0 c_s}(\boldsymbol{I} - \boldsymbol{n}_{ef} \otimes \boldsymbol{n}_{ef})\,(d\boldsymbol{P}\boldsymbol{N}_{ef})\right] \\ \boldsymbol{0} \end{bmatrix} \\
&+ \int_{\boldsymbol{\mathcal{U}}_f^-}^{\boldsymbol{\mathcal{U}}_f^+} \begin{bmatrix} c_p(\boldsymbol{n}_{ef} \otimes \boldsymbol{n}_{ef})\, d\boldsymbol{p} \\ (\frac{1}{\rho_0 c_p} - \frac{1}{\rho_0 c_s})\,[(\boldsymbol{n}_{ef} \otimes \boldsymbol{n}_{ef})(d\boldsymbol{P})\boldsymbol{N}_{ef}] \otimes \boldsymbol{N}_{ef} \\ \boldsymbol{p}_f \cdot \left[\frac{c_p}{\rho_0}\,(\boldsymbol{n}_{ef} \otimes \boldsymbol{n}_{ef})\, d\boldsymbol{p}\right] + (\boldsymbol{P}_f \boldsymbol{N}_{ef}) \cdot \left[\frac{1}{\rho_0 c_p}(\boldsymbol{n}_{ef} \otimes \boldsymbol{n}_{ef})\,(d\boldsymbol{P})\,\boldsymbol{N}_{ef}\right] \\ \boldsymbol{0} \end{bmatrix},
\end{aligned} \tag{31}$$

with $d\boldsymbol{P} = \boldsymbol{\mathcal{C}} : d\boldsymbol{F}$. In the case of linear elasticity, the fundamental assumption made for the derivation of an acoustic Riemann solver, the wave speeds are independent of the state of deformation and it is then possible to integrate above expression exactly to yield

$$\begin{aligned}
&\int_{\boldsymbol{\mathcal{U}}_f^-}^{\boldsymbol{\mathcal{U}}_f^+} |\boldsymbol{\mathcal{A}}_{\boldsymbol{N}_{ef}}|\, \mathrm{d}\boldsymbol{\mathcal{U}} \\
&= \begin{bmatrix} c_s(\boldsymbol{I} - \boldsymbol{n}_{ef} \otimes \boldsymbol{n}_{ef})(\boldsymbol{p}_f^+ - \boldsymbol{p}_f^-) \\ \frac{1}{\rho_0 c_s}\left((\boldsymbol{P}_f^+ - \boldsymbol{P}_f^-)\boldsymbol{N}_{ef}\right) \otimes \boldsymbol{N}_{ef} \\ \boldsymbol{p}_f^{\text{Ave}} \cdot \left[\frac{c_s}{\rho_0}\,(\boldsymbol{I} - \boldsymbol{n}_{ef} \otimes \boldsymbol{n}_{ef})\left(\boldsymbol{p}_f^+ - \boldsymbol{p}_f^-\right)\right] + \boldsymbol{t}_f^{\text{Ave}} \cdot \left[\frac{1}{\rho_0 c_s}(\boldsymbol{I} - \boldsymbol{n}_{ef} \otimes \boldsymbol{n}_{ef})\left[\left(\boldsymbol{P}_f^+ - \boldsymbol{P}_f^-\right)\boldsymbol{N}_{ef}\right]\right] \\ \boldsymbol{0} \end{bmatrix} \\
&+ \begin{bmatrix} c_p(\boldsymbol{n}_{ef} \otimes \boldsymbol{n}_{ef})(\boldsymbol{p}_f^+ - \boldsymbol{p}_f^-) \\ (\frac{1}{\rho_0 c_p} - \frac{1}{\rho_0 c_s})\left[(\boldsymbol{n}_{ef} \otimes \boldsymbol{n}_{ef})(\boldsymbol{P}_f^+ - \boldsymbol{P}_f^-)\boldsymbol{N}_{ef}\right] \otimes \boldsymbol{N}_{ef} \\ \boldsymbol{p}_f^{\text{Ave}} \cdot \left[\frac{c_p}{\rho_0}\,(\boldsymbol{n}_{ef} \otimes \boldsymbol{n}_{ef})\left(\boldsymbol{p}_f^+ - \boldsymbol{p}_f^-\right)\right] + \boldsymbol{t}_f^{\text{Ave}} \cdot \left[\frac{1}{\rho_0 c_p}(\boldsymbol{n}_{ef} \otimes \boldsymbol{n}_{ef})\left[\left(\boldsymbol{P}_f^+ - \boldsymbol{P}_f^-\right)\boldsymbol{N}_{ef}\right]\right] \\ \boldsymbol{0} \end{bmatrix},
\end{aligned} \tag{32}$$

where $\boldsymbol{t}_f^{\text{Ave}} = \frac{1}{2}\left(\boldsymbol{t}_f^- + \boldsymbol{t}_f^+\right)$ and $\boldsymbol{p}_f^{\text{Ave}} = \frac{1}{2}\left(\boldsymbol{p}_f^- + \boldsymbol{p}_f^+\right)$. Substitution of expression (32) into (27) results in

$$\boldsymbol{\mathcal{F}}^C_{\boldsymbol{N}_{ef}} = \begin{bmatrix} -\boldsymbol{t}_f^C \\ -\frac{\boldsymbol{p}_f^C}{\rho_0} \otimes \boldsymbol{N}_{ef} \\ -\frac{1}{\rho_0}\zeta_f^C \\ \boldsymbol{0} \end{bmatrix}, \tag{33}$$

where the numerical (contact) fluxes are obtained as

$$\boldsymbol{t}_f^C = \boldsymbol{t}_f^{\text{Ave}} + \boldsymbol{t}_f^{\text{Stab}} \tag{34a}$$

$$\boldsymbol{p}_f^C = \boldsymbol{p}_f^{\text{Ave}} + \boldsymbol{p}_f^{\text{Stab}} \tag{34b}$$

$$\zeta_f^C = \zeta_f^{\text{Ave}} + \zeta_f^{\text{Stab}}, \tag{34c}$$

with

$$\zeta_f^{\text{Ave}} = \frac{1}{2}\left(\boldsymbol{p}_f^- \cdot \boldsymbol{t}_f^- + \boldsymbol{p}_f^+ \cdot \boldsymbol{t}_f^+\right) \tag{35}$$

and the upwinding stabilisations

$$\boldsymbol{t}_f^{\text{Stab}} = \frac{1}{2}\left[c_p(\boldsymbol{n}_{ef} \otimes \boldsymbol{n}_{ef})(\boldsymbol{p}_f^+ - \boldsymbol{p}_f^-) + c_s(\boldsymbol{I} - \boldsymbol{n}_{ef} \otimes \boldsymbol{n}_{ef})(\boldsymbol{p}_f^+ - \boldsymbol{p}_f^-)\right]; \tag{36a}$$

$$\begin{aligned}\boldsymbol{p}_f^{\text{Stab}} = &\frac{1}{2}\left[\frac{1}{c_p}(\boldsymbol{n}_{ef} \otimes \boldsymbol{n}_{ef})(\boldsymbol{P}_f^+ - \boldsymbol{P}_f^-)\boldsymbol{N}_{ef}\right] \\ &+ \frac{1}{2}\left[\frac{1}{c_s}(\boldsymbol{I} - \boldsymbol{n}_{ef} \otimes \boldsymbol{n}_{ef})(\boldsymbol{P}_f^+ - \boldsymbol{P}_f^-)\boldsymbol{N}_{ef}\right];\end{aligned} \tag{36b}$$

$$\zeta_f^{\text{Stab}} = \boldsymbol{p}_f^{\text{Ave}} \cdot \boldsymbol{t}_f^{\text{Stab}} + \boldsymbol{t}_f^{\text{Ave}} \cdot \boldsymbol{p}_f^{\text{Stab}}. \tag{36c}$$

5. TIME INTEGRATION

Insofar as the resulting set of semi-discrete equations (18) is rather large, it will only be suitable to employ an explicit type of time integrator. For simplicity, an explicit one-step two-stage Total Variation Diminishing Runge-Kutta (TVD-RK) scheme has been used such as that presented in [1, 43, 46, 74]. This is described by the following time update equations from time step t^n to t^{n+1}:

$$\begin{aligned}\boldsymbol{\mathcal{U}}_e^\star &= \boldsymbol{\mathcal{U}}_e^n + \Delta t\, \dot{\boldsymbol{\mathcal{U}}}_e^n(\boldsymbol{\mathcal{U}}_e^n, t^n) \\ \boldsymbol{\mathcal{U}}_e^{\star\star} &= \boldsymbol{\mathcal{U}}_e^\star + \Delta t\, \dot{\boldsymbol{\mathcal{U}}}_e^\star(\boldsymbol{\mathcal{U}}_e^\star, t^{n+1}) \\ \boldsymbol{\mathcal{U}}_e^{n+1} &= \frac{1}{2}(\boldsymbol{\mathcal{U}}_e^n + \boldsymbol{\mathcal{U}}_e^{\star\star}).\end{aligned} \tag{37}$$

It is worthwhile to point out that one of the novelties introduced in this paper, in comparison with previous work by the authors where the geometry is updated through a standard trapezoidal integration procedure (e.g. $\boldsymbol{x}^{n+1} = \boldsymbol{x}^n + \frac{\Delta t}{2\rho_0}\left(\boldsymbol{p}^n + \boldsymbol{p}^{n+1}\right)$), is that the geometry is also updated through the TVD-RK algorithm. This results in a monolithic time integration procedure where the unknowns $\boldsymbol{\mathcal{U}} = \{\boldsymbol{p}, \boldsymbol{F}, E, \boldsymbol{x}\}$ are all updated through equation (37).

The maximum time step $\Delta t = t^{n+1} - t^n$ is governed by a standard Courant-Friedrichs-Lewy (CFL) condition [75] given as

$$\Delta t = \alpha_{\text{CFL}} \frac{h_{\text{min}}}{c_{\text{p,max}}} \tag{38}$$

where $c_{\text{p,max}}$ is the maximum p-wave speed (refer to Appendix A for its evaluation), h_{min} is the minimum (or characteristic) length within the computational domain and α_{CFL} is the CFL stability number. For the numerical computations presented in this paper, a value of $\alpha_{\text{CFL}} = 0.3$ has been chosen, unless otherwise stated, to ensure both accuracy and stability.

6. INVOLUTIONS: CONSTRAINED TRANSPORT SCHEMES

6.1. General remarks

Equation (7) represents a set of compatibility conditions, also known as involutions [76], that must be satisfied by the deformation gradient tensor throughout the deformation process. In the case of linear elasticity, these involutions are known as Saint Venant compatibility conditions [77][§]. The time rate of equation (7) leads to the following expression

$$\text{CURL}\dot{\boldsymbol{F}} = \mathbf{0}, \tag{39}$$

which establishes an equivalent set of involutions on the update of the deformation gradient tensor (refer to equation (20b)). These nine differential conditions in $\mathbb{R}^3$ need only be satisfied by the time-space evolution operator (20b) provided that they are met by the initial deformation gradient [76]. This implies that condition (7) (or (39)), as opposed to a classical constraint, is not necessary to close the system of conservation laws (11), but must be an inherent property of the evolution space-time operator.

One of the greatest challenges in designing a robust computational framework adapted to our mixed solid formulation is the ability to control spurious curl-error mechanisms over a long term response. Otherwise, these spurious modes can accumulate and lead to a breakdown of the numerical scheme. In the context Magnetohydrodynamics, a wide variety of numerical methodologies are available for the construction of transport schemes fulfilling the satisfaction of specific involutions [50, 51, 52, 53]. For instance, a first strategy is based on the use of a local involution-free projection scheme leading to the solution of a Poisson-type equation. This approach is known as elliptic correction [78] and relies upon the computation of an extra Lagrange multiplier parameter. A second strategy amends the conservation law equations via a convection-type correction [52], designed to advect spurious errors out of the computational domain. A final approach is based on the use of constrained transport algorithms [52, 50, 51], where the spatial discretisation is tailor-made to exactly satisfy the involutions by construction.

[§]In the case of linear elasticity, the compatibility equations can be written as curl(curl$\boldsymbol{\varepsilon}$) $= \mathbf{0}$ (in indicial notation $\mathcal{E}_{nml}\mathcal{E}_{ijk}\frac{\partial^2 \varepsilon_{lk}}{\partial x_j \partial x_m} = 0$), where $\boldsymbol{\varepsilon}$ represents the small strain tensor and the operator curl denotes the spatial curl operator.

Within the latter approach, a general framework for a locally curl-preserving finite volume method on two-dimensional structured quadrilateral grids was proposed by Torrilhon $et\ al.$ [50, 51] in the context of shallow water equations. This methodology was explored and expanded by the authors in [1] for the curl preservation of the deformation gradient tensor in two-dimensional structured quadrilateral grids.

In this paper, two new algorithms are introduced where the system of conservation laws is solved subjected to the fulfilment of the involutions (39). The first algorithm, named as constrained-TOUCH, relies on the extension of the constrained transport method presented in [1] to the case of three dimensional hexahedral elements where the overall scheme is recast into a Godunov-type method (see Section 6.2.1). The second algorithm, named as penalisation-TOUCH, follows some of the ideas presented in [44] leading to a penalisation-based finite volume algorithm (see Section 6.3). Finally, and for the sake of completeness, the nodal finite volume GLACE method of [2] is revisited and re-written in a Total Lagrangian manner so that numerical comparisons can then be established between the different schemes (see Section 6.2.2).

6.2. Curl-free Finite Volume Method

For the satisfaction of the involutions (39), the deformation gradient tensor $\boldsymbol{F}$ can be updated (6) in terms of a given nodal linear momentum distribution as [1, 50, 53, 51]

$$\frac{d\boldsymbol{F}_e}{dt} = \sum_{a\in\Lambda_e^a} \frac{\boldsymbol{p}_a}{\rho_0} \otimes \boldsymbol{\nabla}_0 N_a(\boldsymbol{X}_e), \tag{40}$$

where Λ_e^a represents the set of nodes a attached to cell e and $N_a(\boldsymbol{X}_e)$ represents the standard material finite element nodal shape function evaluated at the centroid of the cell e. Expression (40) is naturally curl-free as the evolution of $\boldsymbol{F}$ is formulated in terms of a material discrete gradient of a continuous velocity field. This update coincides with the classical finite element discretisation when considering linear interpolation with only one Gauss quadrature point at the centroid of the element. Analogously, above equation (40) can be re-expressed using the outward nodal area vector $\boldsymbol{C}_{ea}$ proposed by Després and Kluth [2, 70]

$$\frac{d\boldsymbol{F}_e}{dt} = \frac{1}{\Omega_0^e} \sum_{a\in\Lambda_e^a} \frac{\boldsymbol{p}_a}{\rho_0} \otimes \boldsymbol{C}_{ea}. \tag{41}$$

Upon the use of a simple averaging process, the nodal area vector can now be defined as $\boldsymbol{C}_{ea} = \frac{1}{\Lambda_a^f}\sum_{f\in\Lambda_a^f} \boldsymbol{C}_{ef}$, where Λ_a^f is the set of surfaces associated to a node a, leading to the following expression

$$\begin{aligned}
\frac{d\boldsymbol{F}_e}{dt} &= \frac{1}{\Omega_0^e} \sum_{a\in\Lambda_e^a} \frac{\boldsymbol{p}_a}{\rho_0} \otimes \left(\frac{1}{\Lambda_a^f} \sum_{f\in\Lambda_a^f} \boldsymbol{C}_{ef} \right) \\
&= \frac{1}{\Omega_0^e} \sum_{f\in\Lambda_e^f} \left(\frac{1}{\Lambda_f^a} \sum_{a\in\Lambda_f^a} \frac{\boldsymbol{p}_a}{\rho_0} \right) \otimes \boldsymbol{C}_{ef} \\
&= \frac{1}{\Omega_0^e} \sum_{f\in\Lambda_e^f} \frac{\tilde{\boldsymbol{p}}_f^C}{\rho_0} \otimes \boldsymbol{C}_{ef},
\end{aligned} \tag{42}$$

where $\tilde{\boldsymbol{p}}_f^C = \frac{1}{\Lambda_f^a} \sum_{a \in \Lambda_f^a} \boldsymbol{p}_a$. Here, Λ_e^f and Λ_f^a represent the set of faces associated to cell e and the set of nodes a associated to a face f, respectively, and $\tilde{\boldsymbol{p}}_f^C$, as yet to be defined, represents a 'filtering' interface linear momentum (different to the Riemann linear momentum $\boldsymbol{p}_f^C$ (34b)).

All in all, above equation (42) represents a Godunov-type update expressed in terms of an interface 'filtering' linear momentum. The question that remains is the computation of the nodal linear momentum distribution $\boldsymbol{p}_a$ (41), which will be the objective of the following two sections.

6.2.1. Godunov-type Finite Volume Method: constrained-TOUCH. For the evaluation of the filtering linear momentum $\tilde{\boldsymbol{p}}_f^C$, one of the strategies proposed in [1, 4] is to obtain nodal values by applying weighted average of the interface Riemann values as $\boldsymbol{p}_a = \frac{1}{\Lambda_a^f} \sum_{f \in \Lambda_a^f} \boldsymbol{p}_f^C$. In this case, certain corrections are required to enhance the accuracy near boundaries, as discussed in [1].

In this paper, we present a simpler approach for the computation of the filtering values $\tilde{\boldsymbol{p}}_f^C$. The whole process is illustrated in Algorithm 2 and, for clarity, its corresponding two-dimensional schematic diagram is depicted in Fig. 5.

Algorithm 2: Filtering contact linear momentum $\tilde{\boldsymbol{p}}_f^C$

Input : $\boldsymbol{p}_e$
Output: $\tilde{\boldsymbol{p}}_f^C$

(1) Evaluate contact linear momentum: $\boldsymbol{p}_f^C\left(\boldsymbol{p}_e\right) \leftarrow$ (34b)
(2) Obtain averaged linear momentum: $\tilde{\boldsymbol{p}}_e = \frac{1}{\Lambda_e^f} \sum_{f \in \Lambda_e^f} \boldsymbol{p}_f^C$
(3) Compute local gradient operator: $\boldsymbol{G}_e\left(\tilde{\boldsymbol{p}}_e, \boldsymbol{p}_f^C\right) \leftarrow$ (24)
(4) Apply slope limiter to the gradient operator: $\phi_e \leftarrow$ Section [4.2.2]
(5) Compute elemental nodal linear momentum: $\boldsymbol{p}_{ea} \leftarrow$ (26)
(6) Obtain continuous nodal linear momentum: $\boldsymbol{p}_a = \frac{1}{\Lambda_a^e} \sum_{e \in \Lambda_a^e} \boldsymbol{p}_{ea}$
(7) Interpolate filtering contact linear momentum: $\tilde{\boldsymbol{p}}_f^C = \frac{1}{\Lambda_f^a} \sum_{a \in \Lambda_f^a} \boldsymbol{p}_a$

6.2.2. Nodal-based Finite Volume Method: Total Lagrangian Hyperelastic-GLACE. Another curl-free approach, often known as 'nodal' Finite Volume Method [37, 71, 38, 70, 36, 39], has been successfully used in the numerical analysis of gas dynamics. Extension of the nodal solver to solid mechanics was introduced in [2] with the so-called Hyperelastic-GLACE scheme. In particular, an Updated Lagrangian mixed solid formulation was spatially discretised using a Lagrangian cell centred nodal scheme for the case of hyperelasticity.

In this section, and for comparison purposes with the approach presented above, we aim to adapt the Updated Lagrangian nodal scheme to the Total Lagrangian formalism pursued in this paper. Following the works of Després *et al.* [2] and Maire *et al.* [71], the nodal linear momentum $\boldsymbol{p}_a^C$ and the elemental nodal first Piola Kirchhoff stress $\boldsymbol{P}_{ea}^C$ are derived using the linear momentum jump conditon (3). The corresponding jump can be decomposed into the summation of normal and

tangential contributions defined by

$$c_p(\boldsymbol{n}_{ea} \otimes \boldsymbol{n}_{ea}) \left[\boldsymbol{p}_a^C - \boldsymbol{p}_{ea}\right] = -(\boldsymbol{n}_{ea} \otimes \boldsymbol{n}_{ea}) \left[\boldsymbol{P}_{ea}^C - \boldsymbol{P}_{ea}\right] \boldsymbol{N}_{ea} \tag{43a}$$

$$c_s(\boldsymbol{I} - \boldsymbol{n}_{ea} \otimes \boldsymbol{n}_{ea}) \left[\boldsymbol{p}_a^C - \boldsymbol{p}_{ea}\right] = -(\boldsymbol{I} - \boldsymbol{n}_{ea} \otimes \boldsymbol{n}_{ea}) \left[\boldsymbol{P}_{ea}^C - \boldsymbol{P}_{ea}\right] \boldsymbol{N}_{ea}. \tag{43b}$$

An additional nodal equilibrium condition can be established at every node, namely

$$\sum_{e \in \Lambda_a^e} \boldsymbol{P}_{ea}^C \boldsymbol{N}_{ea} = \boldsymbol{0}. \tag{44}$$

Upon substitution of (43a) and (43b) into (44), the nodal linear momentum $\boldsymbol{p}_a^C$ can be found as

$$\boldsymbol{A}_e \boldsymbol{p}_a^C = \boldsymbol{b}_e, \tag{45}$$

where

$$\boldsymbol{A}_e = \sum_{e \in \Lambda_a^e} c_p \left(\boldsymbol{n}_{ea} \otimes \boldsymbol{n}_{ea}\right) + c_s \left(\boldsymbol{I} - \boldsymbol{n}_{ea} \otimes \boldsymbol{n}_{ea}\right) \tag{46}$$

and

$$\boldsymbol{b}_e = \sum_{e \in \Lambda_a^e} \left[c_p \left(\boldsymbol{n}_{ea} \otimes \boldsymbol{n}_{ea}\right) + c_s \left(\boldsymbol{I} - \boldsymbol{n}_{ea} \otimes \boldsymbol{n}_{ea}\right)\right] \boldsymbol{p}_{ea} + \sum_{e \in \Lambda_a^e} \boldsymbol{P}_{ea} \boldsymbol{N}_{ea}. \tag{47}$$

By combining (43a) and (43b), the elemental nodal traction $\boldsymbol{t}_{ea}^C$ is finally obtained as

$$\boldsymbol{t}_{ea}^C := \boldsymbol{P}_{ea}^c \boldsymbol{N}_{ea} = \boldsymbol{P}_{ea} \boldsymbol{N}_{ea} + \left[c_p \left(\boldsymbol{n}_{ea} \otimes \boldsymbol{n}_{ea}\right) + c_s \left(\boldsymbol{I} - \boldsymbol{n}_{ea} \otimes \boldsymbol{n}_{ea}\right)\right] \left[\boldsymbol{p}_{ea} - \boldsymbol{p}_a^C\right]. \tag{48}$$

For completeness, the system of semi-discrete nodal updates for the set of conservation variables presented in this paper (i.e. linear momentum, deformation gradient, total energy and geometry) reads

$$\frac{d\boldsymbol{p}_e}{dt} = \frac{1}{\Omega_0^e} \sum_{a \in \Lambda_e^a} \boldsymbol{t}_{ea}^C \|\boldsymbol{C}_{ea}\| \tag{49a}$$

$$\frac{d\boldsymbol{F}_e}{dt} = \frac{1}{\Omega_0^e} \sum_{a \in \Lambda_e^a} \frac{\boldsymbol{p}_a^C}{\rho_0} \otimes \boldsymbol{C}_{ea} \tag{49b}$$

$$\frac{dE_e}{dt} = \frac{1}{\Omega_0^e} \sum_{a \in \Lambda_e^a} \frac{\boldsymbol{p}_a^C}{\rho_0} \cdot \boldsymbol{t}_{ea}^C \|\boldsymbol{C}_{ea}\| \tag{49c}$$

$$\frac{d\boldsymbol{x}_a}{dt} = \frac{\boldsymbol{p}_a}{\rho_0}. \tag{49d}$$

6.3. Penalisation-based Finite Volume Method: penalisation-TOUCH

Following recent work by the authors [45, 47, 48, 44], an alternative penalisation-based method is presented for the first time in the context of the finite volume scheme. In this approach, a residual-based artificial diffusion is added into the fibre map evolution (6). The main aim of this technique is to control the accumulation of non-physical curl errors, whilst still preserving the standard finite volume update for the fibre map evolution (20b), without the need to resort to filtering interface values of the linear momentum.

For this reason, within each stage of the two-stage TVD Runge Kutta time integrator (37), an augmented deformation gradient is introduced by incorporating an additional geometrical penalisation, with the aim at eliminating curl spurious modes as follows

$$\boldsymbol{F}_e^{\chi} = \boldsymbol{F}_e^{\gamma} + \frac{\Delta t}{\Omega_0^e} \sum_{f \in \Lambda_e^f} \left(\frac{\boldsymbol{p}_f^{C,\gamma}}{\rho_0} \right) \otimes \boldsymbol{C}_{ef} + \xi_{\boldsymbol{F}} \underbrace{\left(\frac{1}{\Omega_0^e} \sum_{f \in \Lambda_e^f} \boldsymbol{x}_f^{\gamma} \otimes \boldsymbol{C}_{ef} - \boldsymbol{F}_e^{\gamma} \right)}_{\text{Penalisation}}, \tag{50}$$

where $\chi = \{*, **\}$ and $\gamma = \{n, *\}$. The non-dimensional parameter $\xi_{\boldsymbol{F}}$ is usually defined in the range of $[0, 0.5]$ [45, 47, 48, 44]. Notice that $\xi_{\boldsymbol{F}} = 0$ recovers the standard finite volume update (20b), whereas $\xi_{\boldsymbol{F}} = 1$ leads to an overly stiff behaviour [45, 44].

7. DISCRETE ANGULAR MOMENTUM PROJECTION ALGORITHM

Any of the family of algorithms presented above, namely constrained (or penalised) Godunov-type algorithms (20a), (20c), (20d) and (42) or the nodal solver algorithm (49a)-(49d) [70], do not intrinsically fulfil conservation of angular momentum, as the deformation gradient $\boldsymbol{F}$ is no longer 'strongly' obtained as the material gradient of the current geometry (e.g. $\boldsymbol{F} \neq \boldsymbol{F}_{\boldsymbol{x}} := \boldsymbol{\nabla}_0 \boldsymbol{x}$) [1].

To remedy this, a projection-based method was presented by the authors in [1, 46] where the interface contact tractions were appropriately modified to guarantee global angular momentum preservation. This approach, however, implies a modification of the interface contact tractions which can affect the overall stability/accuracy of the scheme as a result of a reduction/increase in the numerical dissipation introduced by the interface fluxes. An alternative approach has been recently proposed by Després and Labourasse [70], which incorporates an additional angular momentum conservation law into the finite volume nodal solver system (49a)-(49d). The use of this extra conservation law in conjunction with a local linear reconstruction procedure within every cell is shown to lead, via the use of a Lagrange multiplier, to the preservation of the angular momentum.

In this paper, and following the work in [43], a new variant of the discrete angular momentum projection algorithm is carried out. Unlike the previous approaches proposed by the authors [1, 45], in this paper the local linear momentum update $\dot{\boldsymbol{p}}$ is modified (in the least squares sense) in order to preserve the total angular momentum, whilst still ensuring the conservation of the overall linear momentum.

In the absence of external tractions[¶], the conservation of the discrete angular momentum after a time step can be written as

$$\sum_e \Omega_0^e \boldsymbol{x}_e^{n+1} \times \boldsymbol{p}_e^{n+1} - \sum_e \Omega_0^e \boldsymbol{x}_e^{n} \times \boldsymbol{p}_e^{n} = \boldsymbol{0}. \tag{51}$$

[¶]Consideration of external tractions has been disregarded for simplicity in this derivation. However, addition of torques can be carried out in a straightforward manner. This has been done, wherever necessary, for the numerical examples presented in this paper.

By taking into account the one-step two-stage TVD Runge-Kutta time integrator for the time integration of the geometry (see equation (37)), the above equation can be rewritten as[‖]

$$\sum_e \Omega_0^e \boldsymbol{x}_e^{n+1/2} \times \left(\boldsymbol{p}_e^{n+1} - \boldsymbol{p}_e^n\right) + \frac{\Delta t}{2\rho_0} \sum_e \Omega_0^e \boldsymbol{p}_e^\star \times \boldsymbol{p}_e^{n+1} = \boldsymbol{0}; \quad \boldsymbol{x}_e^{n+1/2} = \boldsymbol{x}_e^n + \frac{\Delta t}{2\rho_0} \boldsymbol{p}_e^n. \tag{52}$$

Equivalently, the above equation can be re-expressed as

$$\sum_e \Omega_0^e \left(\boldsymbol{x}_e^{n+1/2} + \frac{\Delta t}{2\rho_0} \boldsymbol{p}_e^\star\right) \times \left(\boldsymbol{p}_e^{n+1} - \boldsymbol{p}_e^n\right) - \frac{\Delta t}{2\rho_0} \sum_e \Omega_0^e \boldsymbol{p}_e^\star \times (\boldsymbol{p}_e^\star - \boldsymbol{p}_e^n) = \boldsymbol{0}. \tag{53}$$

Considering the TVD Runge-Kutta time integration as presented in equation (37), the linear momentum increment reads

$$\boldsymbol{p}_e^{n+1} - \boldsymbol{p}_e^n = \frac{\Delta t}{2} \left(\dot{\boldsymbol{p}}_e^n + \dot{\boldsymbol{p}}_e^\star\right); \qquad \boldsymbol{p}_e^\star - \boldsymbol{p}_e^n = \Delta t \, \dot{\boldsymbol{p}}_e^n, \tag{54}$$

Substituting (54) into (53), the following equation is obtained after some algebraic manipulations

$$\sum_e \Omega_0^e \boldsymbol{x}_e^n \times \dot{\boldsymbol{p}}_e^n + \sum_e \Omega_0^e \left(\boldsymbol{x}_e^{n+1/2} + \frac{\Delta t}{2\rho_0} \boldsymbol{p}_e^\star\right) \times \dot{\boldsymbol{p}}_e^\star = \boldsymbol{0}. \tag{55}$$

Sufficient conditions to satisfy expression (55) within a time step are enforced at each stage of the two-stage Runge Kutta time integrator described as

$$\sum_e \Omega_0^e \left(\mathscr{X}_e \times \dot{\boldsymbol{p}}^\chi\right) = \boldsymbol{0}; \qquad \forall \chi = \{n, \star\} \tag{56}$$

where

$$\mathscr{X}_e = \begin{cases} \boldsymbol{x}_e^n, & \chi = n \\ \boldsymbol{x}_e^{n+1/2} + \frac{\Delta t}{2\rho_0} \boldsymbol{p}_e^\star, & \chi = \star. \end{cases} \tag{57}$$

A Lagrangian projection procedure is used to ensure the satisfaction of the momentum constraints (56), as well as the conservation of linear momentum (1). This can be achieved by considering the minimisation of the following functional Π as[**]:

$$\begin{aligned} \Pi(\dot{\boldsymbol{p}}_e^C, \boldsymbol{\lambda}_{\text{Ang}}, \boldsymbol{\lambda}_{\text{Lin}}) = \frac{1}{2} \sum_e \Omega_0^e \left(\dot{\boldsymbol{p}}_e^C - \dot{\boldsymbol{p}}_e\right) \cdot \left(\dot{\boldsymbol{p}}_e^C - \dot{\boldsymbol{p}}_e\right) - \boldsymbol{\lambda}_{\text{Ang}} \cdot \left[\sum_e \Omega_0^e \left(\mathscr{X}_e \times \dot{\boldsymbol{p}}_e^C\right)\right] \\ + \boldsymbol{\lambda}_{\text{Lin}} \cdot \left[\sum_e \left(\boldsymbol{T}_{\text{Force}}^e - \Omega_0^e \dot{\boldsymbol{p}}_e^C\right)\right]. \end{aligned} \tag{58}$$

Here, $\dot{\boldsymbol{p}}_e^C$ indicates the enhanced time variation of the elemental linear momentum, $\{\boldsymbol{\lambda}_{\text{Ang}}, \boldsymbol{\lambda}_{\text{Lin}}\}$ are two global Lagrange multiplier vectors associated with the angular momentum constraint and the linear momentum constraint, and the elemental force $\boldsymbol{T}_{\text{Force}}^e = \sum_{f \in \Lambda_e^f} \boldsymbol{t}_f^C \| \boldsymbol{C}_{ef} \| + \rho_0 \boldsymbol{b}_e$.

[‖] As reported in [1, 45, 47, 48, 43, 46, 44], expression (52) simplifies to to $\sum_e \Omega_0^e \boldsymbol{x}_e^{n+1/2} \times \left(\boldsymbol{p}_e^{n+1} - \boldsymbol{p}_e^n\right) = \boldsymbol{0}$, when using the trapezoidal time integrator for the geometry.

[**] The upper indices indicating time step (e.g. $n, n+1/2, *$) have been removed for simplicity.

After some algebraic manipulations, a modified set of the time variation of the linear momentum is obtained as

$$\dot{\boldsymbol{p}}_e^C = \dot{\boldsymbol{p}}_e + \boldsymbol{\lambda}_{\text{Ang}} \times \mathscr{X}_e + \boldsymbol{\lambda}_{\text{Lin}}. \tag{59}$$

The Lagrange multipliers $\{\boldsymbol{\lambda}_{\text{Ang}}, \boldsymbol{\lambda}_{\text{Lin}}\}$ are the solutions of the following system of equations

$$\left(\sum_e \Omega_0^e \left[(\mathscr{X}_e \cdot \mathscr{X}_e)\boldsymbol{I} - \mathscr{X}_e \otimes \mathscr{X}_e\right]\right) \boldsymbol{\lambda}_{\text{Ang}} + \left(\sum_e \Omega_0^e \hat{\mathscr{X}}_e\right) \boldsymbol{\lambda}_{\text{Lin}} = -\sum_e \Omega_0^e \mathscr{X}_e \times \dot{\boldsymbol{p}}_e \tag{60a}$$

$$\left(\sum_e \Omega_0^e \hat{\mathscr{X}}_e\right) \boldsymbol{\lambda}_{\text{Ang}} - \left(\sum_e \Omega_0^e\right) \boldsymbol{\lambda}_{\text{Lin}} = \sum_e \left(\Omega_0^e \dot{\boldsymbol{p}}_e - \boldsymbol{T}^e_{\text{Force}}\right), \tag{60b}$$

with the indicial notation $\left[\hat{\mathscr{X}}_e\right]_{ik} = \mathcal{E}_{ijk} \left[\mathscr{X}_e\right]_j$.

8. ALGORITHM DESCRIPTION

For ease of understanding, Algorithm 3 summarises the complete algorithmic description of the proposed TOUCH methodology with all the necessary numerical ingredients.

9. NUMERICAL EXAMPLES

In this section, a series of numerical examples are presented in order to assess the robustness, effectiveness and applicability of the mixed $\{\boldsymbol{p}, \boldsymbol{F}\}$ Cell Centred Finite Volume (CCFVM) based computational frameworks described above. Notice that even though the total energy of the system E is computed as an additional conservation variable (for dissipation monitoring purposes), it is not coupled with the rest of the conservation variables. Unavoidably, the new set of unknowns leads to an increase in the number of degrees of freedom with respect to traditional formulations. However, the cell centred approach, with only one flux evaluation per face, makes it still very efficient. In addition, it is crucial to notice the explicit nature of the time integrator, which makes feasible the possibility of considering the extra number of degrees of freedom. More importantly, taking advantage of the open source "OpenFOAM", the proposed algorithm can then be parallelised enabling the simulation of large scale real life problems.

Three $\{\boldsymbol{p}, \boldsymbol{F}\}$ CCFVM methods will be analysed, namely constrained-based TOUCH (see Section 6.2.1), penalised-based TOUCH (see Section 6.3) and Total Lagrangian Hyperelastic-GLACE scheme (see Section 6.2.2). Moreover, and for comparison purposes, some results will be benchmarked against the well-known B-bar and the Ladyzhenskaya-Babuška-Brezzi (LBB) compliant Q2-Q1 element (i.e. Taylor-Hood element) [20], as well as a comprehensive library of alternative numerical methodologies developed by the authors. Specifically, we will compare against the Finite Volume based $\{\boldsymbol{p}, \boldsymbol{F}\}$ Upwind Vertex Centred (Upwind-VCFVM) [46] and the $\{\boldsymbol{p}, \boldsymbol{F}\}$ Jameson-Schmidt-Turkel Vertex Centred (JST-VCFVM) [43], to analyse the performance of the cell centred scheme against well-known vertex centred competitors.

Algorithm 3: Time update of conservation variables

Input : $\boldsymbol{\mathcal{U}}_e^n$ where $\boldsymbol{\mathcal{U}} = [\boldsymbol{p}\ \boldsymbol{F}\ E\ \boldsymbol{x}]^T$

Output: $\boldsymbol{\mathcal{U}}_e^{n+1}$, $\boldsymbol{P}_e^{n+1}$

(1) Calculate time step: $\Delta t^n \leftarrow$ (38)

(2) Store conservation variables: $\boldsymbol{\mathcal{U}}_e^{old} = \boldsymbol{\mathcal{U}}_e^n$

for *Runge Kutta stage* $= 1$ **to** 2 **do**

(3) Evaluate wave speeds: $c_p,\ c_s \leftarrow$ (76)

(4) Compute PK1 stresses: $\boldsymbol{P}_e \leftarrow$ (16)

(5) Apply the linear reconstruction procedure:

(5.1) Evaluate gradients of $\boldsymbol{p}_e$ and $\boldsymbol{P}_e \leftarrow$ (24)

(5.2) Apply slope limiter ϕ_e to Step (5.1) $\leftarrow$ Section [4.2.2]

(5.3) Obtain reconstructed values at faces: $\mathcal{U}_f^-,\ \mathcal{U}_f^+ \leftarrow$ (25)

(6) Apply Acoustic Riemann solver: $\boldsymbol{t}_f^C \leftarrow$ (34a), $\boldsymbol{p}_f^C \leftarrow$ (34b)

(7) Ensure a curl-free Finite Volume Method (Section [6])

(7.1) Evaluate nodal linear momentum $\boldsymbol{p}_a$

(7.2) Enforce strong boundary conditions on $\boldsymbol{p}_a$

(7.3) Obtain filtering contact linear momentum: $\tilde{\boldsymbol{p}}_f^C = \frac{1}{\Lambda_f^a} \sum_{a \in \Lambda_f^a} \boldsymbol{p}_a$

(8) Compute time derivative of linear momentum: $\dot{\boldsymbol{p}}_e \leftarrow$ (20a)

(9) Apply angular momentum projection algorithm $\leftarrow$ Section [7]

(10) Solve governing equations: $\boldsymbol{\mathcal{U}}_e = \boldsymbol{\mathcal{U}}_e + \Delta t^n \dot{\boldsymbol{\mathcal{U}}}_e$

end

(11) Update conservation variables: $\boldsymbol{\mathcal{U}}_e^{n+1} = \frac{1}{2}(\boldsymbol{\mathcal{U}}_e + \boldsymbol{\mathcal{U}}_e^{old})$

(12) Compute PK1 stresses: $\boldsymbol{P}_e^{n+1} \leftarrow$ (16)

In addition, a Petrov-Galerkin Finite Element Method (PG-FEM) $\{\boldsymbol{p}, \boldsymbol{F}, J\}$ formulation will also be used, where the extra conservation variable J is proven to be necessary, in terms of robustness, in nearly incompressible simulations [47]. This will enable to compare against a completely different spatial discretisation method. Finally, a very sophisticated LBB compliant Hu-Washizu $\{\boldsymbol{v}, \boldsymbol{\Sigma_F}, \boldsymbol{\Sigma_H}, \Sigma_J\}$ complementary mixed Finite Element formulation will be used (see [54] for further details).

In the following numerical computations, unless otherwise stated, a piecewise linear reconstruction (see Section 4.2.1), slope limiter (see Section 4.2.2), as well as the discrete Angular Momentum Projection Algorithm (see Section 7) are activated when using the proposed TOUCH schemes.

9.1. Elastic cable

This example presents the analysis of a wave propagation problem in a one dimensional linear elastic cable (see Fig. 6). The $L = 10$ m long bar is fixed at one end ($x = 0$), whilst a forcing function is applied at the other free end ($x = L$). Upon the application of the external force, a stress wave propagates across the bar towards the left and then reflects off the fixed end. In this particular case, two different forcing functions will be assessed, namely: (a) Step function loading (see Section 9.1.1); and (b) Smooth sinusoidal loading (see Section 9.1.2).

9.1.1. Step function loading. The first part of this example deals with the wave propagation under the influence of a shock. The linear elastic material has density $\rho_0 = 8000$ kg/m^3, Young's modulus $E = 200$ GPa and Poisson's ratio $\nu = 0$. A step loading is applied which can be mathematically expressed as follows

$$P(L,t) = \begin{cases} 0 & \text{t} < 0 \\ -5 \times 10^7 \text{ Pa} & \text{t} \geq 0. \end{cases} \tag{61}$$

For comparison purposes, the numerical solution obtained using the in-house Jameson-Schmidt-Turkel (JST) vertex centred FVM [43] is also displayed. Fig. 7a shows the evolution of the stress wave at the middle of the cable $L = 5$ m. It can be clearly seen that the first order TOUCH scheme[††] (i.e. discretised with a piecewise constant reconstruction along with the forward Euler time integrator) introduces excessive numerical dissipation. To overcome this, a linear reconstruction procedure together with the use of the two-stage TVD-RK time integrator (see Section 5) is employed. Insofar as the scheme is not monotonicity preserving, oscillations would be observed in the vicinity of the shock. These deficiencies can be eliminated to a great extent with the introduction of a slope limiter (see Section 4.2.2). For the sake of clarity, a magnified view of the shock is depicted in Fig. 7b.

9.1.2. Smooth sinusoidal loading. To assess the convergence behaviour of the proposed formulation, the same problem is repeated but this time with the imposition of a smooth sinusoidal loading defined as

$$P(L,t) = \begin{cases} 0 & \text{t} < 0 \\ 0.001\left[\sin\left(\pi t/20 - \pi/2\right) + 1\right] \text{ Pa} & \text{t} \geq 0. \end{cases} \tag{62}$$

The material parameters used are density $\rho_0 = 1$ kg/m^3, Young's modulus $E = 1$ Pa and Poisson's ratio $\nu = 0.3$. The mesh convergence analysis is shown in Fig. 8. It is clear that an optimal equal order of convergence for the velocities and stresses can be obtained when using either the first order or the second order methodology. For problems where the accurate evaluation of the stresses is of special importance (i.e. onset of plastic yielding), this is certainly one of the greatest advantages of employing this mixed formulation in comparison with a displacement based approach, where stresses converge at a lower order of accuracy.

[††] As in a one-dimensional setting, satisfaction of involutions is guaranteed ab initio, the TOUCH scheme does not require the filtering of the linear momentum field.

9.2. Low dispersion cube

As presented in [48, 49, 46, 27, 43, 47], this example shows a cube of unit side with symmetric boundary conditions (roller supports) at faces $X = 0$, $Y = 0$ and $Z = 0$ and skew-symmetric boundary conditions (restricted tangential displacement) at faces $X = 1$m, $Y = 1$m and $Z = 1$m (see Fig. 9). For small deformations, the problem has a closed-form displacement field of the form

$$\boldsymbol{u}(\boldsymbol{X},t) = U_0 \cos\left(\frac{\sqrt{3}}{2} c_d \pi t\right) \begin{bmatrix} A\sin\left(\frac{\pi X_1}{2}\right)\cos\left(\frac{\pi X_2}{2}\right)\cos\left(\frac{\pi X_3}{2}\right) \\ B\cos\left(\frac{\pi X_1}{2}\right)\sin\left(\frac{\pi X_2}{2}\right)\cos\left(\frac{\pi X_3}{2}\right) \\ C\cos\left(\frac{\pi X_1}{2}\right)\cos\left(\frac{\pi X_2}{2}\right)\sin\left(\frac{\pi X_3}{2}\right) \end{bmatrix}; \quad c_d = \sqrt{\frac{\lambda + 2\mu}{\rho_0}}. \tag{63}$$

Parameters $\{A, B, C\}$ are user-defined arbitrary constants, chosen such that A=B=C. This ensures the existence of a non-zero pressure field, a slight difference with respect to the closed-form solutions previously reported in References [43, 46, 47, 48, 49][‡‡]. For values of U_0 below 0.001 m, the solution can be considered to be linear and the closed-form expression (63) holds. The problem is initialised with a known deformation gradient field $\boldsymbol{F}(\boldsymbol{X}, 0) = \boldsymbol{I} + \boldsymbol{\nabla}_0 \boldsymbol{u}$ and a linear elastic material is chosen with a Poisson's ratio of $\nu = (1 - \mu/\kappa)/2 = 0.3$, Young's modulus $E = 1.7 \times 10^7$ Pa and density $\rho_0 = 1.1 \times 10^3$ kg/m^3. The solution parameters are set as A=B=C=1 and $U_0 = 5 \times 10^{-4}$ m.

The main aim of this example is to demonstrate the convergence behaviour of the proposed constrained- and penalisation-based TOUCH schemes in three dimensions. Fig. 10 and Fig. 11 show the expected second order convergence pattern (L^1 and L^2 norm errors) of the linear momentum $\boldsymbol{p}$ and the first Piola-Kirchhoff stress tensor $\boldsymbol{P}$ (both deviatoric and volumetric components) as compared to the analytical solution given in (63). For completeness, we simulate the exact same problem using the classical B-bar hexahedral element, clearly resulting in a reduced order of convergence (i.e. first order accuracy) for the stresses (see Fig.12).

9.3. Spinning plate

We consider a unit square plate which is free on all sides [1, 44]. The plate is initialised with a constant angular velocity of $\boldsymbol{\omega}_0 = [0, 0, 105]^T$ rad/s relative to the origin and is then left rotating in space (see Fig. 13). A nearly incompressible neo-Hookean material is utilised with the following material properties, namely, density $\rho_0 = 1100$ kg/m^3, Youngs's modulus $E = 17$ MPa and Poisson's ratio $\nu = 0.45$. The main objective of this example is to show that the constrained-TOUCH scheme is capable of handling unstructured meshes. A comparison of the deformed shapes plotted with pressure resolution is depicted in Fig. 14 using both structured and unstructured meshes. For qualitative comparison, the time evolution of x and y displacements at corner point $X = [0.5, 0.5, 0]^T$ are also minotored (see Fig. 15). Both meshes show very good agreement in terms of pressure and also the deformations.

[‡‡]Relationship $A + B + C = 0$ and parameter $c_d = \sqrt{\frac{\mu}{\rho_0}}$ have been used in previous publications [43, 46, 47, 48, 49] leading to a non-volumetric deformation field.

9.4. L-shaped block

In this example we present an L-shaped block (see Fig. 16) which was first introduced by Simo and Tarnow [79] and later in [80, 81, 82, 43, 48, 46]. The block is subjected to time varying forces on two of its sides and is then left floating in space

$$\boldsymbol{F}_1(t) = -\boldsymbol{F}_2(t) = (150, 300, 450)^T\, p(t), \qquad p(t) = \begin{cases} t & 0 \le t < 2.5 \\ 5 - t & 2.5 \le t < 5 \\ 0 & t \ge 5. \end{cases}$$

A neo-Hookean material is considered with density $\rho_0 = 1000$ kg/m^3, Young's modulus $E = 50.05$ kPa and Poisson's ratio $\nu = 0.3$.

The main aim of this example is to demonstrate the preservation of total angular momentum. Fig. 17 shows the time evolution of the deformation during and after the application of the external force, with very smooth pressure contours. A mesh refinement study for structured cube elements is carried out at time $t = 7.5$ s along with the pressure distribution (see Fig. 18), which is shown to be smooth. Fig. 19 shows alternative mesh refinement study for structured cuboid mesh with different aspect ratio. Crucially, all meshes provide practically identical results. Fig. 20a shows the time evolution of the components of angular momentum with and without the consideration of the angular momentum projection algorithm (see Section 7). As can be observed, without the use of the projection algorithm, the block rapidly decelerates until it reaches a standstill. This is in contrast to the perfectly captured behaviour of the block which correctly exhibits no change in angular momentum (after the external loading ceases) when the projection algorithm is employed. Fig. 20b illustrates the conservation of linear momentum, which is zero to machine accuracy. It is worthwhile to highlight that the amount of numerical dissipation introduced by the proposed algorithm can be accurately measured by considering the total energy conservation equation (10). As expected and shown in Fig. 21, the amount of numerical dissipation decreases with the reduction in mesh size.

9.5. Bending column

Following References [43, 47, 46, 45, 1, 48], this example shows a 1 m squared cross section column clamped at the bottom and free on all other sides. The main objective of this example is to demonstrate the performance of the proposed schemes in nearly incompressible bending dominated scenarios. An initial linear variation of the velocity profile is prescribed in the X-Y plane given by $v_0 = V[Y/L, 0, 0]^T$, where $V = 10$ m/s and $L = 6$ m is the length of the column. A nearly incompressible neo-Hookean constitutive law is used where the material parameters are density $\rho = 1100$ kg/m^3, Young's modulus $E = 17$ MPa and Poisson's ratio $\nu = 0.45$. For comparison purposes, an ample spectrum of alternative numerical strategies will be employed, namely $\{\boldsymbol{p}, \boldsymbol{F}\}$ Hyperelastic-GLACE [2], JST-VCFVM [43], Upwind-VCFVM [46], $\{\boldsymbol{p}, \boldsymbol{F}, J\}$ PG-FEM [45, 47, 48], the classical B-bar hexahedral element [3] and Hu-Washizu type variational principle [65].

Fig. 23 depicts a sequence of locking-free deformed shapes for the column under consideration without the appearance of spurious pressure instabilities by using the constrained-TOUCH scheme. The pressure field is plotted constant per cell without resorting to any sort of visual nodal

interpolation. Very similar results are observed by using the penalised-TOUCH approach and hence not shown. It is remarkable the excellent locking-free behaviour and pressure contour observed despite employing only four elements (control volumes) across the thickness.

Fig. 24 demonstrates the importance of performing an accurate reconstruction procedure near the fixed boundary (clamped bottom side). As can observed in Fig. 24a, the use of a standard reconstruction procedure (i.e. standard least square gradient scheme used in OpenFOAM [32]) leads to the appearance of hourglassing-type instabilities, which can lead to the breakdown of the numerical simulation over time specially when dealing with nearly incompressible materials. This is in contrast to the smooth profile displayed in Fig. 24b, where an enhanced reconstruction procedure is used by taking into account the condition of fixed boundary when evaluating the local gradient.

A mesh refinement study is shown in Fig. 25 and a time evolution diagram of the horizontal component of the displacement measured at the tip of the column $\boldsymbol{X} = [0.5, 6, 0.5]^T$ is monitored in Fig. 26. In this latter Figure, results are presented for the proposed constrained-TOUCH methodology and the Total Lagrangian Hyperelastic-GLACE nodal scheme for three different mesh sizes. As can be clearly observed, both computational methodologies converge to the same result when the mesh is refined, as it is seen from the result obtained with the mesh of $16 \times 96 \times 16$ hexahedral elements.

For completeness, Fig. 27 compares the deformed shape and the pressure contour for eight different methodologies, namely (a) Constrained-TOUCH; (b) Penalised-TOUCH ($\xi_{\boldsymbol{F}} = 0.1$); (c) Hyperelastic-GLACE [2]; (d) Classical B-bar method [3]; (e) Upwind-VCFVM [46]; (f) JST-VCFVM [43]; (g) PG-FEM [45]; and (h) Hu-Washizu type variational principle [54].

Results displayed for the cell centred approaches (see Fig. 27a-c) have been obtained with a slightly finer discretisation to that of the other techniques (due to the higher numerical dissipation of the cell centred schemes). As can be observed, the results of the schemes proposed in this paper match very well those of the other in-house methodologies, where the $\{\boldsymbol{p}, \boldsymbol{F}, J\}$ PG-FEM scheme displays a slight over-diffusion of the pressure field near the clamped boundary. The latter can be attributed to the higher number of stabilisation parameters involved in the formulation [47] which would require an in-depth selection procedure.

9.6. Twisting column

In order to illustrate the applicability and robustness of the scheme, the 1 m squared cross section twisting column problem already presented in References [47, 48, 54, 43, 46] is considered. The problem is initialised with a sinusoidal angular velocity field (see Fig. 28) relative to the origin given by $\omega_0 = [0, \Omega \sin(\pi Y/2L), 0]^T$, where $\Omega = 105$ rad/s and $L = 6$ m is the length of the column. A nearly incompressible neo-Hookean material is used and the material parameters are: density $\rho_0 = 1100$ kg/m^3, Youngs's modulus $E = 17$ MPa and Poisson's ratio $\nu = 0.45$.

Fig. 29 shows the deformation sequence along with the pressure distribution when using the constrained-TOUCH scheme. The pressure field is plotted constant per cell without resorting to any sort of visual nodal interpolation and, once again, no pressure instabilities can be observed. It is again remarkable the excellent locking-free behaviour and pressure contour observed despite employing only four elements (control volumes) across the thickness.

The discontinuous cell-wise pressure pattern contour displayed along the longitudinal direction of the domain does not correspond to a spurious mode, as it gets eliminated after refinement of

the mesh (see Fig. 30). Notice that spurious pressure checkerboard modes can never be alleviated by increasing the mesh density (due to dissatisfaction of the LBB condition). It is important to emphasise that a nodal averaging (smoothing) process could have been used to display the results (see Fig. 30b). However, it is known that this can lead to the removal of possible spurious oscillations, which is why we have explicitly decided not to do so.

A comparison between the proposed constrained-TOUCH algorithm and the adapted Total Lagrangian nodal Hyperelastic-GLACE scheme [2] is shown in Fig. 31a-b. The Total Lagrangian Hyperelastic-GLACE nodal scheme seems to be more dissipative as it misses one twist when a coarse mesh is used (see Fig. 31b). However, the results can be significantly improved by increasing the density of the mesh (see Fig. 31c). A mesh refinement analysis of the constrained-TOUCH scheme is also shown in Fig. 32, where very smooth pressure results can be observed. It is also interesting to notice how the methodology preserves perfect axial rotation introducing no out-of-axis characteristics. Other formulations [43] have in contrast been found to introduce out-of-axis characteristics, due to excessive or unbalanced numerical dissipation.

Fig. 33 has been included to clearly show that the use of the classical finite volume update (see Section 6) clearly introduces curl-errors which accumulate over time leading to non-physical results and the final breakdown of the solution. This Figure emphasises that the standard CCFVM cannot be used in the context of large strain solid dynamics and the consideration of curl-free algorithms is of paramount importance.

For completeness, and for benchmarking purposes, we simulate the exact same problem in Fig. 34 using other available methodologies, namely Hyperelastic-GLACE [2], PG-FEM [45, 47, 48], JST-VCFVM [43], Upwind-VCFVM [46], the classical B-bar, the LBB compliant Q2-Q1 hexahedral element [3] and Hu-Washizu type mixed formulation [54]. Results displayed in columns (a) Constrained-TOUCH, (b) Penalised-TOUCH and (c) Hyperelastic-GLACE have been obtained with a slightly finer discretisation to that of the other techniques (due to the higher numerical dissipation of the cell centred schemes). It can be observed that the deformation patterns predicted by the family of numerical mixed methodologies are practically identical, apart from a slight out-of-plane deformation introduced by the JST-VCFVM. Pressure contour displayed by using the B-bar method are shown per cell and not nodally interpolated. This is sometimes done in order to smooth possible pressure oscillations of this element [3].

Fig. 35 includes a similar comparative study, with a reduced number of methodologies and with a higher Poisson's ratio of value $\nu = 0.495$, which can be considered as very nearly incompressible. Crucially, all computational mixed methodologies presented produce very similar deformation patterns with smooth pressure distribution and absence of locking. Here again, the results obtained with the TOUCH schemes (a)-(b) have been obtained with a slightly finer mesh.

In this case ($\nu = 0.495$), the simulation could not be run with the JST-VCFVM, the Upwind-VCFVM and Hyperelastic-Glace schemes, due to lack of robustness for this high Poisson's ratio. For high values of the Poisson's ratio, a new additional conservation law is necessary, as already reported by the authors in previous publications [47]. Remarkably, both TOUCH schemes were capable of simulating this problem without the need to resort to an additional conservation law for the Jacobian. However, for extremely high values of the Poisson's ratio beyond $\nu = 0.495$, an extra conservation law for J is necessary and will be the focus of future publications.

9.7. Taylor impact plasticity

A copper bar, of initial length 0.03 m with a squared cross section of 0.006×0.006 m, has a velocity of 227 m/s and impacts against a rigid wall at time $t = 0$ s (see Fig. 36). A von Mises hyperelastic-plastic material with isotropic hardening is chosen to simulate the material. The material parameters are Young's modulus $E = 117$ GPa, density $\rho_0 = 8.930 \times 10^3$ kg/m^3, Poisson's ratio $\nu = 0.35$, yield stress, $\bar{\tau}_y^0 = 0.4$ GPa and hardening modulus $H = 0.1$ GPa. Fig. **??** shows the comparison of plastic strain distribution at a particular time using three different methodologies, namely, constrained-TOUCH, penalisation-TOUCH and Hyperelastic-GLACE. As can be observed, results using the constrained-TOUCH and penalisation-TOUCH approaches are very similar (see Fig. **??**a-b). On the contrary, the result displayed by using the Hyperelastic-GLACE approach is more diffusive, as can be noticed from the deformed shape of the cross section in contact with the rigid wall (see Fig. **??**c). A sequence of pressure snapshots for the bar is also shown in Fig. 37, where similar conclusions can be drawn.

For comparison purposes, the time evolution of the current coordinate of the mid-edge ($\boldsymbol{X} = [0.003, 0, 0]^T$) is monitored and compared in Fig. 38 for the three different approaches, namely constrained-TOUCH, penalised-TOUCH ($\xi_{\boldsymbol{F}} = 0.15$) and Hyperelastic-GLACE. It can be seen that all methodologies produce similar locking-free deformation, where mesh refinement leads to a converged solution just under $7 \cdot 10^{-3}$ m. However, the Hyperelastic-GLACE scheme needs of a more refined mesh $20 \times 100 \times 20$ in order to converge to the same results displayed by the TOUCH methodologies for a coarser mesh of $12 \times 60 \times 12$.

10. CONCLUDING REMARKS

This paper introduces a new mixed conservation law computational framework for the numerical simulation of large strain solid dynamics. The formulation bridges the gap between CFD and large strain solid dynamics and it has been implemented, from scratch, within the open source platform OpenFOAM. Following the works of [2, 1], a mixed formulation written in the form of a system of first order hyperbolic equations is employed. The linear momentum $\boldsymbol{p}$, the deformation gradient $\boldsymbol{F}$, the total energy E and the geometry $\boldsymbol{x}$ are regarded as primary conservation variables. For closure of the system, two variants of isothermal constitutive laws are presented, both for neo-Hookean and hyperelastic-plastic models. A thorough study of the eigen-structure of the full system of conservation laws is presented in order to demonstrate its hyperbolicity and compute appropriate time step bounds.

From the spatial discretisation point of view, a second order monotonicity-preserving Cell Centred Finite Volume Method named TOUCH is used in conjunction with an acoustic (linearised) Riemann solver. Unfortunately, the standard Godunov-type update does not ensure the satisfaction of existing involutions (curl-free condition of the deformation gradient), thus allowing for the appearance of spurious mechanisms which lead to the breakdown of the solution. To overcome this, two alternative algorithms are presented for the update of the deformation gradient, namely constrained-TOUCH and penalisation-TOUCH. In addition, an explicit TVD-RK angular momentum preserving space-time integrator is also presented.

For comparison purposes, the Hyperelastic-GLACE nodal scheme [2, 70] is adapted to a Total Lagrangian formalism and it is also implemented in OpenFOAM. Finally, a comprehensive list of numerical examples has been presented, where both TOUCH schemes show excellent behaviour in bending dominated nearly incompressible scenarios.

The inclusion of the volume map evolution [47, 48, 49, 46] and the implementation of a Roe based Riemann solver [62] to further enhance the robustness of the scheme in the context of thermoelasticity is the next step of our work.

Acknowledgements

The first author would like to acknowledge the financial support received through "The Erasmus Mundus Joint Doctorate SEED" programme. The second, third and fourth authors gratefully acknowledge the financial support provided by the Sêr Cymru National Research Network for Advanced Engineering and Materials, United Kingdom. The third author would also like to acknowledge the financial support received through "The Leverhulme Prize" awarded by The Leverhulme Trust, United Kingdom.

A. APPENDIX

This Appendix is included to demonstrate the hyperbolicity (also called rank-one convexity [47]) of the system of conservation laws. In addition, the computation of the maximum (pressure) wave speed is necessary for the evaluation of the maximum time step of the explicit time integrator. Consider the plane wave solutions of the form

$$\boldsymbol{\mathcal{U}} = \phi(\boldsymbol{X}\cdot\boldsymbol{N} - c_\alpha t)\boldsymbol{\mathcal{R}}_\alpha = \phi(\boldsymbol{X}\cdot\boldsymbol{N} - c_\alpha t)\begin{bmatrix} \boldsymbol{p}^R_\alpha \\ \boldsymbol{F}^R_\alpha \\ E^R_\alpha \\ \boldsymbol{x}^R_\alpha \end{bmatrix}, \tag{64}$$

where c_α are the wave speeds associated with the corresponding right eigenvectors $\boldsymbol{\mathcal{R}}_\alpha$. The right eigen-system is then defined as

$$c_\alpha\boldsymbol{\mathcal{R}}_\alpha = \boldsymbol{\mathcal{A}}_{\boldsymbol{N}}\boldsymbol{\mathcal{R}}_\alpha; \qquad \boldsymbol{\mathcal{A}}_{\boldsymbol{N}} = \boldsymbol{\mathcal{A}}_I N_I; \qquad \boldsymbol{\mathcal{A}}_I = \frac{\partial\boldsymbol{\mathcal{F}}_I}{\partial\boldsymbol{\mathcal{U}}}, \tag{65}$$

where $\boldsymbol{\mathcal{F}}_I$ is the flux vector in I-th material direction, $\boldsymbol{\mathcal{A}}_I$ its corresponding flux Jacobian matrix and N_I the I-th component of the vector $\boldsymbol{N}$. Analogously, the left eigen-system is of the form

$$c_\alpha\boldsymbol{\mathcal{L}}^T_\alpha = \boldsymbol{\mathcal{L}}^T_\alpha\boldsymbol{\mathcal{A}}_{\boldsymbol{N}}, \tag{66}$$

with $\boldsymbol{\mathcal{L}}_\alpha$ defined as the set of left eigenvectors. Upon the use of (16), the flux Jacobian matrix $\boldsymbol{\mathcal{A}_N}$ of the system of conservation laws is given by

$$\boldsymbol{\mathcal{A}_N} = \begin{bmatrix} \mathbf{0}_{3\times3} & -\boldsymbol{\mathcal{C}}_N & \mathbf{0}_{3\times1} & \mathbf{0}_{3\times3} \\ -\frac{1}{\rho_0}\boldsymbol{I}_N & \mathbf{0}_{9\times9} & \mathbf{0}_{9\times1} & \mathbf{0}_{9\times3} \\ -\frac{1}{\rho_0}\boldsymbol{PN} & -\frac{1}{\rho_0}\boldsymbol{p}^T\boldsymbol{\mathcal{C}}_N & 0 & \mathbf{0}_{1\times3} \\ \mathbf{0}_{3\times3} & \mathbf{0}_{3\times9} & \mathbf{0}_{3\times1} & \mathbf{0}_{3\times3} \end{bmatrix}, \tag{67}$$

where

$$[\boldsymbol{\mathcal{C}}_N]_{ijJ} = \mathcal{C}_{iIjJ}N_I; \qquad \mathcal{C}_{iIjJ} = \frac{\partial P_{iI}}{\partial F_{jJ}}; \qquad [\boldsymbol{I}_N]_{iIj} = \delta_{ij}N_I. \tag{68}$$

Substitution of the above expression $\boldsymbol{\mathcal{A}_N}$ into (65a), and particularisation for each of the conservation variables, yields

$$c_\alpha \boldsymbol{p}_\alpha^R = -\boldsymbol{\mathcal{C}}_N : \boldsymbol{F}_\alpha^R \tag{69a}$$

$$c_\alpha \boldsymbol{F}_\alpha^R = -\frac{1}{\rho_0}\boldsymbol{p}_\alpha^R \otimes \boldsymbol{N} \tag{69b}$$

$$c_\alpha E_\alpha^R = -\frac{1}{\rho_0}\boldsymbol{p}_\alpha^R \cdot \boldsymbol{PN} - \frac{1}{\rho_0}\boldsymbol{p}^T\boldsymbol{\mathcal{C}}_N : \boldsymbol{F}_\alpha^R \tag{69c}$$

$$c_\alpha \boldsymbol{x}_\alpha^R = \mathbf{0}. \tag{69d}$$

Equation (69c) can be further reduced by substituting (69a) into (69c) as follows,

$$c_\alpha E_\alpha^R = -\frac{1}{\rho_0}\boldsymbol{p}_\alpha^R \cdot \boldsymbol{PN} + \frac{c_\alpha}{\rho_0}\left(\boldsymbol{p}\cdot\boldsymbol{p}_\alpha^R\right). \tag{70}$$

Notice that, in the case of an isothermal process, both expressions (70) and (69d) are clearly redundant as no coupling term emerges in (69a) [46]. Analogously, substitution of (69a) into (69b) results in

$$\rho_0 c_\alpha^2 \boldsymbol{p}_\alpha^R = \boldsymbol{\mathcal{C}}_{NN}\boldsymbol{p}_\alpha^R; \qquad [\boldsymbol{\mathcal{C}}_{NN}]_{ij} = [\boldsymbol{\mathcal{C}}]_{iIjJ}\, N_I N_J. \tag{71}$$

The tensor $\boldsymbol{\mathcal{C}}_{NN}$ for the constitutive model under consideration (see Section 2.5) can be shown to be

$$\begin{aligned} \boldsymbol{\mathcal{C}}_{NN} = &-\frac{2}{3}\mu J_{\boldsymbol{F}}^{-5/3}\left((\boldsymbol{H_F N})\otimes(\boldsymbol{FN}) + (\boldsymbol{FN})\otimes(\boldsymbol{H_F N})\right) \\ &+ \mu J_{\boldsymbol{F}}^{-2/3}\boldsymbol{I} + \left[\frac{5}{9}\mu J_{\boldsymbol{F}}^{-8/3}(\boldsymbol{F}:\boldsymbol{F}) + \kappa\right](\boldsymbol{H_F N})\otimes(\boldsymbol{H_F N}). \end{aligned} \tag{72}$$

Combining equations (71) and (72) and introducing the vectors $\boldsymbol{m} := \boldsymbol{H_F N}$ and $\boldsymbol{m}^* := \boldsymbol{FN}$, it yields

$$\rho_0 c_\alpha^2 \boldsymbol{p}_\alpha^R = \left[\gamma_1\left(\boldsymbol{m}\otimes\boldsymbol{m}^* + \boldsymbol{m}^*\otimes\boldsymbol{m}\right) + \gamma_2\boldsymbol{I} + \gamma_3\boldsymbol{m}\otimes\boldsymbol{m}\right]\boldsymbol{p}_\alpha^R, \tag{73}$$

where

$$\gamma_1 = -\frac{2}{3}\mu J_{\boldsymbol{F}}^{-5/3}, \tag{74a}$$

$$\gamma_2 = \mu J_{\boldsymbol{F}}^{-2/3}, \tag{74b}$$

$$\gamma_3 = \kappa + \frac{5}{9}\mu J_{\boldsymbol{F}}^{-8/3}\left(\boldsymbol{F} : \boldsymbol{F}\right). \tag{74c}$$

Although it is possible to obtain a closed form solution for the eigen-system defined above, it is sufficient to compute bounds of the wave speeds. This scenario arises when the vectors $\boldsymbol{m}$ and $\boldsymbol{m}^*$ are co-linear, which is attained when $\boldsymbol{N}$ is a principal direction. In this particular case, it is easy to prove that $\boldsymbol{m}^* = \lambda \boldsymbol{n}$ and $\boldsymbol{m} = \frac{J_{\boldsymbol{F}}}{\lambda}\boldsymbol{n}$ where λ is the stretch in the spatial direction $\boldsymbol{n}$ and the system (73) yields

$$\rho_0 c_\alpha^2 \boldsymbol{p}_\alpha^R = \left[\left(2\gamma_1\left(\frac{J_{\boldsymbol{F}}}{\lambda}\right) + \gamma_3\left(\frac{J_{\boldsymbol{F}}}{\lambda}\right)^2\right)\boldsymbol{n}\otimes\boldsymbol{n} + \gamma_2\boldsymbol{I}\right]\boldsymbol{p}_\alpha^R. \tag{75}$$

It can be seen that the system contains three pairs of non-zero eigenvalues corresponding to the volumetric and shear waves as

$$c_{1,2} = \pm c_p,\ c_p = \sqrt{\frac{\left(2\gamma_1\left(\frac{J_{\boldsymbol{F}}}{\lambda}\right) + \gamma_3\left(\frac{J_{\boldsymbol{F}}}{\lambda}\right)^2 + \gamma_2\right)}{\rho_0}}, \quad c_{3,4} = c_{5,6} = \pm c_s,\ c_s = \sqrt{\frac{\gamma_2}{\rho_0}}, \tag{76}$$

with the right eigenvectors

$$\boldsymbol{\mathcal{R}}_{1,2} = \begin{bmatrix} \boldsymbol{n} \\ \pm\frac{1}{\rho_0 c_p}\boldsymbol{n}\otimes\boldsymbol{N} \\ \pm\frac{1}{\rho_0 c_p}\boldsymbol{n}\cdot\boldsymbol{P}\boldsymbol{N} + \frac{1}{\rho_0}\boldsymbol{p}\cdot\boldsymbol{n} \\ \boldsymbol{0} \end{bmatrix}, \quad \boldsymbol{\mathcal{R}}_{3,4} = \begin{bmatrix} \boldsymbol{t}_1 \\ \pm\frac{1}{\rho_0 c_s}\boldsymbol{t}_1\otimes\boldsymbol{N} \\ \pm\frac{1}{\rho_0 c_s}\boldsymbol{t}_1\cdot\boldsymbol{P}\boldsymbol{N} + \frac{1}{\rho_0}\boldsymbol{p}\cdot\boldsymbol{t}_1 \\ \boldsymbol{0} \end{bmatrix}, \tag{77}$$

and

$$\boldsymbol{\mathcal{R}}_{5,6} = \begin{bmatrix} \boldsymbol{t}_2 \\ \pm\frac{1}{\rho_0 c_s}\boldsymbol{t}_2\otimes\boldsymbol{N} \\ \pm\frac{1}{\rho_0 c_s}\boldsymbol{t}_2\cdot\boldsymbol{P}\boldsymbol{N} + \frac{1}{\rho_0}\boldsymbol{p}\cdot\boldsymbol{t}_2 \\ \boldsymbol{0} \end{bmatrix}, \tag{78}$$

where $\boldsymbol{t}_1$ and $\boldsymbol{t}_2$ are two arbitrary tangential vectors orthogonal to $\boldsymbol{n}$. The rest of the eigenvalues are zero and have null associated velocity components. Finally, the following set of left eigenvectors can be obtained in an analogous manner using expression (66)

$$\boldsymbol{\mathcal{L}}_{1,2} = \begin{bmatrix} \boldsymbol{n} \\ \pm\frac{1}{c_p}\boldsymbol{\mathcal{C}} : (\boldsymbol{n}\otimes\boldsymbol{N}) \\ \boldsymbol{0} \\ \boldsymbol{0} \end{bmatrix}, \quad \boldsymbol{\mathcal{L}}_{3,4} = \begin{bmatrix} \boldsymbol{t}_1 \\ \pm\frac{1}{c_s}\boldsymbol{\mathcal{C}} : (\boldsymbol{t}_1\otimes\boldsymbol{N}) \\ \boldsymbol{0} \\ \boldsymbol{0} \end{bmatrix}, \quad \boldsymbol{\mathcal{L}}_{5,6} = \begin{bmatrix} \boldsymbol{t}_2 \\ \pm\frac{1}{c_s}\boldsymbol{\mathcal{C}} : (\boldsymbol{t}_2\otimes\boldsymbol{N}) \\ \boldsymbol{0} \\ \boldsymbol{0} \end{bmatrix}. \tag{79}$$

REFERENCES

1. Lee CH, Gil AJ, Bonet J. Development of a cell centred upwind finite volume algorithm for a new conservation law formulation in structural dynamics. *Computers and Structures* 2013; **118**:13–38.
2. Kluth G, Després B. Discretization of hyperelasticity on unstructured mesh with a cell-centered Lagrangian scheme. *Journal of Computational Physics* 2010; **229**(24):9092–9118.
3. Hughes TJR. *The finite element method: linear static and dynamic finite element analysis*. Dover Publications, 2000.
4. David J Benson. Computational methods in Lagrangian and Eulerian hydrocodes. *Computer Methods in Applied Mechanics and Engineering* 1992; **99**(2):235–394.
5. Payen DJ, Bathe KJ. Improved stresses for the 4-node tetrahedral element. *Computers and Structures* 2011; **89**:1265–1273.
6. Payen DJ, Bathe KJ. A stress improvement procedure. *Computers and Structures* 2012; **112-113**:311–326.
7. Hilber HM, Hughes TJR, Taylor RL. Improved numerical dissipation for time integration algorithms in structural dynamics. *Earthquake Engineering and Structural Dynamics* 1977; **5**(3):283–292.
8. Wood WL, Bossak M, Zienkiewicz OC. An alpha modification of Newmark's method. *International Journal for Numerical Methods in Engineering* 1980; **15**(10):1562–1566.
9. Chung J, Hulbert GM. A time integration algorithm for structural dynamics with improved numerical dissipation: The generalized-α method. *Journal of Applied Mechanics* Jun 1993; **60**(2):371–375.
10. Adams DD, Wood WL. Comparison of Hilber-Hughes-Taylor and Bossak 'α-methods' for the numerical integration of vibration equations. *International Journal for Numerical Methods in Engineering* 1983; **19**(5):765–771.
11. Bathe KJ. *Finite element procedures*. Prentice Hall, 1996.
12. Onishi Y, Amaya K. A locking-free selective smoothed finite element method using tetrahedral and triangular elements with adaptive mesh rezoning for large deformation problems. *International Journal for Numerical Methods in Engineering* 2014; **99**:354–371.
13. Onishi Y, Amaya K. Performance evaluation of the selective smoothed finite element methods using tetrahedral elements with deviatoric/hydrostatic split in large deformation analysis. *Theoretical and Applied Mechanics Japan* 2015; **63**:55–65.
14. Pires FMA, de Souza Neto EA, de la Cuesta Padilla JL. An assessment of the average nodal volume formulation for the analysis of nearly incompressible solids under finite strains. *Communications in Numerical Methods in Engineering* 2004; **20**:569–583.
15. Gil AJ, Ledger PD. A coupled hp-finite element scheme for the solution of two-dimensional electrostrictive materials. *International Journal for Numerical Methods in Engineering* 2012; **91**:1158–1183.
16. Jin D, Ledger PD, Gil AJ. An hp-fem framework for the simulation of electrostrictive and magnetostrictive materials. *Computers and Structures* 2014; **133**:131–148.
17. Jin D, Ledger PD, Gil AJ. hp-Finite Element solution of coupled stationary magnetohydrodynamics problems including magnetostrictive effects. *Computers and Structures* 2015; Accepted.
18. Belytschko T, Ong JS, Liu WK, Kennedy JM. Hourglass control in linear and nonlinear problems. *Computer Methods in Applied Mechanics and Engineering* 1984; **43**:251–276.
19. Flanagan DP, Belytschko T. A uniform strain hexahedron and quadrilateral with orthogonal hourglass control. *International Journal for Numerical Methods in Engineering* 1981; **17**:679–706.
20. Donea J, Huerta A. *Finite element methods for flow problems*. John Wiley & Sons, 2003.
21. Bonet J, Burton A. A simple average nodal pressure tetrahedral element for incompressible and nearly incompressible dynamic explicit applications. *Communications in Numerical Methods in Engineering* 1998; **14**(5):437–449.
22. Gee MW, Dohrmann CR, Key SW, Wall WA. A uniform nodal strain tetrahedron with isochoric stabilization. *International Journal for Numerical Methods in Engineering* 2009; **78**(4):429–443.
23. Puso MA, Solberg J. A stabilized nodally integrated tetrahedral. *International Journal for Numerical Methods in Engineering* 2006; **67**(6):841–867.
24. Dohrmann C, Heinstein M, Jung J, Key S, Witkowski W. Node-based uniform strain elements for three-node triangular and four-node tetrahedral meshes. *International Journal for Numerical Methods in Engineering* 2000; **47**(9):1549–1568.
25. Bonet J, Marriott H, Hassan O. An averaged nodal deformation gradient linear tetrahedral element for large strain explicit dynamic applications. *Communications in Numerical Methods in Engineering* 2001; **17**(8):551–561.
26. Souza Neto EA, Perić D, Dutko M, Owen DRJ. Design of simple low order finite elements for large strain analysis of nearly incompressible solids. *International Journal of Solids and Structures* 1996; **33**:3277–3296.

27. Scovazzi G, Carnes B, Zeng X, Rossi S. A simple, stable, and accurate linear tetrahedral finite element for transient, nearly and fully incompressible solid dynamics: A dynamic variational multiscale approach. *International Journal for Numerical Methods in Engineering* 2015; DOI: 10.1002/nme.5138.
28. Fryer Y, Bailey C, Cross M, Lai CH. A control volume procedure for solving the elastic stress-strain equations on an unstructured mesh. *Applied Mathematical Modelling* 1991; **15**(1112):639–645.
29. Bailey C, Cross M. A finite volume procedure to solve elastic solid mechanics problems in three dimensions on an unstructured mesh. *International Journal for Numerical Methods in Engineering* 1995; **38**(10):1757–1776.
30. Slone A, Bailey C, Cross M. Dynamic solid mechanics using finite volume methods. *Applied Mathematical Modelling* 2003; **27**(2):69–87.
31. Taylor GA, Bailey C, Cross M. A vertex-based finite volume method applied to non-linear material problems in computational solid mechanics. *International Journal for Numerical Methods in Engineering* 2003; **56**(4):507–529.
32. Jasak H, Weller H. Application of the finite volume method and unstructured meshes to linear elasticity. *International Journal for Numerical Methods in Engineering* 2000; **48**(2):267–287.
33. Bijelonja I, Demirdžić I, Muzaferija S. A finite volume method for incompressible linear elasticity. *Computer Methods in Applied Mechanics and Engineering* 2006; **195**:6378–6390.
34. Cardiff P, Karač A, Ivanković A. Development of a finite volume contact solver based on the penalty method. *Computational Materials Science* 2012; **64**:283–284.
35. Cardiff P, Karač A, Ivanković A. A large strain finite volume method for orthotropic bodies with general material orientations. *Computer Methods in Applied Mechanics and Engineering* 2014; **268**:318–335.
36. Després B, Mazeran C. Lagrangian Gas Dynamics in Two Dimensions and Lagrangian systems. *Archive for Rational Mechanics and Analysis* 2005; **178**(3):327–372.
37. Pierre-Henri Maire, Rémi Abgrall, Jérôme Breil, Jean Ovadia. A cell-centered Lagrangian scheme for two-dimensional compressible flow problems. *SIAM Journal on Scientific Computing* 2007; **29**(4):1781–1824.
38. Carré G, Del Pino S, Després B, Labourasse E. A cell-centered Lagrangian hydrodynamics scheme on general unstructured meshes in arbitrary dimension. *Journal of Computational Physics* 2009; **228**(14):5160–5183.
39. Pierre-Henri Maire. A high order cell-centered Lagrangian scheme for compressible fluid flows in two-dimensional cylindrical geometry. *Journal of Computational Physics* 2009; **228**:6882–6915.
40. Burton DE, Carney TC, Morgan NR, Sambasivan SK, Shashkov MJ. A Cell-Centered Lagrangian Godunov-like method for solid dynamics. *Computers and Fluids* 2013; **83**:33–47.
41. Trangenstein JA, Colella P. A higher-order Godunov method for modeling finite deformation in elastic-plastic solids. *Communications on Pure and Applied Mathematics* 1991; **44**(1):41–100.
42. Trangenstein JA. A second-order Godunov algorithm for two-dimensional solid mechanics. *Computational mechanics* 1994; **13**(5):343–359.
43. Aguirre M, Gil AJ, Bonet J, Carreño AA. A vertex centred finite volume Jameson–Schmidt–Turkel (JST) algorithm for a mixed conservation formulation in solid dynamics. *Journal of Computational Physics* 2014; **259**:672–699.
44. Karim IA, Lee CH, Gil AJ, Bonet J. A two-step Taylor-Galerkin formulation for fast dynamics. *Engineering Computations* 2014; **31**(3):366–387.
45. Lee CH, Gil AJ, Bonet J. Development of a stabilised Petrov–Galerkin formulation for conservation laws in Lagrangian fast solid dynamics. *Computer Methods in Applied Mechanics and Engineering* 2014; **268**:40–64.
46. Aguirre M, Gil AJ, Bonet J, Lee CH. An upwind vertex centred Finite Volume solver for Lagrangian solid dynamics. *Journal of Computational Physics* 2015; **300**:387–422.
47. Gil AJ, Lee CH, Bonet J, Aguirre M. A stabilised Petrov–Galerkin formulation for linear tetrahedral elements in compressible, nearly incompressible and truly incompressible fast dynamics. *Computer Methods in Applied Mechanics and Engineering* 2014; **276**:659–690.
48. Bonet J, Gil AJ, Lee CH, Aguirre M, Ortigosa R. A first order hyperbolic framework for large strain computational solid dynamics. Part I: Total Lagrangian isothermal elasticity. *Computer Methods in Applied Mechanics and Engineering* 2015; **283**:689–732.
49. Gil AJ, Lee CH, Bonet J, Ortigosa R. A first order hyperbolic framework for large strain computational solid dynamics. Part II: Total Lagrangian compressible, nearly incompressible and truly incompressible elasticity. *Computer Methods in Applied Mechanics and Engineering* 2016; **300**:146–181.
50. Torrilhon M. Locally divergence-preserving upwind finite volume schemes for magnetohydrodynamic equations. *SIAM Journal on Scientific Computing* 2005; **26**(4):1166–1191.
51. Jeltsch R, Torrilhon M. On curl-preserving finite volume discretizations for shallow water equations. *BIT Numerical Mathematics* 2006; **46**(1):35–53.
52. Dedner A, Kemm F, Kröner D, Munz CD, Schnitzer T, Wesenberg M. Hyperbolic divergence cleaning for the MHD equations. *Journal of Computational Physics* 2002; **175**(2):645–673.

53. Tóth G. The $\nabla \cdot B = 0$ constraint in shock-capturing magnetohydrodynamics codes. *Journal of Computational Physics* 2000; **161**(2):605–652.
54. Bonet J, Gil AJ, Ortigosa R. A computational framework for polyconvex large strain elasticity. *Computer Methods in Applied Mechanics and Engineering* 2015; **283**:1061–1094.
55. Nguyen NC, Peraire J. Hybridizable Discontinuous Galerkin methods for partial differential equations in continuum mechanics. *Journal of Computational Physics* 2012; **231**:5955–5988.
56. Gil AJ, Arranz Carreño A, Bonet J, Hassan O. The immersed structural potential method for haemodynamic applications. *Journal of Computational Physics* 2010; **229**(22):8613–8641.
57. Gil AJ, , Arranz Carreño A, Bonet J, Hassan O. An enhanced Immersed Structural Potential Method for fluid–structure interaction. *Journal of Computational Physics* 2013; **250**:178–205.
58. Thomas P, Lombard C. Geometric conservation law and its application to flow computations on moving grids. *The American Institute of Aeronautics and Astronautics (AIAA)* 1979; **17**(10):1030–1037.
59. Persson P, Bonet J, Peraire J. Discontinuous Galerkin solution of the Navier–Stokes equations on deformable domains. *Computer Methods in Applied Mechanics and Engineering* 2009; **198**(17):1585–1595.
60. Gil AJ, Bonet J, Silla J, Hassan O. A discrete geometric conservation law (DGCL) for a cell vertex finite-volume algorithm on moving domains. *International Journal for Numerical Methods in Biomedical Engineering* 2010; **26**(6):770–779.
61. Sevilla R, Gil AJ, Weberstadt M. A high-order stabilised finite element formulation for the Euler equations on deformable domains. *Computers and Structures* 2015; Under review.
62. Toro EF. *Riemann solvers and numerical methods for fluid dynamics: A practical introduction*. Third edn., Springer-Verlag, 2009.
63. Marsden JE, Hughes TJR. *Mathematical foundations of elasticity*. Dover Publications, 1994.
64. Bonet J, Wood RD. *Nonlinear continuum mechanics for finite element analysis*. Second edn., Cambridge University Press, 2008.
65. Bonet J, Gil AJ, Ortigosa R. On a tensor cross product based formulation of large strain solid mechanics. *International Journal of Solids and Structures* 2016; Doi: 10.1016/j.ijsolstr.2015.12.030.
66. Bonet J, Kulasegaram S. Correction and stabilization of smooth particle hydrodynamics methods with applications in metal forming simulations. *International Journal of Numerical Methods in Engineering* 2000; **47**:1189–1124.
67. LeVeque RJ. *Finite volume methods for hyperbolic problems*, vol. 31. Cambridge University Press, 2002.
68. Hirsch C. *Numerical computation of internal and external flows. Volume I: The fundamentals of computational fluid dynamics*. Second edn., Elsevier, 2007.
69. Barth TJ, Jespersen DC. The design and application of upwind schemes on unstructured meshes. *AIAA* 1989; **89-0366**.
70. Després B, Labourasse E. Angular Momentum preserving cell-centered Lagrangian and Eulerian schemes on arbitrary grids. *Journal of Computational Physics* 2015; **290**:28–54.
71. Pierre-Henri Maire, Abgrall R, Breil J, Loubère R, Rebourcet B. A nominally second-order cell-centered Lagrangian scheme for simulating elastic–plastic flows on two-dimensional unstructured grids. *Journal of Computational Physics* 2013; **235**:626–665.
72. Hubbard M. Multidimensional slope limiters for MUSCL-type finite volume schemes on unstructured grids. *Journal of Computational Physics* 1999; **155**(1):54–74.
73. Blazek J. *Computational Fluid Dynamics: Principles and applications*. Elsevier, 2005.
74. Engquist B, Osher S. One-sided difference approximations for nonlinear conservation laws. *Mathematics of Computation* 1981; **36**(154):321–351.
75. Courant R, Friedrichs K, Lewy H. On the partial difference equations of mathematical physics. *Mathematische Annalem* 1928; **100**:32–74.
76. Dafermos CM. *Quasilinear hyperbolic systems with involutions*. Springer, 1989.
77. Timoshenko SP, Goodier JN. *Theory of elasticity*. McGraw-Hill, 1970.
78. Brackbill JU, Barnes D. The effect of nonzero $\nabla \cdot B = 0$ on the numerical solution of the magnetohydrodynamic equations. *Journal of Computational Physics* 1980; **35**(3):426–430.
79. Simo J, Tarnow N. The discrete energy-momentum method. Conserving algorithms for nonlinear elastodynamics. *Zeitschrift für angewandte Mathematik und Physik ZAMP* 1992; **43**(5):757–792.
80. Meng X, Laursen T. Energy consistent algorithms for dynamic finite deformation plasticity. *Computer Methods in Applied Mechanics and Engineering* 2002; **191**(15):1639–1675.
81. Noels L, Stainier L, Ponthot JP. An energy–momentum conserving algorithm for non-linear hypoelastic constitutive models. *International Journal for Numerical Methods in Engineering* 2004; **59**(1):83–114.
82. Dong S. BDF-like methods for nonlinear dynamic analysis. *Journal of Computational Physics* 2010; **229**(8):3019–3045.

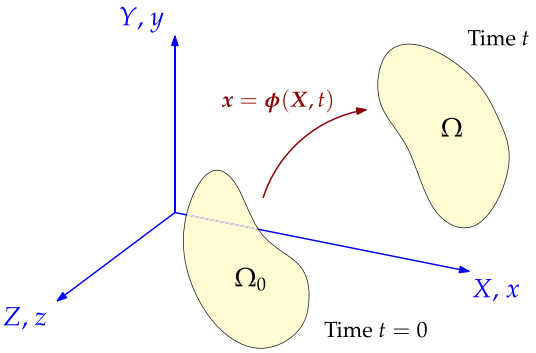

Figure 1. Motion of a continuum domain

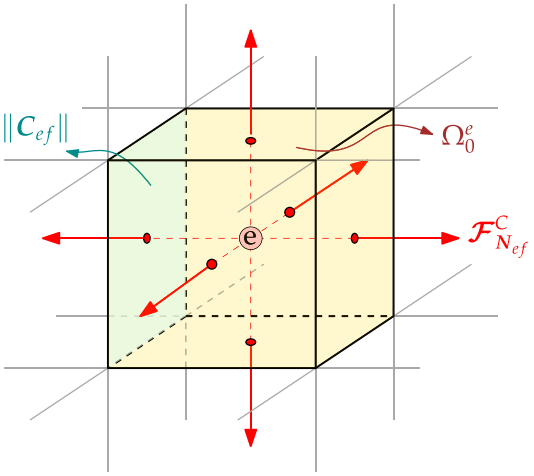

Figure 2. Standard cell centred Finite Volume Method

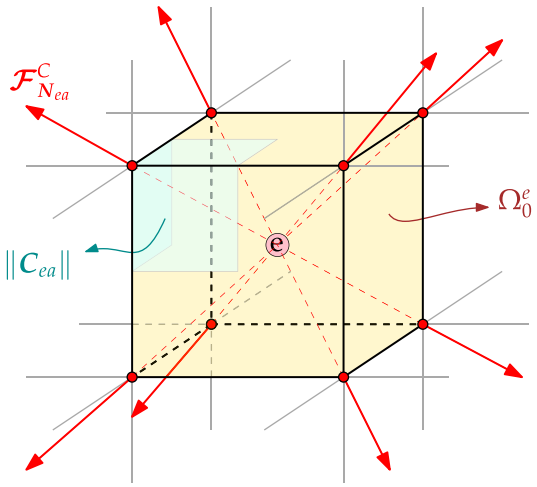

Figure 3. Cell centred nodal framework

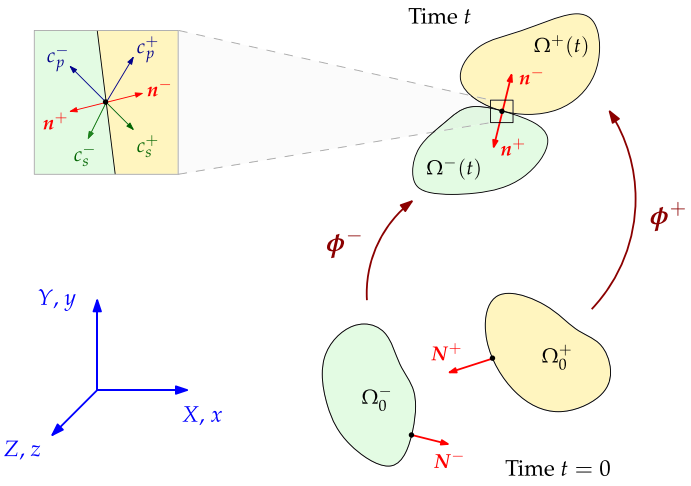

Figure 4. Contact mechanics

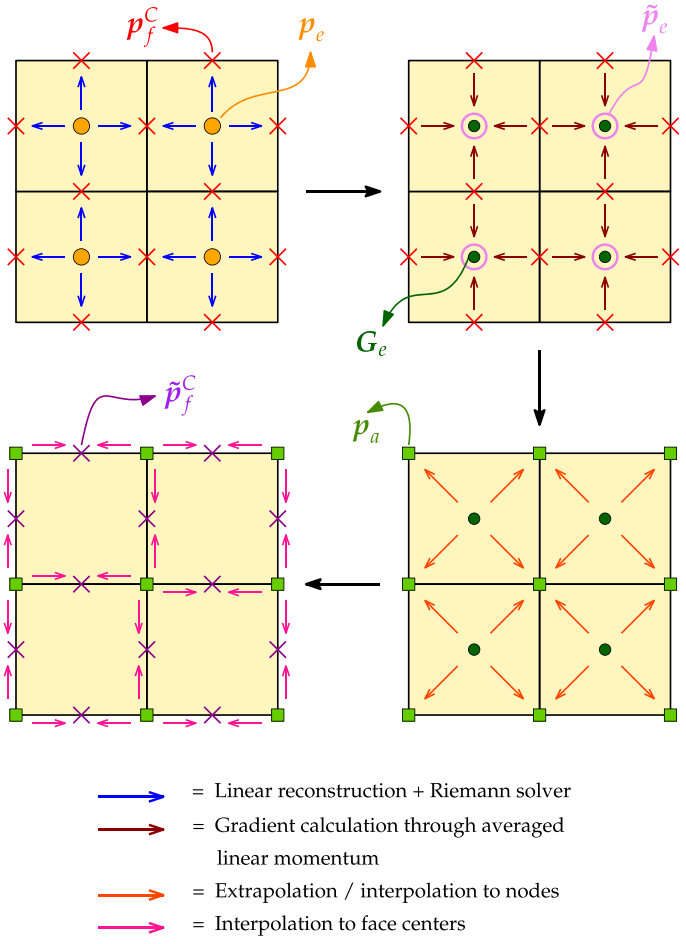

Figure 5. Involutions: Curl-free Finite Volume Method

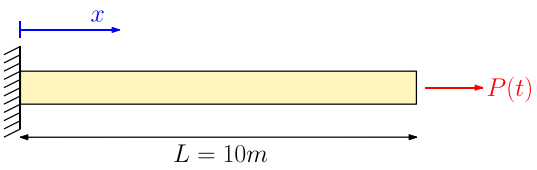

Figure 6. Elastic cable configuration

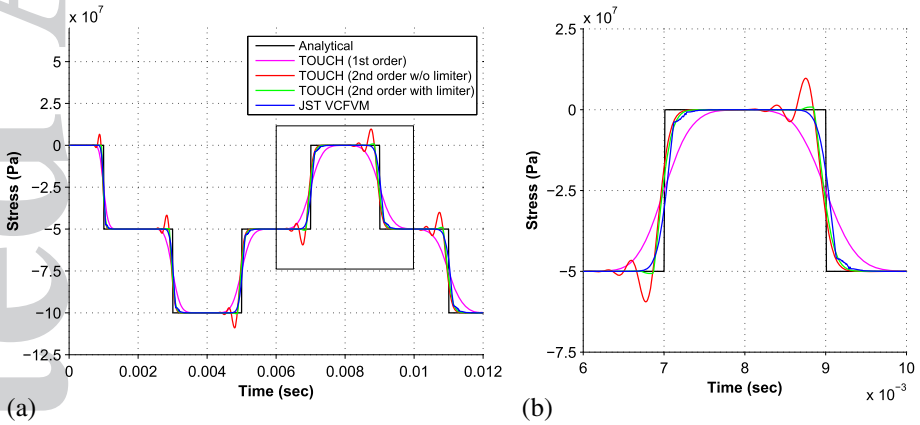

Figure 7. Elastic cable with step loading: Stress evolution at mid-bar with a shock load $P(L,t) = -5 \times 10^7$ Pa using the constrained-TOUCH scheme. Results obtained using a linear elastic constitutive model with density $\rho_0 = 8000$ kg/m^3, Young's modulus $E = 200$ GPa, Poisson's ratio $\nu = 0$, $\alpha_{\text{CFL}} = 0.5$ and $\Delta t = 1 \times 10^{-5}$ s. Discretisation of $100 \times 1 \times 1$ hexahedral elements.

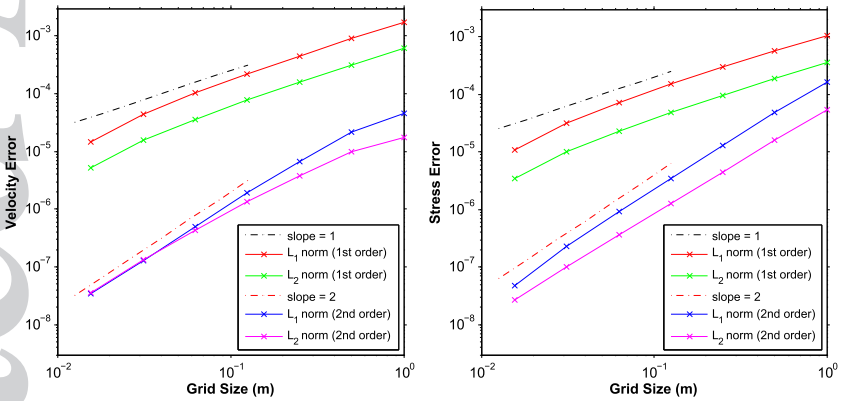

(a) Velocities (b) Stresses

Figure 8. Elastic cable with sinusoidal loading: L_1 and L_2 norm convergence of (a) Velocities and (b) Stresses at a particular time $t = 34.4757$ s using the constrained-TOUCH scheme. Results obtained using a linear elastic model with $P(L,t) = 0.001\,[\sin(\pi t/20 - \pi/2) + 1]$ Pa , density $\rho_0 = 1$ kg/m^3, Young's modulus $E = 1$ Pa, Poisson's ratio $\nu = 0.3$ and $\alpha_{\text{CFL}} = 0.5$.

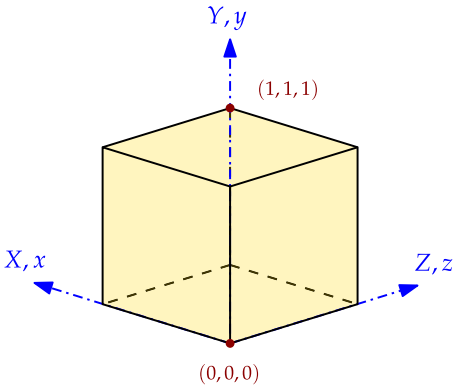

Figure 9. Low dispersion cube configuration

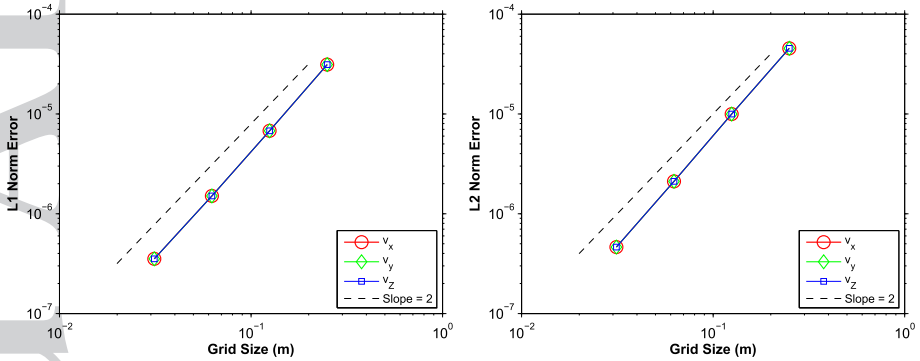

(a) Velocities

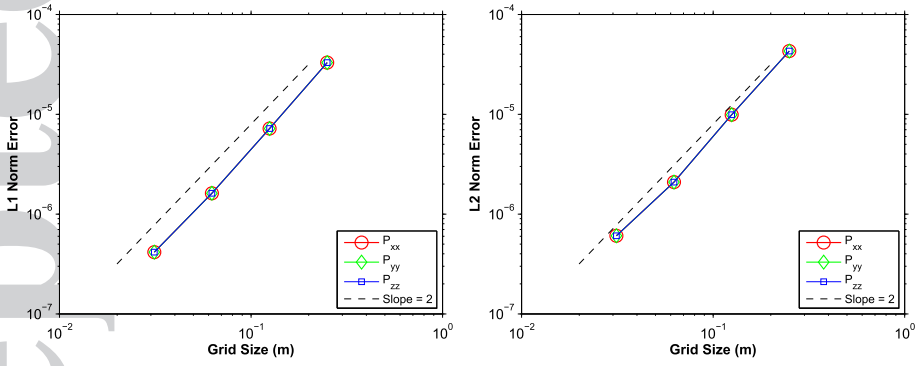

(b) Stresses

Figure 10. Low dispersion cube: L_1 and L_2 norm convergence of components of (a) Velocities; and (b) Stresses at a particular time $t = 0.004$ s. Results obtained using a linear elastic material with $A = B = C = 1$ and $U_0 = 5 \times 10^{-4}$ m using the constrain-based TOUCH. The material properties used are density $\rho_0 = 1100$ kg/m^3, Young's modulus $E = 17$ MPa, Poisson's ratio $\nu = 0.3$ and $\alpha_{\text{CFL}} = 0.3$.

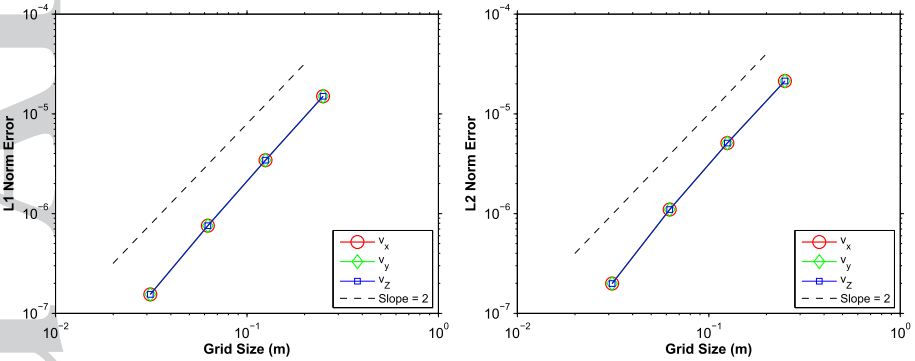

(a) Velocities

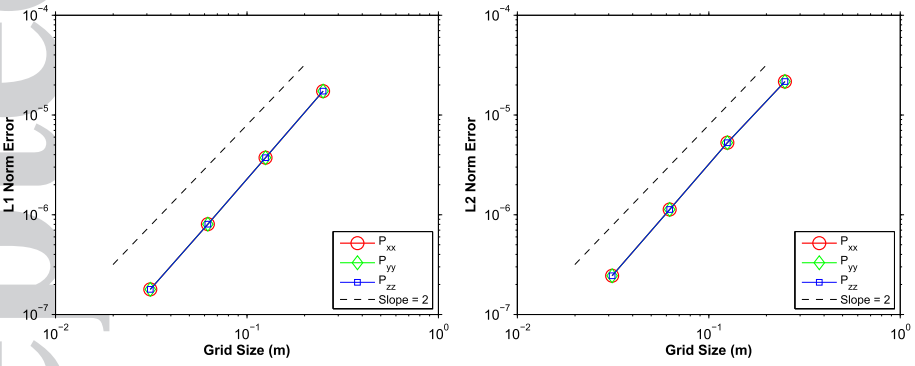

(b) Stresses

Figure 11. Low dispersion cube: L_1 and L_2 norm convergence of components of (a) Velocities; and (b) Stresses at a particular time $t = 0.004$ s. Results obtained using a linear elastic material with $A = B = C = 1$ and $U_0 = 5 \times 10^{-4}$ m using the penalisation-based TOUCH. The material properties used are density $\rho_0 = 1100$ kg/m^3, Young's modulus $E = 17$ MPa, Poisson's ratio $\nu = 0.3$ and $\alpha_{\text{CFL}} = 0.3$.

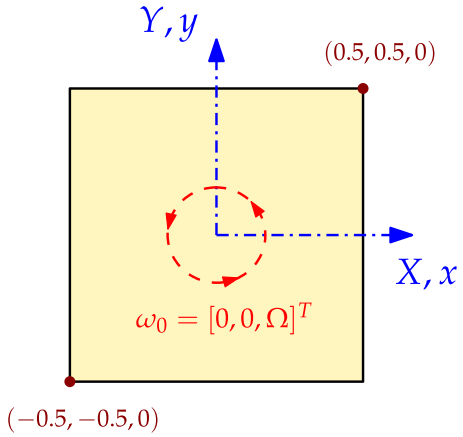

Figure 12. Low dispersion cube: L^2 norm convergence of components of (a) Velocities; and (b) Stresses at a particular time $t = 0.004$ s. Results obtained using a linear elastic material with $A = B = C = 1$ and $U_0 = 5 \times 10^{-4}$ m using the B-bar hexahedral method. The material properties used are density $\rho_0 = 1100$ kg/m^3, Young's modulus $E = 17$ MPa and Poisson's ratio $\nu = 0.3$.

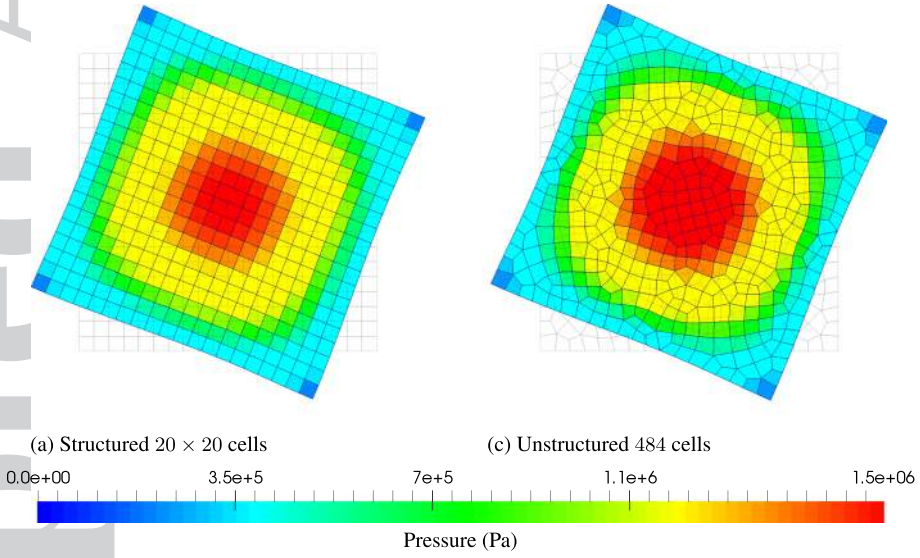

Figure 13. Spinning plate configuration

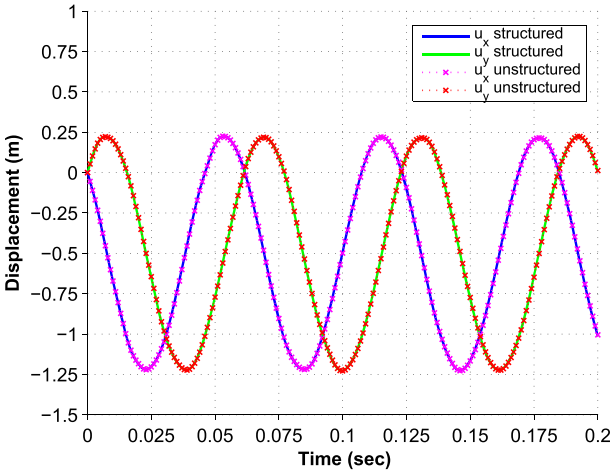

Figure 14. Spinning plate: Mesh comparison of deformed shapes plotted along with pressure distribution at $t = 0.15$ s for two different mesh types: (a) Structured mesh (20×20 cells) and (b) Unstructured mesh (484 cells). Results are obtained using the constrained-TOUCH scheme with an initial angular velocity field $\boldsymbol{\omega}_0 = [0, 0, 105]^T$ rad/s. A neo-Hookean material is used with density $\rho_0 = 1100$ kg/m^3, Young's modulus $E = 17$ MPa, Poisson's ratio $\nu = 0.45$ and $\alpha_{\text{CFL}} = 0.3$.

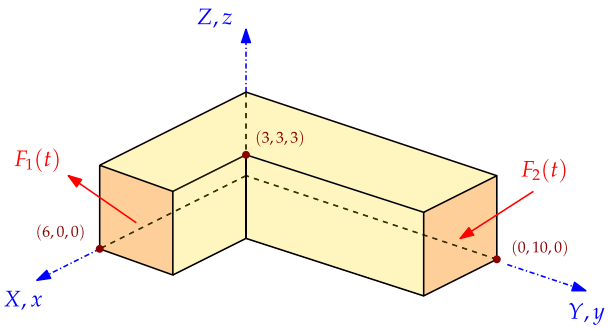

Figure 15. Spinning plate: Time evolution of x and y displacements (u_x, u_y) of the point $X = [0.5, 0.5, 0]^T$ using structured (20×20 cells) and unstructured (484 cells) meshes. Results are obtained using the constrained-TOUCH scheme with an initial angular velocity field $\boldsymbol{\omega}_0 = [0, 0, 105]^T$ rad/s. A neo-Hookean material is used with density $\rho_0 = 1100$ kg/m^3, Young's modulus $E = 17$ MPa, Poisson's ratio $\nu = 0.45$ and $\alpha_{\text{CFL}} = 0.3$.

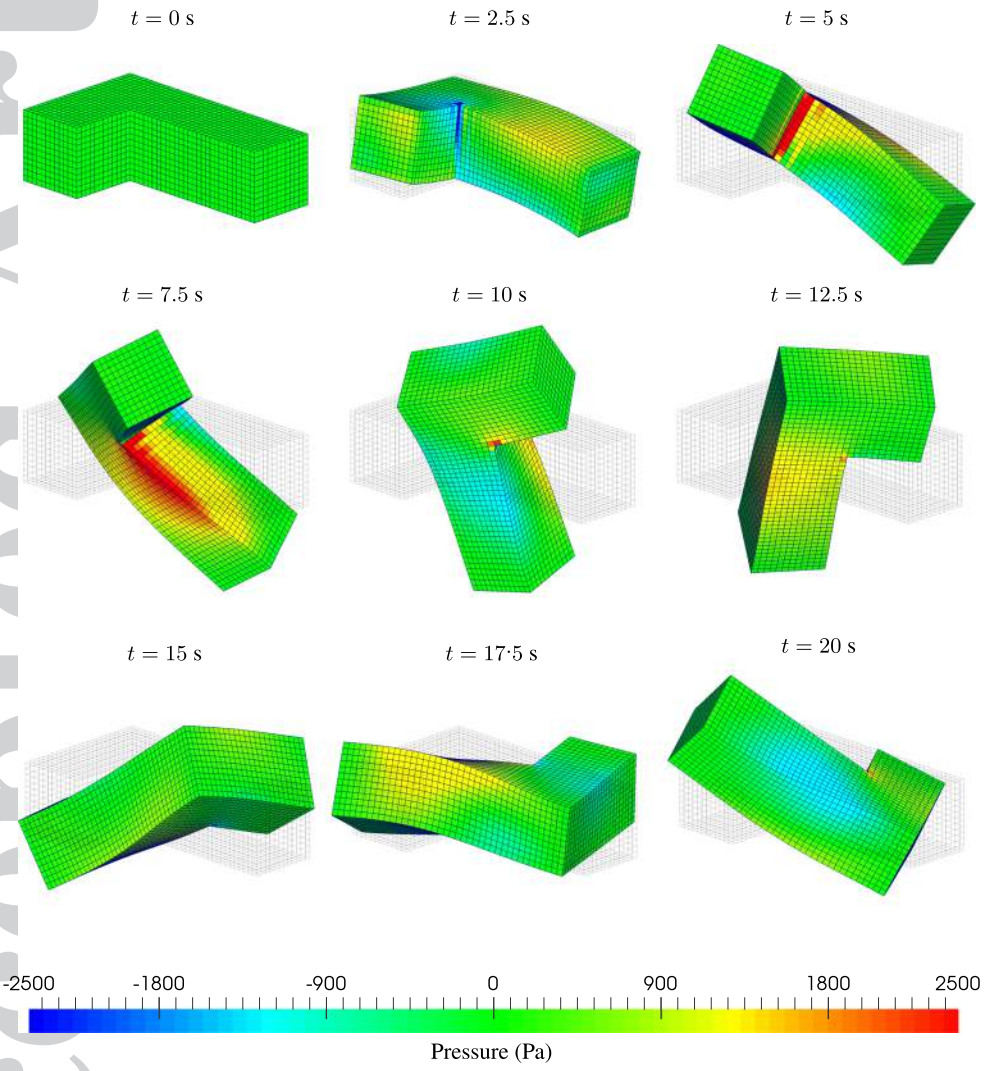

Figure 16. L-shaped block configuration

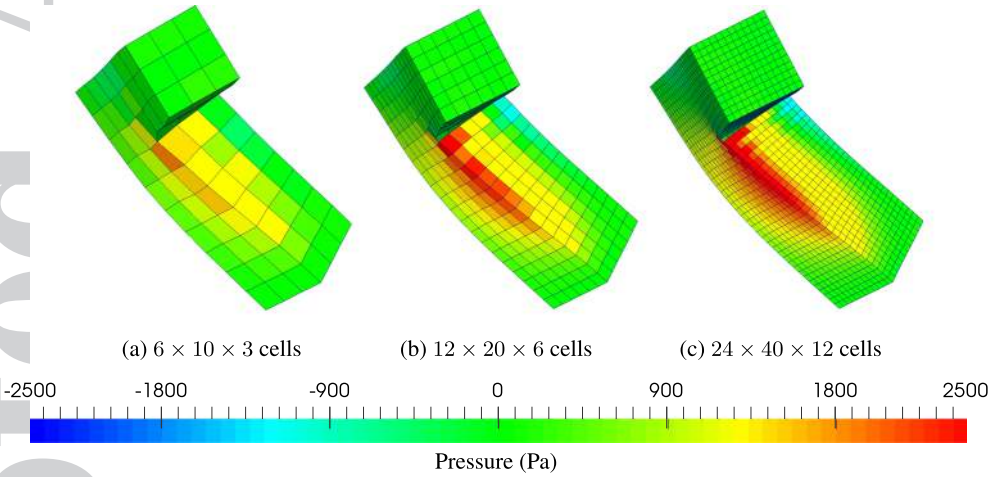

Figure 17. L-shaped block: Time evolution of the deformation plotted with pressure distribution using the constrained-TOUCH scheme. Results obtained with impulse boundary conditions on two of the sides and a discretisation of $24 \times 40 \times 12$ hexahedral elements. A neo-Hookean material is used with density $\rho_0 = 1000$ kg/m^3, Young's modulus $E = 50.05$ kPa, Poisson's ratio $\nu = 0.3$, $\alpha_{\text{CFL}} = 0.3$ and $\Delta t \approx 0.008$ s.

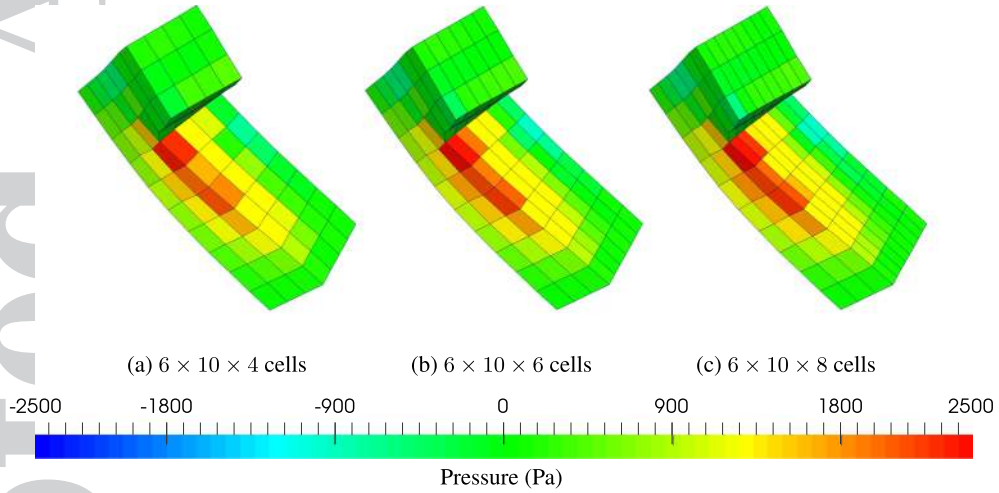

Figure 18. L-shaped block: Mesh refinement of deformed shapes plotted along with pressure contour for structured cube elements at $t = 7.5$ s for three different mesh sizes: (a) $h = 1$ m; (b) $h = 1/2$ m; and (c) $h = 1/4$ m. Results are obtained using the constrained-TOUCH scheme with the impulse boundary conditions applied on two of its sides. A neo-Hookean material is used with density $\rho_0 = 1000$ kg/m^3, Young's modulus $E = 50.05$ kPa, Poisson's ratio $\nu = 0.3$ and $\alpha_{\text{CFL}} = 0.3$.

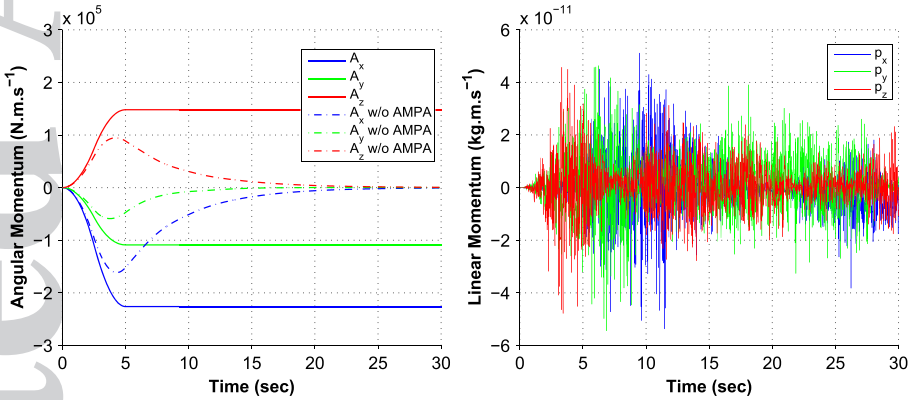

(a) Angular momentum (b) Linear momentum

Figure 19. L-shaped block: Mesh refinement along the z axis of the deformed shapes with pressure distribution for structured cuboid elements with various aspect ratios r: (a) $r = 4/3$; (b) $r = 2$; and (c) $r = 8/3$. Results are obtained at time $t = 7.5$ s using the constrained-TOUCH scheme with the impulse boundary conditions applied on two of its sides. A neo-Hookean material is used with density $\rho_0 = 1000$ kg/m^3, Young's modulus $E = 50.05$ kPa, Poisson's ratio $\nu = 0.3$ and $\alpha_{\text{CFL}} = 0.3$.

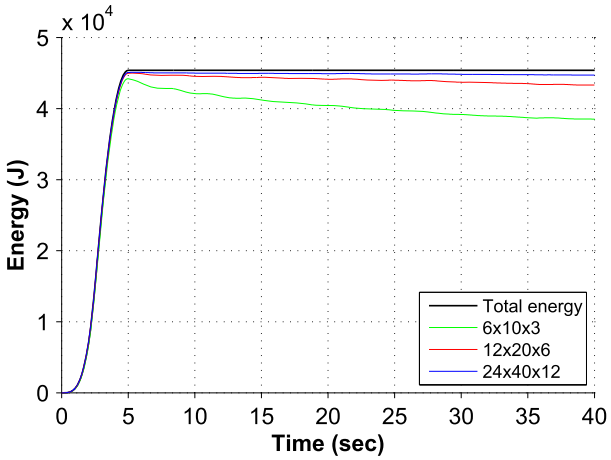

Figure 20. L-shaped block: Evolution of the components of (a) Angular momentum and (b) Linear momentum, with and without the consideration of the discrete Angular Momentum Projection Algorithm (AMPA). A hyperelastic neo-Hookean constitutive model is utilised. Results obtained using the constrained-TOUCH scheme with a discretisation of $12 \times 20 \times 6$ hexahedral elements by imposing impulse boundary conditions on two of its sides. The material properties used are density $\rho_0 = 1000$ kg/m^3, Young's modulus $E = 50.05$ kPa, Poisson's ratio $\nu = 0.3$, $\alpha_{\text{CFL}} = 0.3$ and $\Delta t \approx 0.017$ s.

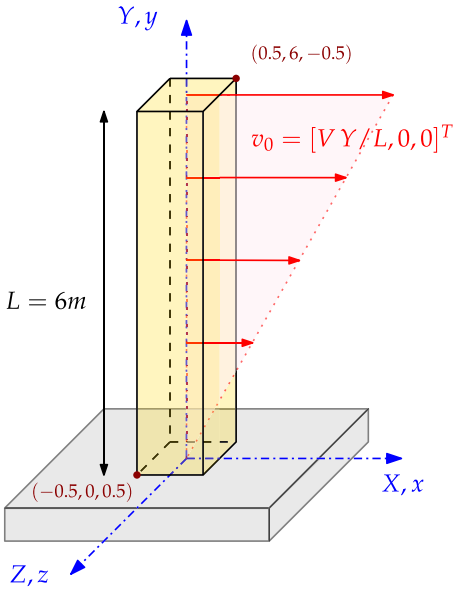

Figure 21. L-shaped block: Numerical dissipation of the constrained-TOUCH scheme discretised using three different mesh sizes. A hyperelastic neo-Hookean constitutive model is used. Results are obtained with the impulse boundary conditions applied on two of its sides and the material parameters are density $\rho_0 = 1000$ kg/m^3, Young's Modulus $E = 50.05$ kPa, Poisson's ratio $\nu = 0.3$ and $\alpha_{\text{CFL}} = 0.3$.

Figure 22. Bending column configuration

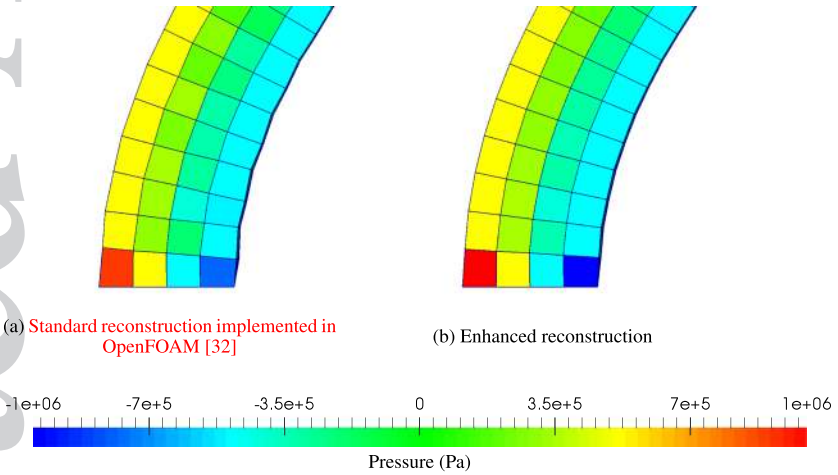

(a) Standard reconstruction implemented in OpenFOAM [32]

(b) Enhanced reconstruction

Figure 23. Bending column: Time evolution of the deformation with pressure distribution using the constrained-TOUCH scheme. Results obtained with a velocity field $v_0 = [(VY/L), 0, 0]^T$ where $V = 10$ m/s. A neo-Hookean material is used with density $\rho = 1100$ kg/m^3, Young's modulus $E = 17$ MPa, Poisson's ratio $\nu = 0.45$, $\alpha_{\text{CFL}} = 0.3$ and time step $\Delta t \approx 2.8 \times 10^{-4}$. Discretisation of $4 \times 24 \times 4$ hexahedral elements.

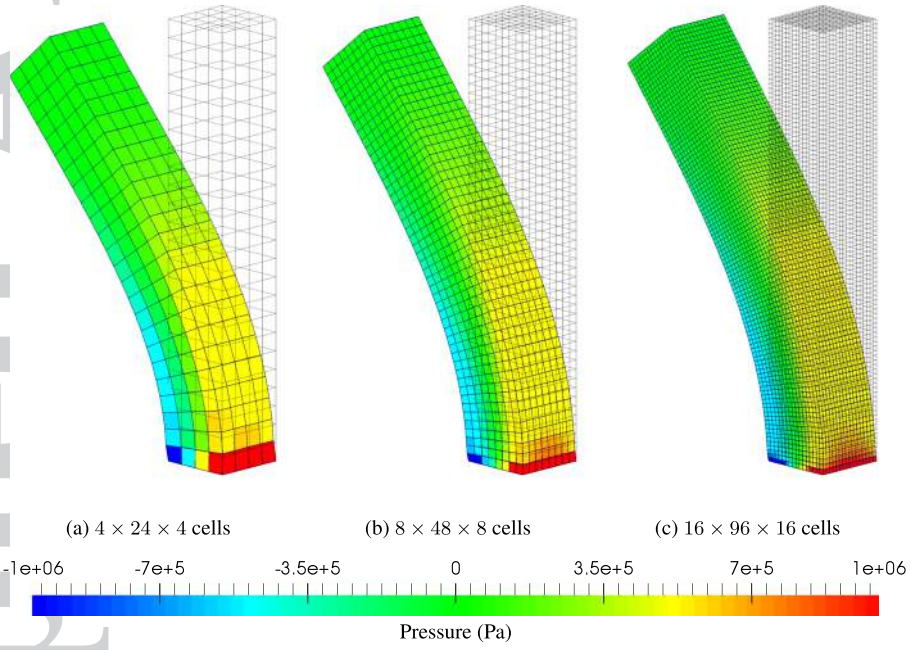

Figure 24. Bending column: Comparison of current mesh at time $t = 0.5$ s using: (a) Standard reconstruction implemented in OpenFOAM [32]; and (b) Enhanced reconstruction (with the use of additional boundary velocities). Results are obtained using the constrained-TOUCH scheme by imposing a linear variation of velocity field $v_0 = [VY/L, 0, 0]^T$ where $V = 10$ m/s. A neo-Hookean model is used where the density $\rho = 1100$ kg/m^3, Young's modulus $E = 17$ MPa, Poisson's ratio $\nu = 0.45$ and $\alpha_{\text{CFL}} = 0.3$. Discretisation of $4 \times 24 \times 4$ hexahedral elements.

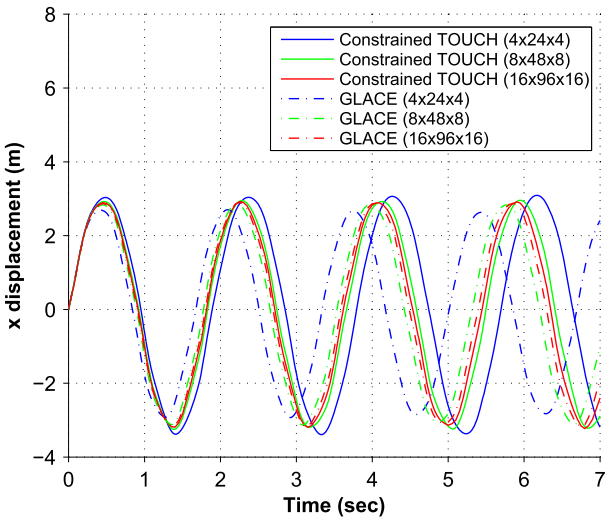

Figure 25. Bending column: Mesh refinement of deformed shapes plotted with pressure distribution at $t = 1.5$ s using three different mesh sizes: (a) $h = 1/4$ m; (b) $h = 1/8$ m; and (c) $h = 1/16$ m. Results obtained using the constrained-TOUCH scheme with a velocity field $v_0 = [(VY/L), 0, 0]^T$ where $V = 10$ m/s. A neo-Hookean material is used with density $\rho = 1100$ kg/m^3, Young's modulus $E = 17$ MPa, Poisson's ratio $\nu = 0.45$, $\alpha_{\text{CFL}} = 0.3$.

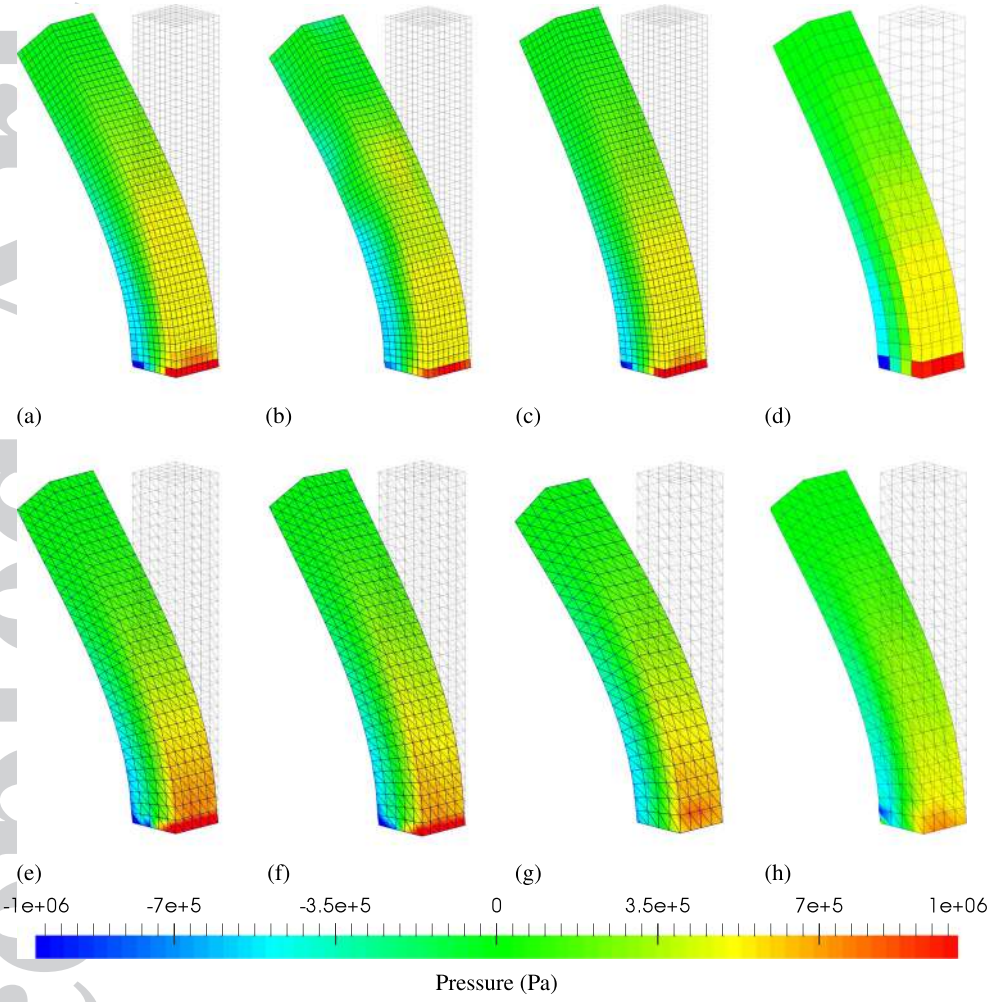

Figure 26. Bending column: Time history of x displacement at material point $\boldsymbol{X} = [0.5, 6, 0.5]^T$ simulated using the constrained-TOUCH and Hyperelastic-GLACE schemes. Results are obtained with a linear variation of velocity field $v_0 = [VY/L, 0, 0]^T$ (where $V = 10$ m/s) using three different mesh sizes, namely: $4 \times 24 \times 4$, $8 \times 48 \times 8$ and $16 \times 96 \times 16$ hexahedral elements. A neo-Hookean material is used where the material properties are density $\rho = 1100$ kg/m^3, Young's modulus $E = 17$ MPa, Poisson's ratio $\nu = 0.45$, $\alpha_{\text{CFL}} = 0.3$.

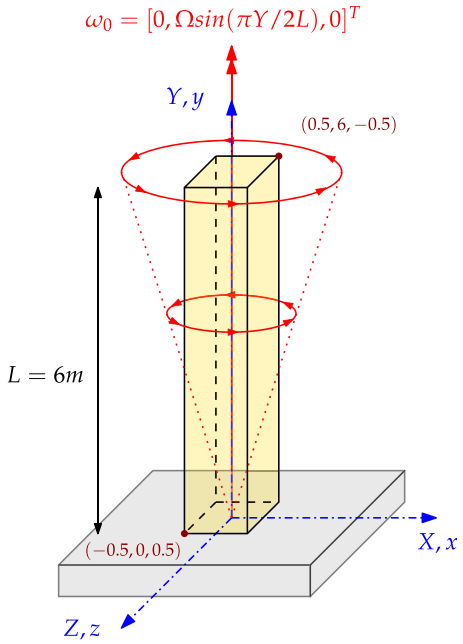

Figure 27. Bending column: Comparison of deformed shapes plotted with pressures at time $t = 1.5$ s using various numerical schemes: (a) Constrained-TOUCH; (b) Penalised-TOUCH ($\xi_{\boldsymbol{F}} = 0.1$); (c) Hyperelastic-GLACE [2]; (d) B-bar hexahedral method; (e) Upwind-VCFVM [46]; (f) JST-VCFVM [43]; (g) PG-FEM [45]; and (h) Hu-Washizu type variational principle [54]. Results are obtained with a linear variation of velocity field $v_0 = [VY/L, 0, 0]^T$ where $V = 10$ m/s and $L = 6$ m. A neo-Hookean material is used with density $\rho_0 = 1100$ kg/m^3, Young's modulus $E = 17$ MPa and Poisson's ratio $\nu = 0.45$.

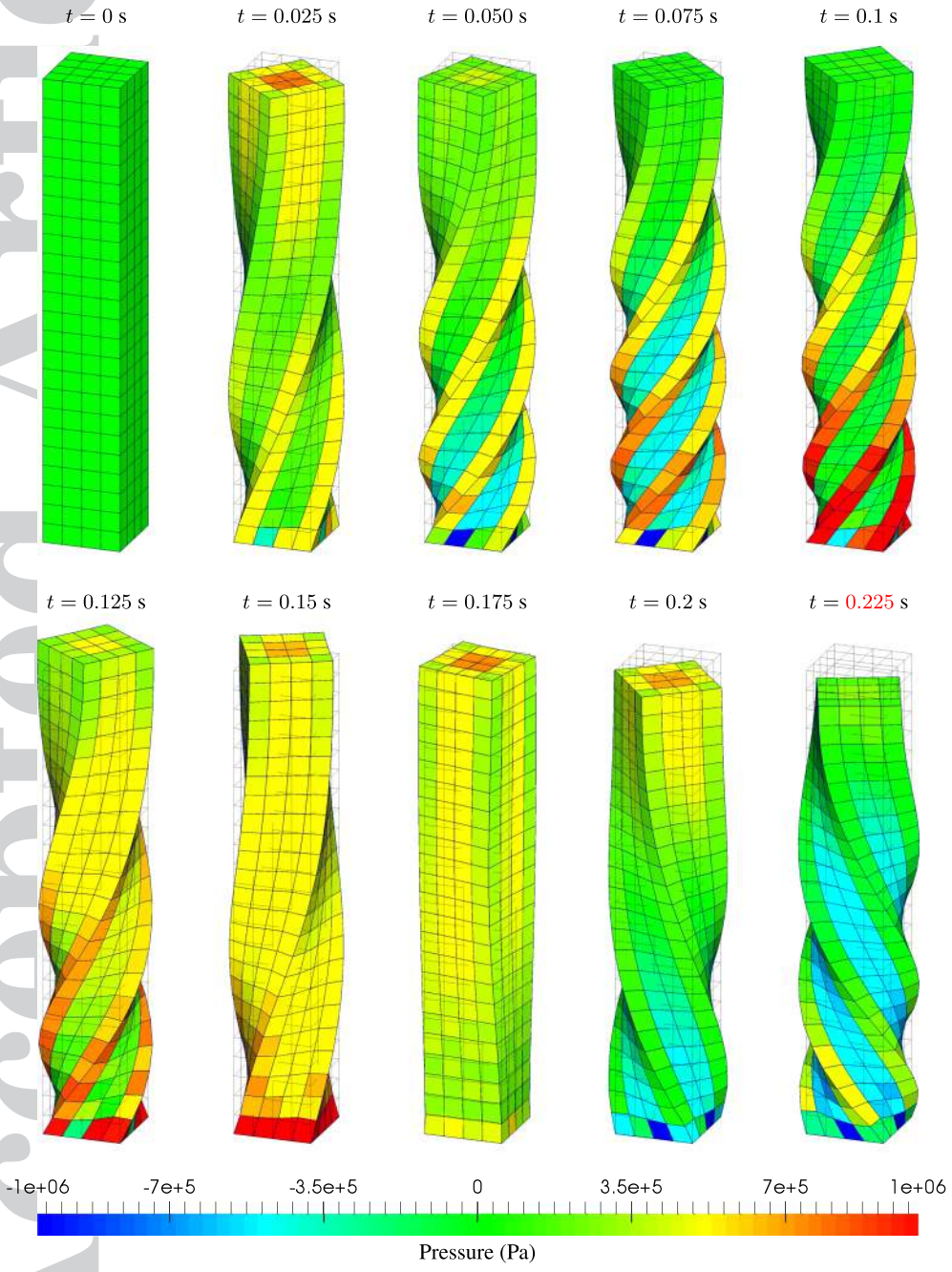

Figure 28. Twisting column configuration

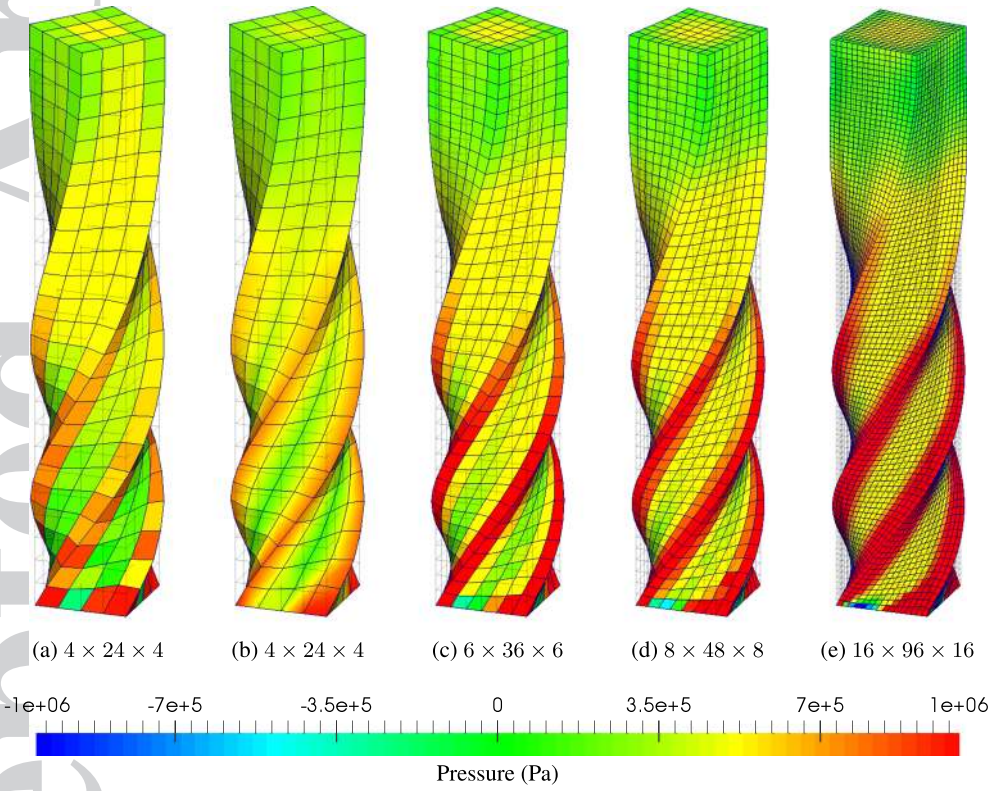

Figure 29. Twisting column: Time evolution of the deformation along with the pressure distribution using the constrained-TOUCH scheme. Results obtained with an angular velocity field $\omega_0 = [0, \Omega \sin(\pi Y/2L), 0]$ where $\Omega = 105$ rad/s and $L = 6$ m. A neo-Hookean material is used with density $\rho_0 = 1100$ kg/m^3, Young's modulus $E = 17$ MPa, Poisson's ratio $\nu = 0.45$, $\alpha_{\text{CFL}} = 0.3$ and $\Delta t \approx 2.5 \times 10^{-3}$ s. Discretisation of $4 \times 24 \times 4$ hexahedral elements.

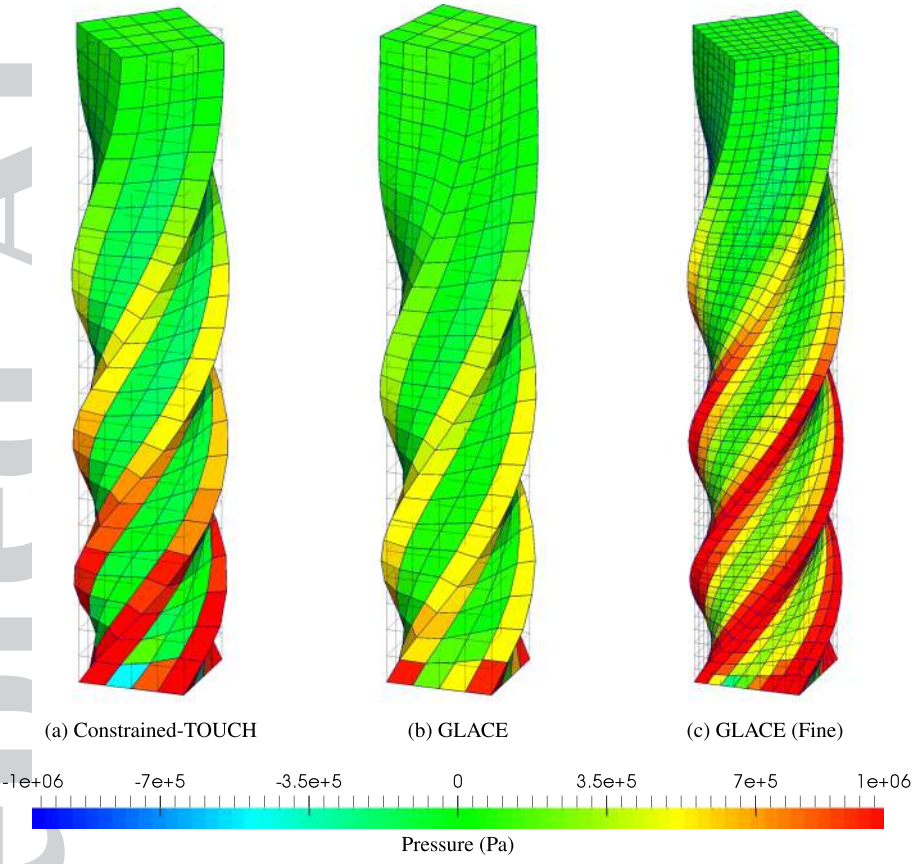

Figure 30. Twisting column: Comparison of the deformation along with the pressure distribution at time $t = 0.125$ s for various mesh sizes: (a) $4 \times 24 \times 4$ (cell values); (b) $4 \times 24 \times 4$ (node values); (c) $6 \times 36 \times 6$ (cell values); (d) $8 \times 48 \times 8$ (cell values) and (e) $16 \times 96 \times 16$ (cell values) . Results obtained using the constrained-TOUCH scheme with an angular velocity field $\omega_0 = [0, \Omega \sin(\pi Y/2L), 0]$ where $\Omega = 105$ rad/s and $L = 6$ m. A neo-Hookean material is used with density $\rho_0 = 1100$ kg/m^3, Young's modulus $E = 17$ MPa, Poisson's ratio $\nu = 0.45$ and $\alpha_{\text{CFL}} = 0.3$.

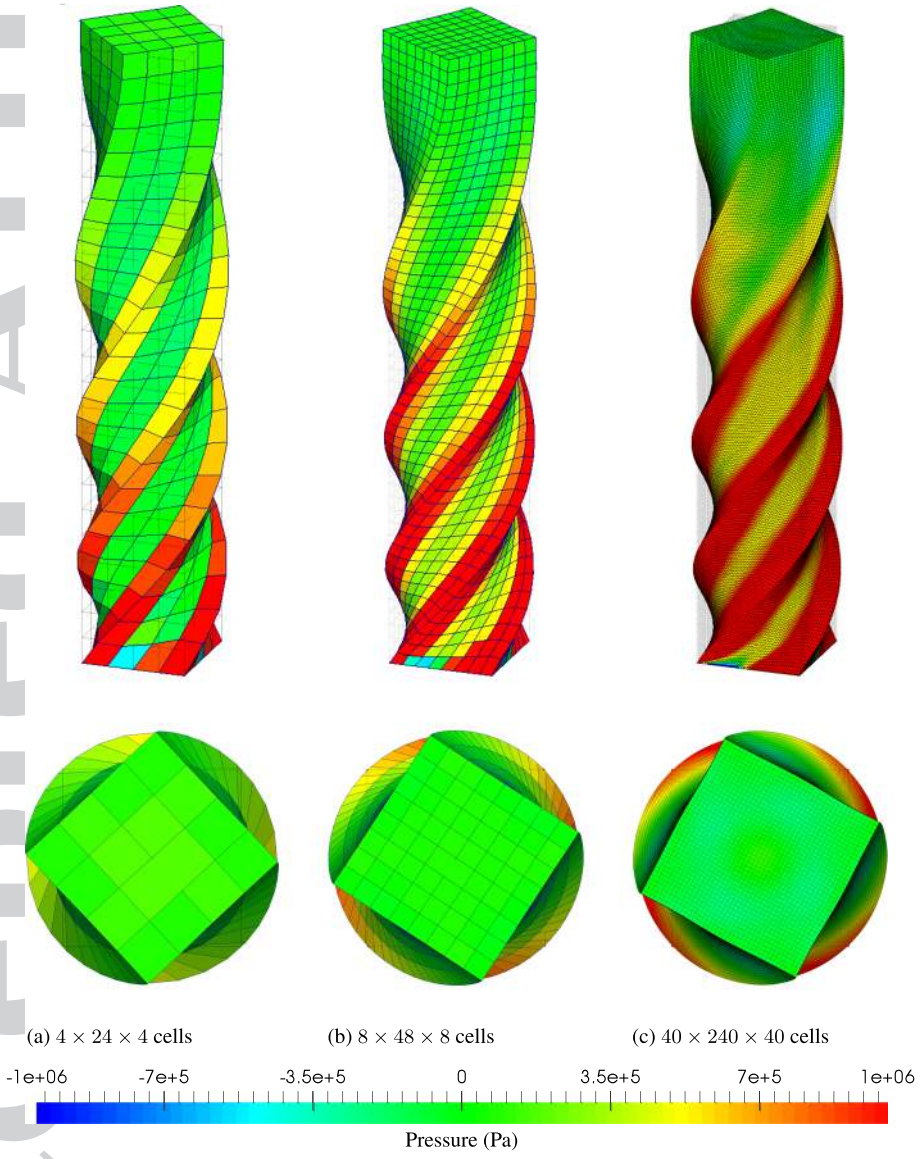

Figure 31. Twisting column: Comparison of deformed shapes plotted with pressure distribution using: (a) Constrained-TOUCH, (b) Hyperelastic-GLACE and (c) Hyperelastic-GLACE (fine mesh). Results obtained with an angular velocity field $\omega_0 = [0, \Omega \sin(\pi Y/2L), 0]$ where $\Omega = 105$ rad/s and $L = 6$ m at time $t = 0.1$ s. A neo-Hookean material is used with density $\rho_0 = 1100$ kg/m^3, Young's modulus $E = 17$ MPa, Poisson's ratio $\nu = 0.45$ and $\alpha_{\text{CFL}} = 0.3$.

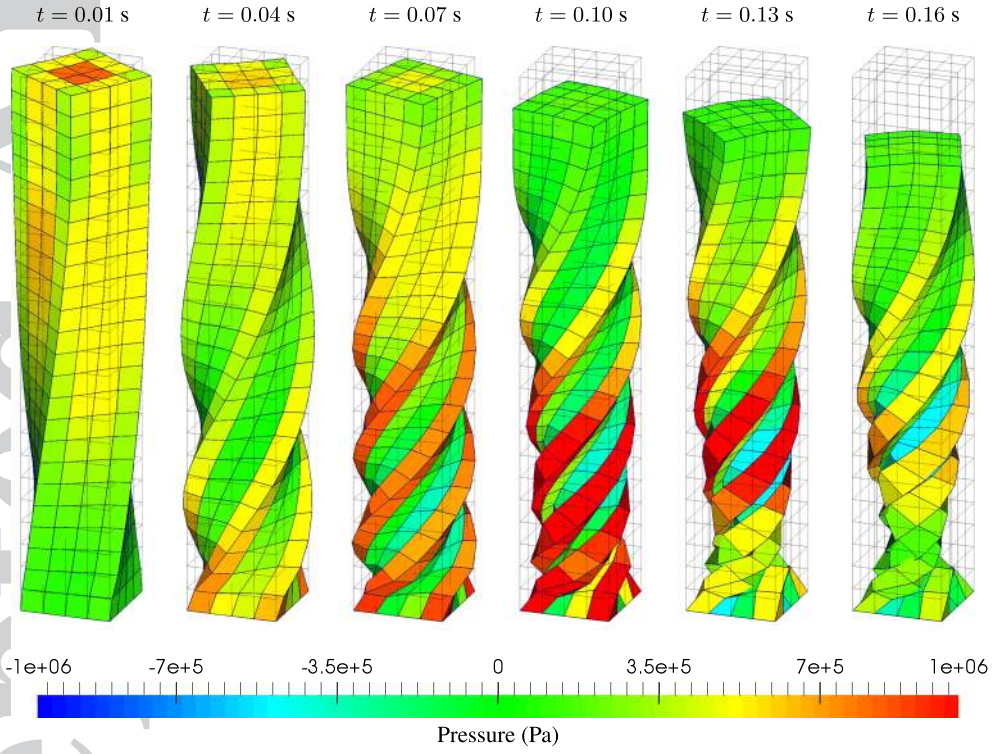

Figure 32. Twisting column: Mesh convergence of deformed shapes with pressure distribution at $t = 0.1$ s using three different mesh sizes: (a) $h = 1/4$ m, (b) $h = 1/8$ m and (c) $h = 1/40$ m. Results obtained using the constrained-TOUCH scheme with an angular velocity field $\omega_0 = [0, \Omega \sin(\pi Y/2L), 0]$, where $\Omega = 105$ rad/s and $L = 6$ m. A neo-Hookean material is used with density $\rho_0 = 1100$ kg/m^3, Young's modulus $E = 17$ MPa, Poisson's ratio $\nu = 0.45$ and $\alpha_{\text{CFL}} = 0.3$.

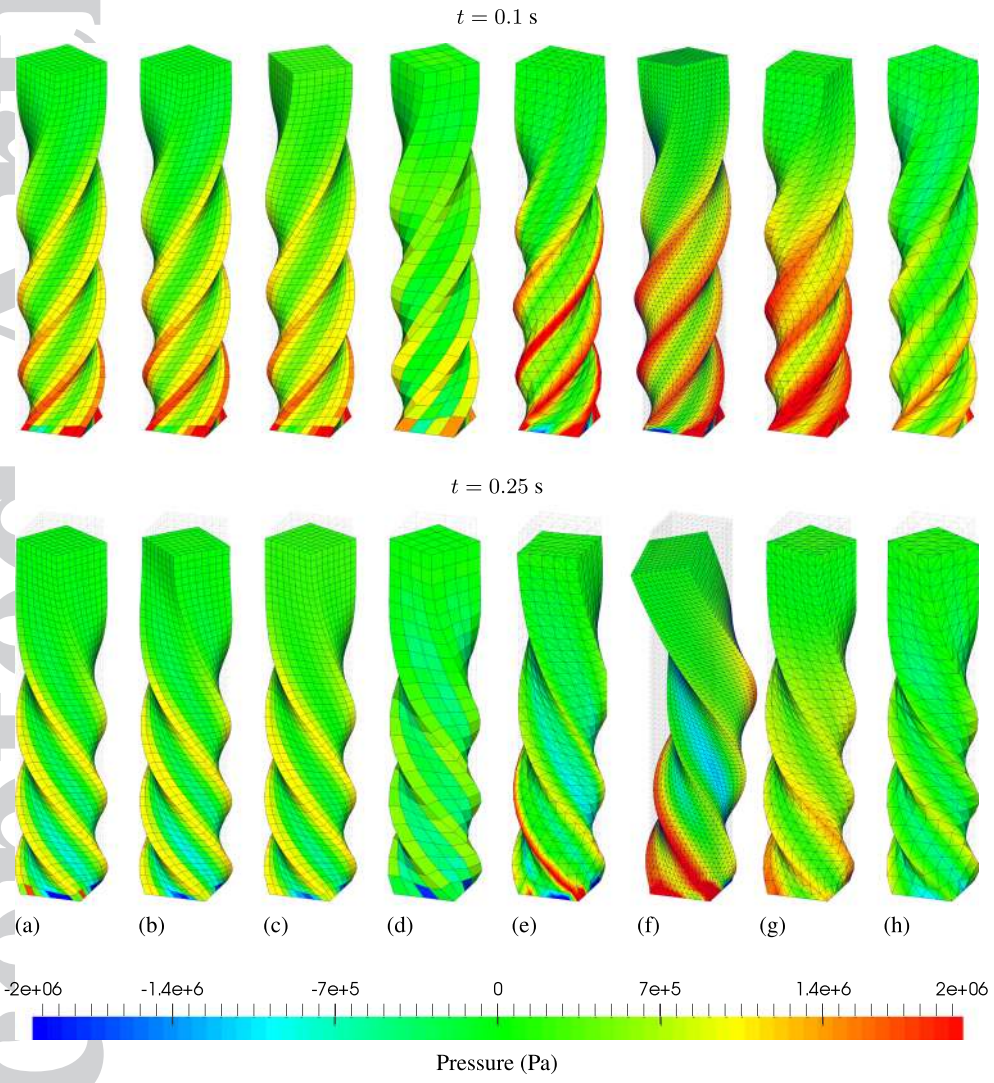

Figure 33. Twisting column: Time evolution of deformation plotted with pressure distribution. Results are simulated using the standard FVM update (penalised-TOUCH with $\xi_F = 0$) with an angular velocity field $\omega_0 = [0, \Omega \sin(\pi Y/2L), 0]$, where $\Omega = 105$ rad/s and $L = 6$ m. A neo-Hookean material is used with density $\rho_0 = 1100$ kg/m^3, Young's modulus $E = 17$ MPa, Poisson's ratio $\nu = 0.45$ and $\alpha_{\text{CFL}} = 0.3$. Discretisation of $4 \times 24 \times 4$ hexahedral elements.

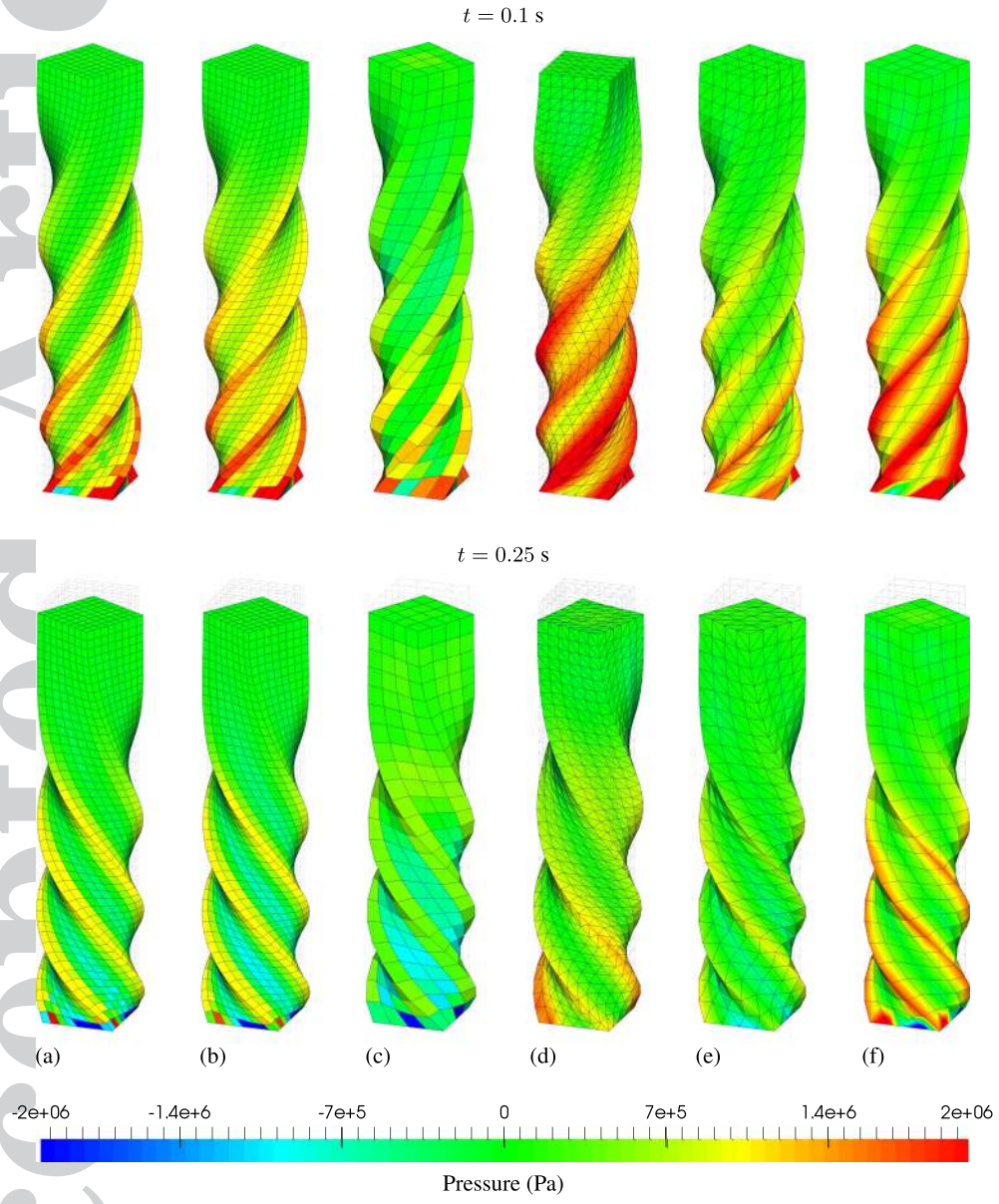

Figure 34. Twisting column: Comparison of deformed shapes plotted with pressures at time $t = 0.1$ s and $t = 0.25$ s using various numerical schemes: (a) Constrained-TOUCH; (b) Penalised-TOUCH ($\xi_{\boldsymbol{F}} = 0.1$); (c) Hyperelastic-GLACE [2]; (d) B-bar hexahedral method; (e) Upwind-VCFVM [46]; (f) JST-VCFVM [43]; (g) PG-FEM [45]; and (h) Hu-Washizu type variational principle [54]. Results obtained with an angular velocity field $\omega_0 = [0, \Omega \sin(\pi Y/2L), 0]$ where $\Omega = 105$ rad/s and $L = 6$ m. A neo-Hookean material is used with density $\rho_0 = 1100$ kg/m^3, Young's modulus $E = 17$ MPa and Poisson's ratio $\nu = 0.45$.

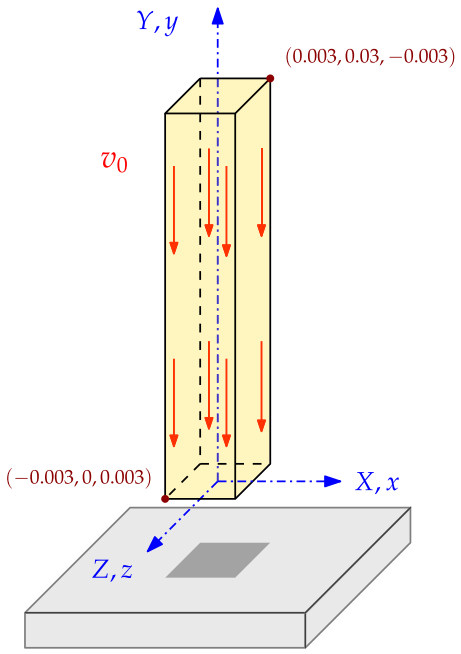

Figure 35. Twisting column: Comparison of deformed shapes plotted with pressures at time $t = 0.1$ s and $t = 0.25$ s using various numerical schemes: (a) Constrained-TOUCH; (b) Penalised-TOUCH ($\xi_{\boldsymbol{F}} = 0.05$); (c) B-bar hexahedral method; (d) PG-FEM [45]; (e) Hu-Washizu type variational principle [54]; and (f) Q2-Q1 hexahedral FEM. Results obtained with an angular velocity field $\omega_0 = [0, \Omega \sin(\pi Y/2L), 0]$ where $\Omega = 105$ rad/s and $L = 6$ m. A neo-Hookean material is used with density $\rho_0 = 1100$ kg/m^3, Young's modulus $E = 17$ MPa and Poisson's ratio $\nu = 0.495$.

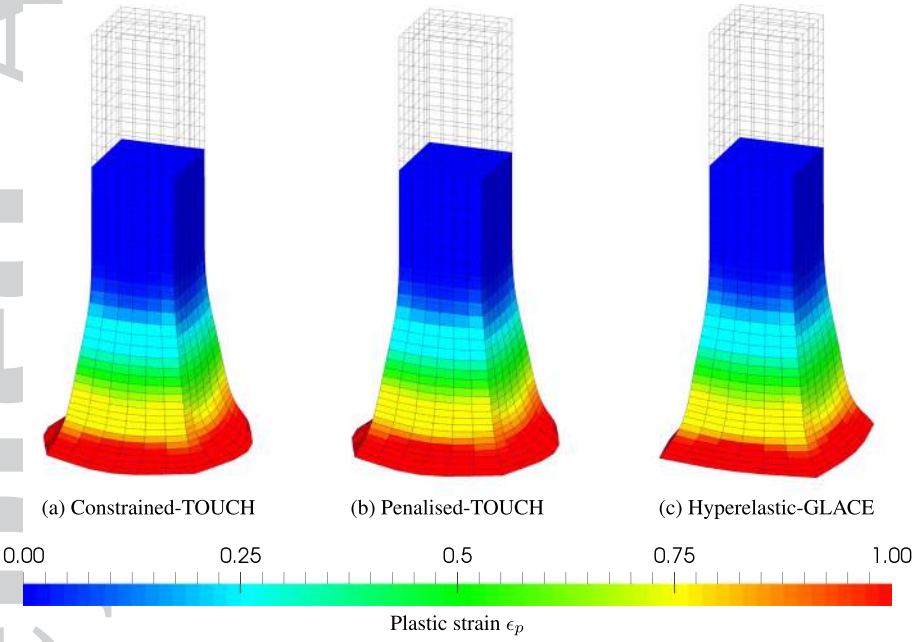

Figure 36. Taylor impact configuration

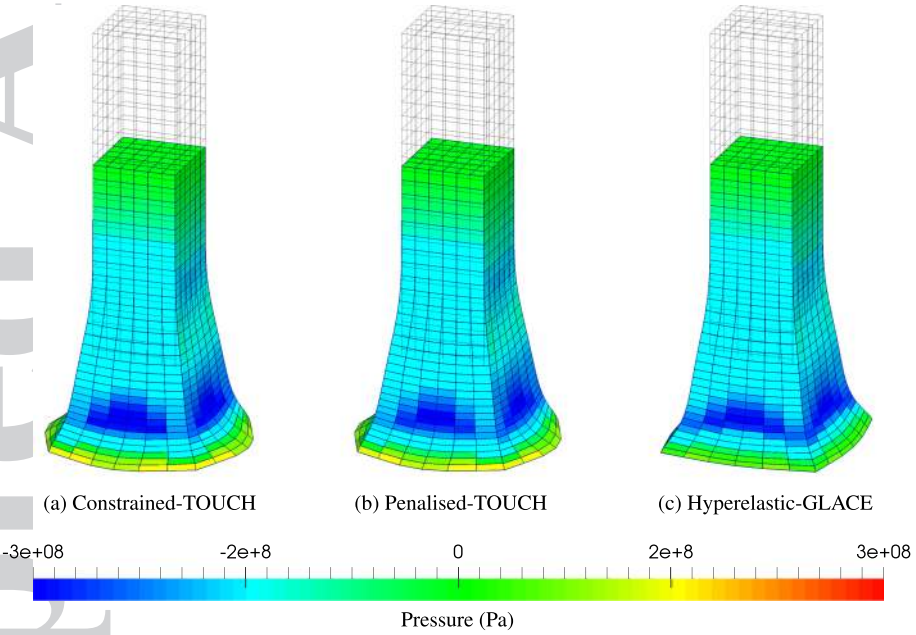

Figure 37. Taylor impact: Comparison of deformed shapes plotted with pressures using various numerical schemes: (a) Constrained-TOUCH, (b) Penalised-TOUCH ($\xi_{\boldsymbol{F}} = 0.15$) and (c) Hyperelastic-GLACE [2]. Results obtained with a constant velocity field $v_0 = [0, -227, 0]^T$ m/s at time $t = 60\,\mu$s. A von Mises hyperelastic-plastic material is used with density $\rho_0 = 8930$ kg/m^3, Young's modulus $E = 117$ GPa, Yield stress $\bar{\tau}_y^0 = 0.4$ GPa, Hardening modulus $H = 0.1$ GPa and Poisson's ratio $\nu = 0.35$ and $\alpha_{\text{CFL}} = 0.3$.

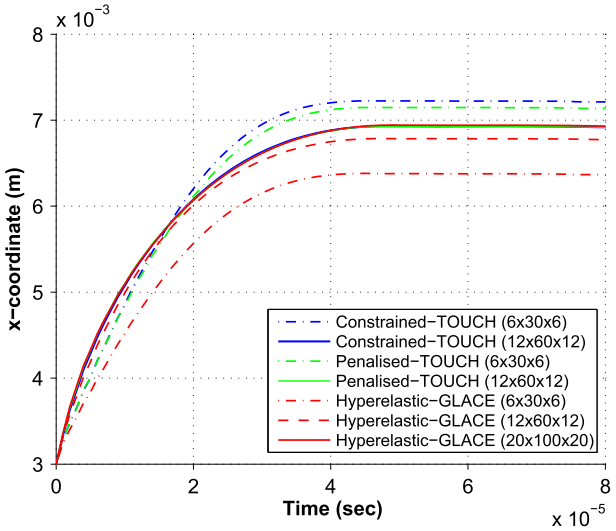

Figure 38. Taylor impact: Time history of the x coordinate of the point $\boldsymbol{X} = [0.003, 0, 0]^T$. Comparison obtained from three different numerical schemes: (a) Constrained-TOUCH, (b) Penalised-TOUCH ($\xi_{\boldsymbol{F}} = 0.15$) and (c) Hyperelastic-GLACE [2]. Results obtained with a constant velocity field $v_0 = [0, -227, 0]^T$ m/s using mesh sizes of $6 \times 30 \times 6$, $12 \times 60 \times 12$ and $20 \times 100 \times 20$ hexahedral elements. A von Mises hyperelastic-plastic material is used with density $\rho_0 = 8930$ kg/m^3, Young's modulus $E = 117$ GPa, Yield stress $\tau_y = 0.4$ GPa, Hardening modulus $H = 0.1$ GPa and Poisson's ratio $\nu = 0.35$ and $\alpha_{\text{CFL}} = 0.3$.